UNIVERSITY OF CALIFORNIA

SANTA CRUZ

DESIGN, CONSTRUCTION, AND ON-SKY PERFORMANCE OF A MEMS-BASED UPLINK-ADAPTIVE OPTICS SYSTEM

A dissertation submitted in partial satisfaction of the

requirements for the degree of

DOCTOR OF PHILOSOPHY

in

ELECTRICAL ENGINEERING

by

Andrew Paul Norton

June 2014

The Dissertation of Andrew Paul Norton is approved:

Professor Joel Kubby, Chair

Dr. Donald Gavel

Professor Claire Max

Professor Don Wiberg

Tyrus Miller
Vice Provost and Dean of Graduate Studies

Table of Contents

List of Figures

List of Tables

Abstract

Design, Construction, and On-sky Performance of a MEMS-based Uplink-Adaptive Optics System

by

Andrew Paul Norton

I present the design, construction, and on-sky results of the world‘s first micro-electrical mechanical systems (MEMS) deformable mirror (DM)-based adaptive optics (AO) system used for laser uplink correction. This system was integrated into the beam transfer optics of the laser guidestar at the University of California Observatory‘s 3-meter Shane telescope at Mt. Hamilton, and provided correction of the quasi-static phase aberrations in the 3.5 Watt sodium. A novel extension of this research as a means for producing multiple LGS spots (asterisms) from a single laser beam is also presented.

I also developed the architecture for the woofer-tweeter controller for the new ShaneAO system. This controller uses the natural modal basis set of each of the deformable mirrors, and takes into account the spatial and temporal characteristics of each DM to provide and efficient and effective method for correcting for atmospheric turbulence.

To my family and friends,

with gratitude

Acknowledgments

"An individual tends to absorb the surrounding spirit and to radiate the acquired lifestyle and worldview to anyone around" -Andrei Kolmogorov

I have been extremely privileged to do research in the field of Adaptive Optics, let alone to have had the opportunity to work under the talented and supportive people at the Center for Adaptive Optics. A special thanks to my advisors Don Gavel, Claire Max, Joel Kubby, Don Wiberg. To the team at the Laboratory for Adaptive Optics, Daren Dillon, Renate Kupke, Katie Morzinski, Sandrine Thomas, and Luke Johnson. Lisa Poyneer, Bruce Macintosh and Dave Palmer of Lawrence Livermore National Laboratory. Fellow graduate students Srikar Srinath, Rosalie McGurk, and Oscar Azucena. To Drew Phillips, Jim Ward, Terry Pfister, Dave Hilyard, and Brian Dupraw of the UCO optical shops. Elinor Gates, Kostos Chloros, and Donnie Redel of the UCOLick Observatory. To Micheal Helmbrecht and Carl Kempf of IrisAO Inc. And to my parents and fiancee.

There where times during this research that we stood at the edge of all previous knowledge about this subject, where people had never before explored. I cannot put to words how thrilling of a feeling it was to experience this. Graduate school provided me an environment that made it safe to explore some truly wild ideas. For this I will always be grateful.

Chapter 1

Introduction

"I consider that I understand an equation when I can predict the properties of its solutions, without actually solving it." -Paul Dirac

In his 1953 paper [1] on "The Possibility of Compensating Astronomical Seeing", Horace Babcock was first to give serious thought to the design of an optical system that could actively measure and correct the atmosphere‘s deleterious effects imposed on astronomical images. However, it wasn‘t until the launching of the Sputnik satellite by the Union of Soviet Socialist Republics (USSR) in 1957, that the need for an Adaptive Optics (AO) system that could remove the blurring effects of the atmosphere received adequate attention [2]. As in many cases, government funding supplied opportunities for research and development by engineers, physicists, chemists, statisticians and mathematicians, creating the multi-disciplinary field that became Adaptive Optics.

Horace Babcock‘s initial adaptive optics design was unknown to the researchers (private communication, David Fried) working under what was then the United States Defense Advanced Research Projects Agency (DARPA). As a result, much of the explored technology resulted in AO system designs that had no connection and did not build on Babcock‘s idea. By the end of the 1970‘s the basics of adaptive optics were considered to be well in hand [3], and subsequent exploration of laser communication with satellites led to further understanding of the atmosphere‘s effects and AO system requirements. The success of these initial AO systems, along with the advances in technology and declassification of these techniques, components and ideas in 1992, has since resulted in large astronomical optical and infrared ground-based telescope being equipped with an adaptive optics system.

1.1 Contributions of this Thesis

This thesis concerns itself with the adaptive optics correction of optical wavefront deviations for two different cases — firstly, that of sodium laser guidestar light propagating upwards through the atmosphere, and secondly with the arrival of distant star light traveling down through the atmosphere.

1.1.1 First On-Sky demonstration of Laser-Uplink Adaptive Optics for Astronomical Applications

The first half of this thesis is focused on improving the quality of laser guidestars‘ (LGS) wavefront, specifically at the University of California Observatory (UCO) Lick 3-meter Shane telescope at Mt. Hamilton. I present the idea behind this investigation aimed at pre-compensating the LGS beam for internal, slow time-varying phase aberrations. I also present analysis and results from the first on-sky demonstration of laser uplink-AO using a Micro-Electrical Mechanical Systems (MEMS) deformable mirror (DM). The final section of this half of the thesis investigates the use of a DM in the uplink-AO path as a novel means for generating a desired LGS asterism for application in Multi-Conjugate and Multi-Object Adaptive Optics.

1.1.2 Woofer-Tweeter Control Architecture for the new Shane AO system upgrade

The second half of this thesis is also related to the Shane 3-meter telescope at Mt. Hamilton, but concerns itself with the case of phase variations imparted to star light as it propagates down through the Earth‘s atmosphere. I present a design to efficiently and effectively control two deformable mirrors arranged in series (woofer-tweeter) that have overlapping temporal and spatial characteristics, and that share a common wavefront sensor (WFS). Simulations and experimental laboratory results are conducted to validate the proposed woofer-tweeter control architecture.

1.2 Physical assumptions and definition of parameters

An accelerating charge constitutes a source for generating a self-sustaining electromagnetic wave. The propagation of this electromagnetic wave through space and time is described by Maxwell‘s equations. For the purpose of this analysis, we will assume that any point in the electric field is oscillating perpendicular to our line-of-sight, so that the light propagates in the direction of our detector. Furthermore, we will concern ourselves only with the component of the electromagnetic field that dies off inversely proportional with the distance from its source, namely, the third component of Coulomb‘s electric field force.

Now, any point in the electric field can be thought of as an arrow rotating around a point. Mathematically this can be represented as a vector on a Cartesian coordinate system. The amplitude of the oscillation is given by the length of the vector and the phase is represented by the angle of the vector from the real axis.

To simplify the mathematics we define the vertical axis as the imaginary axis and we use use the mathematical constant e to link the complex plane to the real plane. We acknowledge the link between geometrical and trigonometric relationships, using Euler‘s equation

$$E(\omega, t) = E_o e^{\imath\omega t} = E_o(\cos\omega t + \imath \sin\omega t) \tag{1.1}$$

Where E_o represents the amplitude of the electric field (Amps/meter) [**?**], t is the time at which electric field is measured, and ω is the angular frequency (radians per second) of the light. Now imagine two points in the electric field separated a distance d from each other as shown in Figure 1. Each point can be described mathematically as $E_1(\omega, t) = A_o e^{\imath(\omega t + \phi_1)}$ and $E_2(\omega, t) = A_2 e^{\imath(\omega t + \phi_2)}$ where A_1 and A_2 are the amplitudes of each antenna, ω is the angular frequency (radians per second), and ϕ is the initial phase of the of the electric field at this instance in time.

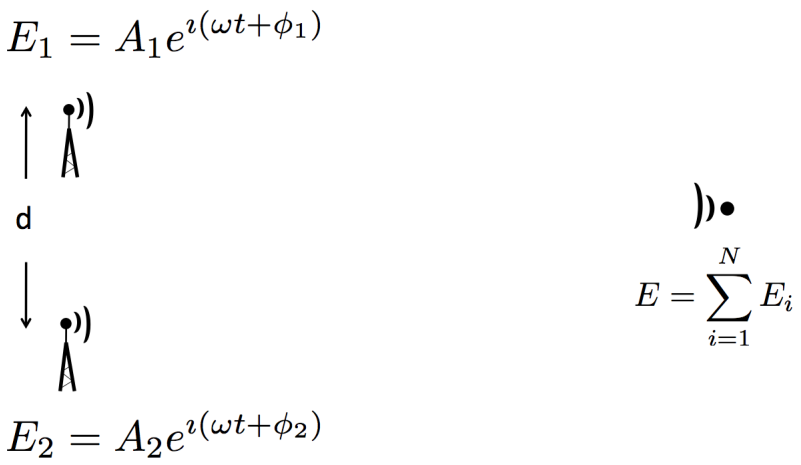

Figure 1.1: Points in the electromagnetic field represented as oscillating antennae spaced distance d apart. The detector located to the right of the charges measures the resulting linear superposition of the electric fields when they are brought to a focus.

The electric fields from each of the two points interact according to the laws of linear superposition, resulting in $E = \sum_{i=1}^{N} E_i$, the electric field at the detector plane. This can be mathematically represented as

$$E = A_1 e^{\imath(\omega t + \phi_1)} + A_2 e^{\imath(\omega t + \phi_2)} \tag{1.2}$$

or equivalently as

$$E = e^{\imath\omega t}(A_1 e^{\imath\phi_1} + A_2 e^{\imath\phi_2}) \tag{1.3}$$

where $e^{\imath\omega t}$ is the angular rotation of the resulting vector. Because both antennae oscillate at the same frequency, and hence have the same color, the resulting electric field vector will rotate through the same number of radians per second on the Cartesian graph.

So we can drop the $e^{\imath\omega t}$ term for now, and concern ourselves only with the resulting amplitude and phase of the new electric field in the detector plane

$$E = (A_1 e^{\imath\phi_1} + A_2 e^{\imath\phi_2}) = \hat{E} \tag{1.4}$$

This complex wave represents the new electric field at the location of our detector. However, our detector can measure only the energy of the electromagnetic wave and not the phase of the electric field. So we understand that we can measure the intensity of the resulting wave from the two sources, and that the intensity is proportional to the square of the electric field, averaged in time. Mathematically this is described as

$$I = \hat{E}^2 = EE^* = |E|^2 \tag{1.5}$$

The vector will rotate counter clockwise, and this vector represents the new electric field wave resulting from the two light antennae that will interact with our detector. Thus, the intensity at our detector from the new electric field can be found by inserting equation 1.4 into 1.5, resulting in

$$I = A_1^2 + A_2^2 + A_1 A_2 (e^{\imath\phi_1 - \phi_2} + e^{\imath\phi_2 - \phi_1}) \tag{1.6}$$

Using the relationship

$$e^{\imath\theta} + e^{-\imath\theta} = \cos(\theta) + \imath\sin(\theta) + \cos(\theta) - \imath\sin(\theta) = 2\cos(\theta) \tag{1.7}$$

the intensity due to two sources of different amplitudes and initial phases at the detector is

$$I = A_1^2 + A_2^2 + 2A_1 A_2 \cos(\phi_1 - \phi_2) \tag{1.8}$$

When the amplitudes of the sources are the same, we see that the intensity has the following properties for different phase relationships

$$I(\Delta\phi) = \begin{cases} 4A^2 & \text{for} \quad \Delta\phi = 0, (n)2\pi \\ 2A^2 & \text{for} \quad \Delta\phi = (n/2)\pi \\ 0 & \text{for} \quad \Delta\phi = (n)\pi \end{cases} \tag{1.9}$$

where n is an integer, the intensity is maximum (4 times the amplitude squared) when the phase difference between the two sources is an even integer multiple of $n2\pi$; half the maximum intensity at multiples of $(n/2)\pi$; and zero at odd integer multiples of π. For cases when the amplitudes of the sources are different, such as a Gaussian beam profile, the intensity will never be zero.

In the case of astronomy, the distance between the two antennae in Figure 1.1 is the diameter of the primary mirror. Each point of the electric field captured by the primary mirror can be thought of as a local oscillator. The curvature of the primary mirror ensures the phase of these waves arrive at the detector at the same time, and hence, in phase.

The angular resolution is set by the furthest separation of the points in the electric field as defined by the diameter of the telescope and the wavelength of light. This is the theoretical best resolving power of a telescope, which assumes that the oscillators that make up the aperture are all in phase with one another. When an external source such as starlight reaches the telescope, the electromagnetic field imparts a force on the electrons via the Lorentz force, and so drives the electrons creating a new electric field. The electrocromagnetic waves from each of these new sources add linearly, as described above, producing the diffraction-limited intensity pattern in the detector plane. It is these optical phase relationships that govern the image structure.

For telescopes operating in the optical and near-infrared wavelengths and located on the ground, achieving diffraction limited angular resolution is severely limited by the

turbulent atmosphere.

Mathematical analysis by A.N. Kolmogorov [5], V.I. Tatarski [6] and David Fried [7] [8] [9] has led to current understanding of the physical characteristics of atmospheric turbulence's effects on image formation.

The atmosphere is in constant motion. Turbulence in the atmosphere arises from differential heating of the Earth's surface as it rotates through the Sun's light. Energy is input to the atmosphere starting at the large scale, with turbulent cells on the order of a ~ 100 meters that dissipate energy to smaller and smaller turbulent cells on the order of a few millimeters. As the energy is transferred between these scales it creates regions in the atmosphere that vary in temperature and thus pressure, each with a different index of refraction. As the isophase of the star light propagates through this non-homogeneous, turbulent medium, the index of refraction variations are mapped into the local phase variations of the incoming beam. That is, the phase error accumulated by light passing through the atmosphere is the sum of the index of refraction contributions along the entire path, stated mathematically as

$$\phi(x) = k \int_{h}^{h+\delta h} n(x, z) dz \tag{1.10}$$

where k is the wavenumber, $2\pi/\lambda$. Measurements of the uniform index of refraction along a line-of-sight are displayed in Figure 1.2, showing that the averaged index of refraction of the atmosphere from the ground to 100 kilometers differs by no more than

one one-thousandth of a percent.

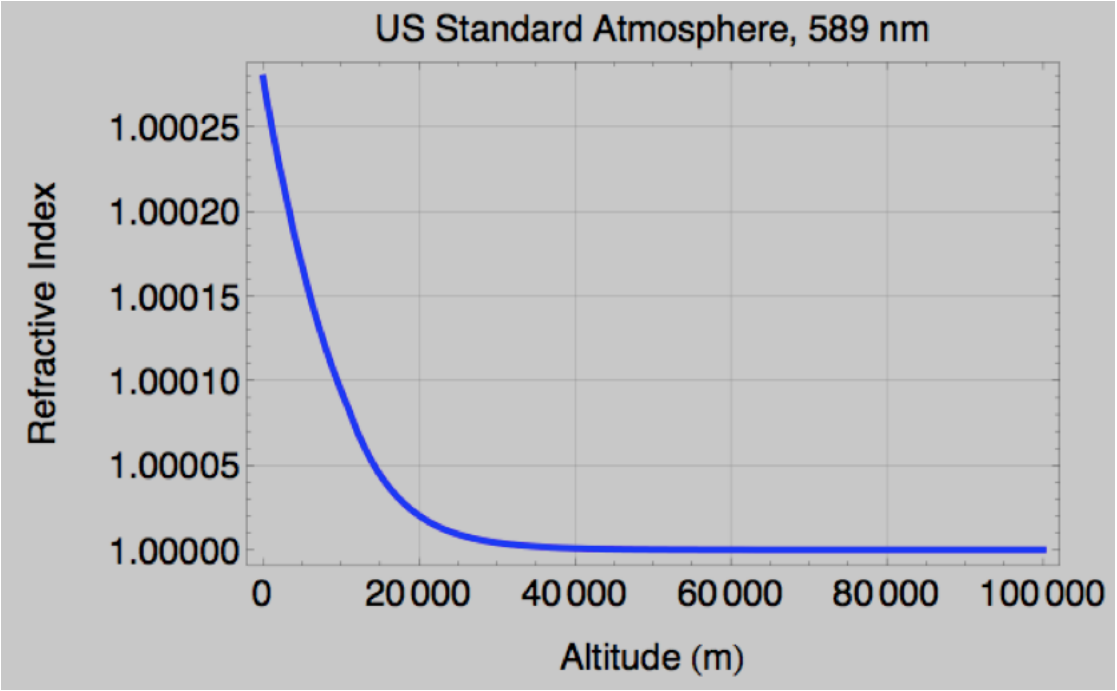

Figure 1.2: The uniform component of the index of refraction measured through the Earth‘s atmosphere, courtesy of Robert Fugate

If one could take a snap shot and freeze the electric field after it has passed through the Earth‘s atmosphere, one would find that the distance along the phase front by which the electric field varied by one wavelength — that is to say the relative phase angle across all these vectors in this plane — would differ by 2π radians. Stated another way, this is the same resolution that would be obtained in the absence of the atmosphere with a diffraction-limited lens of diameter r_o [8]. As mentioned above, the physical significance of this is that at the detector plane the intensity at the corresponding angle λ/r_o would be zero. For Kolmorogrov turbulence, this distance between the oscillators

described in Figure 1.1 is typically around 25 cm at a wavelength of 500 nm, meaning that a ground-based telescope will have no better angular resolution than a 12 inch telescope. This distance, known as the atmospheric coherence length parameter, or r_o, can be stated mathematically as

$$r_o = [0.423k^2(\sec\zeta)\int C_N^2(h)dh]^{-3/5} \tag{1.11}$$

It is dependent on the wavenumber k (ro is smaller at shorter wavelengths), the angle from zenith ζ (r_o is smaller at larger angles from zenith because of the added path of atmosphere), and the refractive index structure constant $\int C_N^2$, which is the link to the temperature and pressure structure functions and hence the refractive index variations. Also known as the Fried parameter, named after its discoverer, r_o is arguably the most important parameter in adaptive optics as it determines the relevant timescales of turbulence, the isoplanatic angle or angle over which AO compensation will be relevant, the number of degrees of freedom required for the wavefront correct, as well as many other important AO system requirements.

A schematic of the effect of r_o on image formation in adaptive optics is shown in Figure 1.3. The ideal, diffraction-limited angular resolution of $2.44\lambda/D$ for a circular aperture is shown on the left for reference. When Kolmogorov turbulence is present, the long exposure results in an intensity distribution with an angular resolution proportional to λ/r_o caused by the blurring of each r_o size diameter aperture present over the telescope diameter. A short exposure image reveals the D/r_o number of sub-images present in the

intensity plane, each with an angular resolution of λ/D due to the cumulative effects of each phase value across the primary. Note the reduction in intensity in each spot.

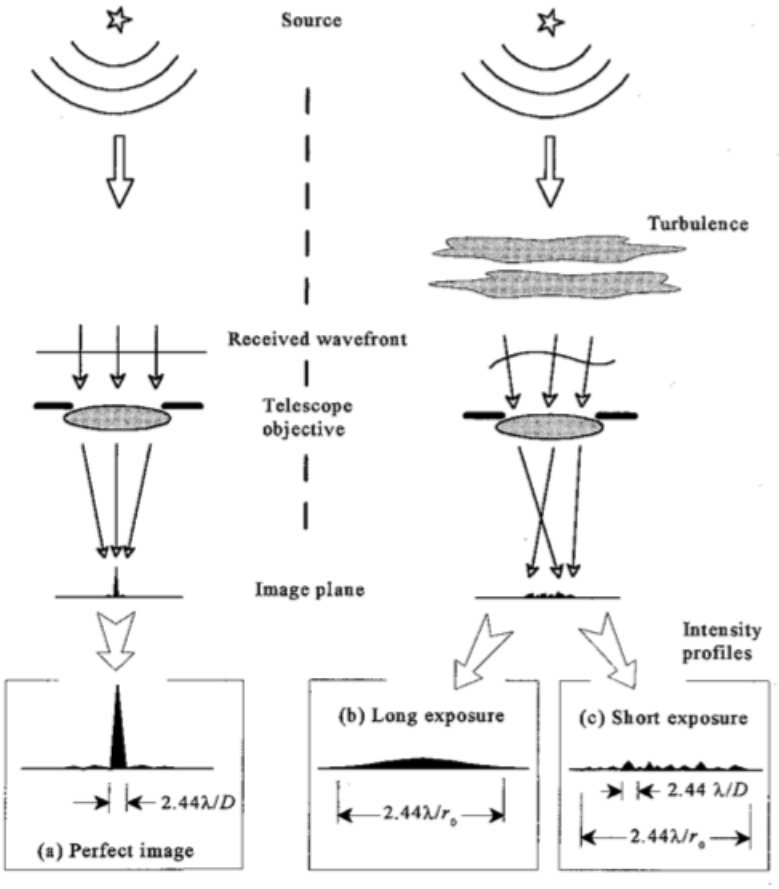

Figure 1.3: Schematic of the perfect point spread function (PSF) (image left) and the effects of atmospheric turbulence on long- and short-time exposures (images right). Image Credit: J.W. Hardy.

In order to correct for the turbulence, the AO system must measure and correct for the optical path length differences over each sub-aperture r_o before they change. For astronomical applications, a common and valid assumption for the timescale over which

the turbulence in the atmosphere changes is dependent on how long it takes the wind to translate the r_o size aperture by one r_o length. This is known as Taylor's frozen-flow hypothesis [10] [11], which states that 1) the entire pattern of a random turbulent field is transported along with the wind velocity and 2) turbulent eddies do not change significantly as they are carried across the telescope by the wind.

This simplifying hypothesis about the time behavior of the Earth's turbulence closely approximates atmospheric conditions observed at the Palomar and Lick observatories [14], and also at observatories at Mauna Kea [15].

Typical values for average seeing and wind conditions at an observatory for an AO system operating in the visible wavelengths are a timescale τ_o on the order of a few milliseconds.

An example of correction achievable with the AO system on the 200 inch Hale Telescope at the Palomar Observatory is shown in Figure 1.4. Note the visible diffraction pattern of each star after AO correction, owing to the wave nature of light.

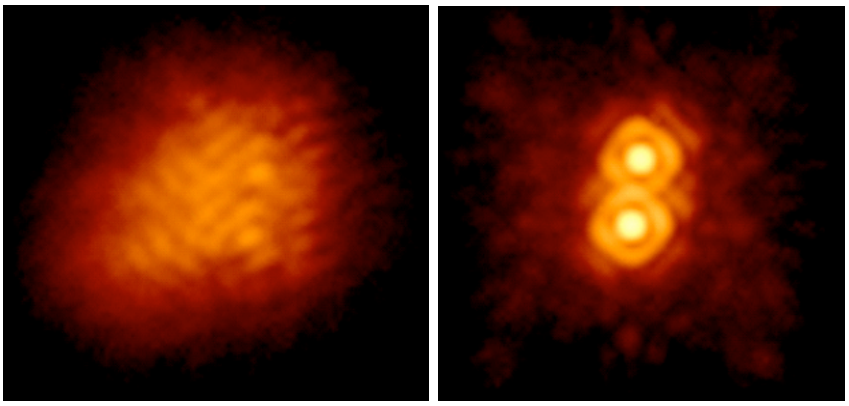

Figure 1.4: Image of binary star IW Tau without (left) and with (right) adaptive optics. The stars have a 0.3 arc second separation. The images were taken by Chas Beichman and Angelle Tanner of JPL.

Before concluding this introduction it is relevant to note one final physical assumption important to the work contained herein. Namely, that of the geometrical assumption in adaptive optics.

The geometrical assumption presumes that index of refraction variations add linearly and and do not cause rays of the incoming light to cross paths before reaching the primary mirror of the telescope. This assumption has two significant physical interpretations that are relevant to the work presented in this thesis.

Firstly, changes in optical path length produced by turbulence are almost independent of wavelength, because the spectral dispersion of air is very small over the visible and IR spectral bands [16].

Secondly, under the geometric assumption, turbulence is not strong enough to produce

mixing of the electric field‘s phase and amplitude, so this thesis will not deal with this effect known as scintillation. This assumption is valid for weak turbulence, such as that found at good astronomical sites [16] [17]. Under these conditions, the optical pathlength disturbances in light rays emanating from a single point source can be compensated by placing the wavefront corrector at any location in the ray path [16]. This concept will be especially relevant in the first chapter of this thesis.

Chapter 2

Laser-Uplink AO at Mt. Hamilton using a MEMS Deformable Mirror

2.1 Summary

By inserting an adaptive optics system into the sodium laser guidestar‘s (LGS) beam transfer optics (BTO), we actively controlled the wavefront quality of the outgoing laser. This allowed us to correct for internal, slow-time varying aberrations, provide dynamic refocusing of the laser guidestar spot in the mesosphere, and make a more compact, more uniform spot, thus decreasing the measurement error and increasing the performance of the adaptive optics system located behind the primary. Furthermore, inclusion of an adaptive optics system in the laser launch path relaxes alignment tolerances and in the future could be used to correct for the atmospheric turbulence along the laser light path

as well as provide a means for generating custom laser guidestar asterisms.

2.2 Introduction

Adaptive optics (AO) systems measure and correct in real-time for the deleterious effects caused by the Earth‘s atmosphere, enabling ground-based telescopes to achieve diffraction-limited images. However, less than 1 percent of the night sky provides a sufficiently bright reference source for the AO system to achieve good correction, thus severely limiting the benefits of imaging with AO.

To overcome this, many of the world‘s optical and infrared telescopes use a $10-50$ Watt class laser [23] to excite sodium atoms that are present between roughly 87 and 97 km in the mesosphere — higher than this and the sodium atoms ionize, lower and they mix with oxygen.

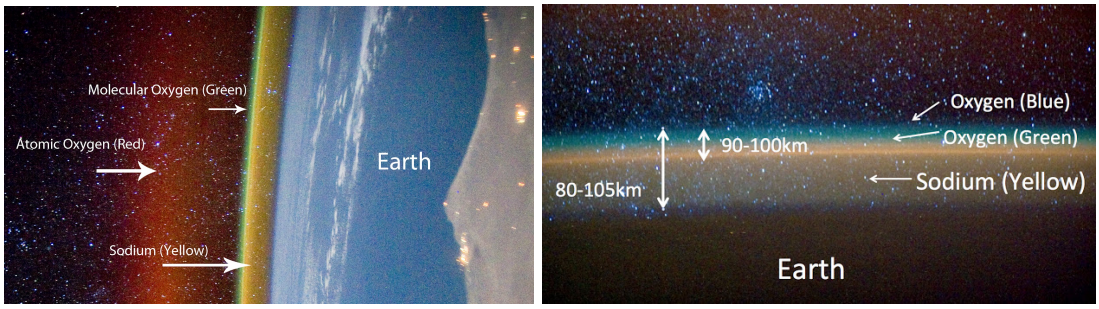

Figure 2.1: Images taken from the International Space Station and processed by Alex Rivet. (Left) Stars, the Earth's atmosphere, ocean and land on the right. Sodium atoms, located in the mesosphere at a median altitude of 92 km, are deposited there when meteorites enter the atmosphere. (Right) Close up of the upper atmosphere, showing the sodium layer. These sodium atoms are excited with laser light (not shown) from Earth and provide a reference beacon for AO systems to measure the turbulence. Image credit: http://auroranightglow.blogspot.com/

Once excited, light from the sodium atoms create a reference source, known as a laser guidestar (LGS). This provides a return flux sufficient for the AO system to measure the turbulence in the direction the laser is pointing, thus greatly increasing the range of application and benefit of adaptive optics.

Coupling of the laser power to the sodium atoms — and thus the efficiency of amount of light returned to the telescope from resonant optical backscattering [24] — is dependent on many factors, including density of the sodium atoms which varies seasonally [12], optical repumping and laser pulse format, orientation of the LGS beam with the respect to Earth's magnetic field, and polarization state [13] of the LGS light to name a few.

The research presented in this paper concerns itself only with the effects of the phase of the outgoing LGS electric field.

Phase errors can be introduced into the laser guidestar beam in two ways: 1) internally, as the laser light propagates through the beam transfer optics located inside the telescope dome and 2) externally, from the index of refraction variations in the turbulent atmosphere as the laser travels to the sodium layer. Both sources of phase errors adversely affect the shape of the LGS spot and the ability to concentrate the laser light into the sodium layer.

In most arrangements, the sodium laser light is free space propagated through the beam transfer optics (BTO) and then launched from a laser launch telescope (LLT). The LLT is typically located on the side of the telescope‘s primary mirror or behind the secondary mirror. The last component in the LLT is either a refractive or reflective element with typical diameters ranging from 20 to 40 cm. However, imperfections in the lenses and optics along the BTO introduce phase error in the electric field of the laser beam that degrade the shape and size of the beam in the mesosphere.

Naturally, this would lead one to ask what benefits, if any, would be achieved by incorporating an AO system in the laser launch telescope that used a deformable mirror to correct for any slow time-varying, internal aberrations. Or, the turbulence above the launch telescope is known, then one could precompensate the outgoing laser beam, imparting a deliberately aberrated phase to the outgoing beam such that the atmosphere would apply the conjugate phase, delivering a diffraction limited spot at the target.

This technique of using an adaptive optics system to correct the outgoing laser beam is referred to as laser uplink-AO.

2.2.1 Background

The first cases of laser beam precorrection date to September 1985, when Darryl Greenwood and the team at Lincoln Lab used a 69-channel DM to score a sounding rocket with a 532 nm laser [19]. Similar tests were repeated again with success, this time in February, 1990 by Dan Murphy and the Lincoln Laboratory team using a 241-channel AO system.

In July 2003, the team at Starfire Optical Range pre-corrected a 8.5 W Sodium LGS that was launched form 0.5 meter diameter telescope [20]. The sharpened spot was imaged with a 3.5 meter telescope 50 meters from the launch telescope and was concluded to form a 38 cm FWHM spot in the mesosphere (0.87 arcseconds), nearly 50% smaller than the uncompensated beam. The deformable mirror used in uplink-AO experiment at the SOR was several tens of centimeters in diameter (private communication, Craig Denman) and was expensive even by today‘s standards.

While the use of laser beam shaping has many applications, including telecommunications, energy research, biology, and national security, the use of deformable mirrors for astronomy-based laser applications is still relatively new.

2.2.2 Motivation

At approximately $100,000 per Watt, sodium lasers tuned to the D2 line remain the largest subsystem cost for many current and next generation AO systems [22]. On top of this, the high price of electricity at remote telescope sites combined with the substantial amount of power used to run these relatively inefficient systems makes them expensive to operate. For example, the Keck 2 laser system operating at full time (roughly 90 nights per year, private communication, Peter Tucker, W.M. Keck Observatory) at 40 cents per kilowatt-hour results in an annual electricity bill of roughly $22,000.

Incorporating a deformable mirror in the laser launch telescope is desirable both systematically and economically.

Interest in integrating this concept into astronomy-based applications was first published in 2008 [23] in the Visible light laser guidestar experimental system (Villages). The goal of Villages was to precorrect the outgoing LGS beam and launch it from a 1-meter diameter telescope. This beam launch configuration would result in a depth of focus closely matching the thickness of the sodium layer and an LGS spot smaller than the atmospheric coherence length. As is understood from theory, the pairing of such a small reference source with a diffractive wavefront sensor (WFS) such as a pyramid wavefront sensor, would require only 2 Watts of sodium laser light [23].

More recently, in 2012 the Gemini South Observatory reported the goal of using deformable mirrors in their LGS launch system as a means to improve stability, robust-

ness, and performance of laser systems [21]. This is a dual-deformable mirror system designed to correct both the phase and amplitude errors of their LGS beam.

This chapter reports on the first-ever performance of Uplink-AO with a MEMS deformable mirror, in which the DM was incorporated into the laser‘s beam transfer optics path and allowed control of the size and shape of the LGS spot in the mesosphere. On-sky tests were conducted at the University of California Lick Observatory on Mt. Hamilton in northern California with the sodium dye laser guidestar.

2.3 Deformable Mirrors for Laser-Uplink AO

Among the most pertinent requirements of a deformable mirror for laser uplink-AO applications are its ability to meet the surface deflection needed to conjugate the phase errors and the DM‘s ability to withstand the incident laser power.

Certainly, this task of laser uplink AO places strict demands on the deformable mirror as not only must the DM be able to withstand the high optical power, it must be able to do this night after night, sometimes with the laser-light being incident for several continuous hours, and still remain fully functional and without any permanent damage.

Over the past 50 years many different types of deformable mirrors have become commercially available for high energy laser applications. One such example is the piezoelectrically driven, continuous-facesheet dielectric-coated membrane mirror from the Fraunhofer Institute for Ceramic Technologies and Systems. This DM can withstand

power densities up to 0.4 kW/cm [25].

While many other candidate deformable mirrors exist, in the last decade a relatively new type of deformable mirror made from the same type of batch fabrication technology as the integrated circuit technology has come along. This type of mirror is known as a Micro-Electrical Mechanical Systems (MEMS) deformable mirror. These mirrors have the advantage over conventional mirrors in that they are more compact , have a higher actuator-density, and can achieve micrometers of stroke with very accurate go-to position repeatability.

However, being a relatively new technology, the ability of a MEMS DM to provide phase correction for high-power laser guidestar applications was up until now not well studied. To this end, several MEMS deformable mirrors from two different companies, Iris AO Inc. and Boston Micromachines Corporation, were investigated at the Laboratory for Adaptive Optics in acceptance tests designed to qualify their use for applications in uplink-AO. Details on each of these devices and their response to incident laser light is presented in the next section.

2.3.1 MEMS deformable mirrors from Boston Micromachines Corporation.

Boston Micromachine Corporation‘s MEMS deformable mirrors are fabricated using a custom lithography process [26]. The deformable mirror structure consists of alternating

layers of polysilicon and oxide, with the latter being removed to allow the free standing structures to deflect under actuation (Figure 2.2). Deflection is achieved with capacitive electrostatic actuation. When an electrostatic potential is applied to the electrode, the double-cantilever plate above is deflected downwards. Consequently, this pulls down the attachment post which translates the deflection of surface of the mirror in a very highly controllable shape.

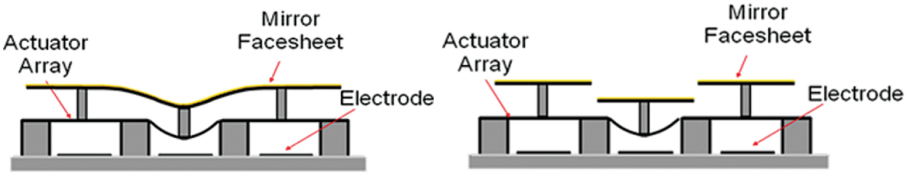

Figure 2.2: Schematic of the continuous-facesheet (left) and segmented (right) deformable mirrors from Boston Micromachines. Images courtesy of Boston Micromachines Corp.

Three 1024-actuator BMC DMs were tested: two continuous-facesheet DMs and one segmented deformable mirror (BMC segmented DM). The top polysilicon layer of the continous-facesheet DMs was 3 μm thick and the segmented DM was 8 μm thick. 100 nm of protected silver coated the segmented DM and one of the continuous-facesheet DMs. The silver-coated DMs have an overlaying 10 nm layer of magnesium fluoride to guard against oxidation. The other continuous-facesheet DM was coated with 70 nm of aluminum. An image of the continuous-facesheet BMC DM is shown in Figure 2.3.

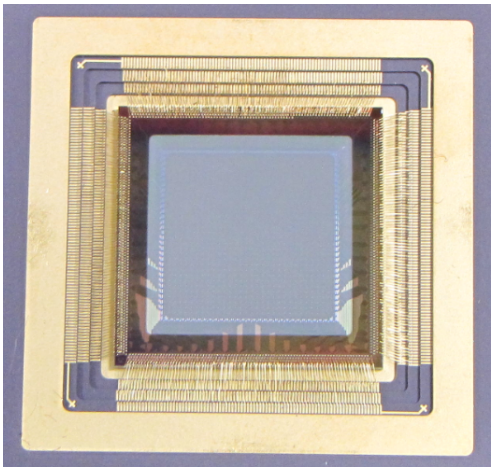

Figure 2.3: Image of the 1024 actuator silver-coated continuous-facesheet MEMS DM. The active DM area ($1cm^2$) is inner most reflective region, surrounded by the gold wires that connect the mirror drive electronics to the individual actuators.

The deformable mirror is the inner square region of Figure 2.3, with the wire bonds along the periphery. The actuators for each mirror are arranged in a 32×32 grid with 300 μm pitch giving an active aperture of 9.6 mm. Though these devices are often housed behind a window to guard against oxidation, the window was removed for the purpose of these tests.

2.3.2 MEMS deformable mirrors from IrisAO

The response of several Iris AOs PTT111 DMs to incident laser light was also studied. These deformable mirrors consists of 37 individual segments arranged in a hexagonal pattern as shown in the left image of Figure 2.4. These deformable mirrors have an

inscribed circular diameter of 3.5 mm. A cross section of single actuator is shown image right of Figure 2.4.

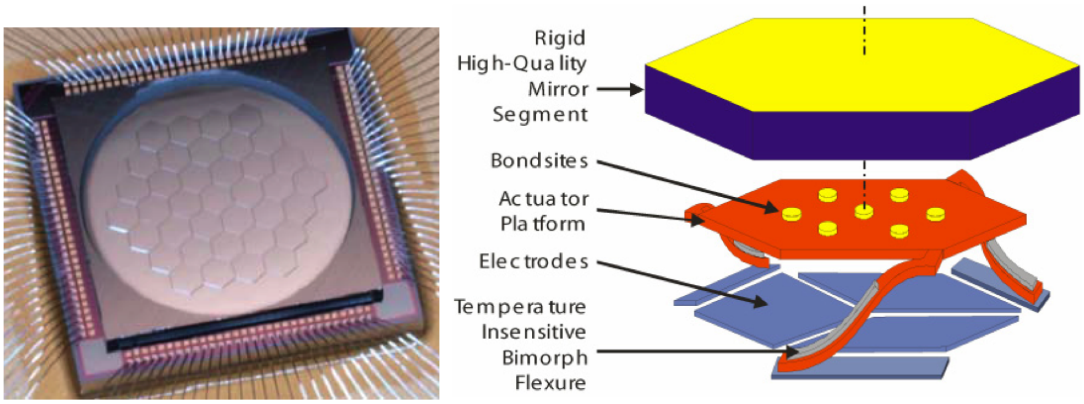

Figure 2.4: Left) Image of a 37 segment, 111 degree-of-freedom IrisAO DM. This DM has a working aperture of 3.5 mm. Right) Cross-section of a single segment. Images courtesy of Michael Helmbrecht.

These DMs are fabricated in a process that combines both surface micromachining and bulk micromaching [27] [29]. The 25 μm thick single-crystal silicon segments are coated with 250 nanometers of aluminum and flip-chip bonded onto the polysilicon-constructed actuator-platforms. The actuator platform and the three electrodes beneath form the parallel plate capacitor. Each electrode can individually be addressed, allowing for each segment to deflect in piston/tip/tilt motion, giving 111 degrees-of-freedom across the working aperture of the DM. Each segment is 700 μm vertex to vertex, and is separated by a 6 μm gap, giving a greater than 98 percent fill-factor.

The following subsections are a synthesis of the experiments I conducted to qualify

MEMS deformable mirrors for Laser uplink applications. The results presented here can also be found in publications in the proceedings of the International Professional Society for Optics and Photonics Technology (SPIE) [32] [32] [29].

2.3.3 High-Energy Visible-Wavelength Laser Experiments with MEMS Deformable Mirrors

Astronomical facilities require sodium laser powers of typically 10 Watts average output power. At the beginning of this research I didn‘t have access to a facility class sodium laser, so the Laboratory for Adaptive Optics‘ 2 Watt neodymium-doped yttrium aluminum garnet (Nd:YAG) laser was used to test the initial response of the MEMS DMs. These results allowed us to extrapolate the expected performance and response of the MEMS DMs to power levels required of a sodium laser at an astronomical observatory.

2.3.4 Testbed layout

Figure 2.5 is a schematic of the optical layout of the high-power laser test. The Nd:YAG laser light (λ=532 nm) exits the laser cavity at the top right of the image. The Gaussian-profile laser-light reflects off two flat mirrors (M1 and M2), before traveling the rest of the 2.5 meters to the surface of the deformable mirror.

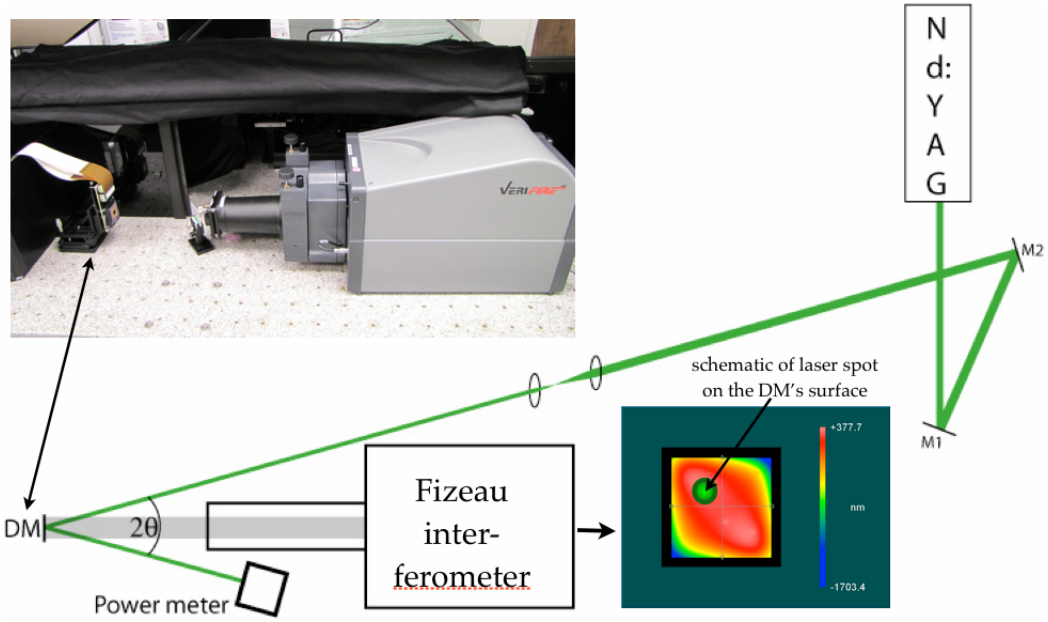

Figure 2.5: Schematic of the laser testbed setup at the Laboratory for Adaptive Optics. The laser light travels 2.5 meters before striking the surface of the DM, which is monitored by the Fizeau interferometer. A telescope pair of lenses is used to decrease the beam size incident on the DM, thus increasing the irradiance on the DM. A simulated Gaussian profile beam diameter is depicted as the green spot on the DM surface profile (nm surface) shown to the right of the Fizeau interferometer. The inset image at the upper left shows the BMC DM and ribbon cables with the interferometer pointed at the surface of the DM.

The beam at the location of the DM is nominally 3.5 mm in diameter. During tests in which it was desired to increase the irradiance on the DM, a telescope pair of lenses was inserted along the beam path. This resulted in a 1.75 mm beam size at the location of

the deformable mirror.

A Zygo VeriFire AT+ Fizeau interferometer placed normal to the DMs surface recorded the response of the DM to incident laser light. The 27 cm focal length and body geometry of the interferometer defined the limiting incidence angle θ of 12.3°. A 633 nm bandpass filter (not shown in Figure 2.5) was placed just in front of the Zygo lens at a 45° angle to protect any scattered laser light from reaching the the interferometers CCD.

2.3.5 Test procedures

The following test procedure was used to examine the response of each MEMS deformable mirror to the Nd:YAG laser:

1. Select either the 1.75 or 3.5 mm beam diameter.

2. Select the location on the DM for the laser beam to be located. Areas were selected that were deemed far enough from the edges of the device but not too close to any broken actuators.

3. Ramp the laser power from 0 to 2 Watts in 0.1 Watt increments.

4. Measure the surface response (and hence phase distortion) of the DM at each laser power interval.

5. The next step at the maximum power of 2 Watts was to either:

(a) shutter the laser switch—laser power goes from 2 to 0 Watts without going step-wise back to 0 Watts;

(b) perform closed-loop control of the DM; or

(c) continue to monitor the DM surface over 7 continuous hours of exposure to 2 Watts.

2.3.6 Response of MEMS deformable mirrors to incident laser-light

Zygo images capturing the response of the aluminum-coated continuous-facesheet BMC deformable mirror to increasing laser power are shown in Figure 2.6.

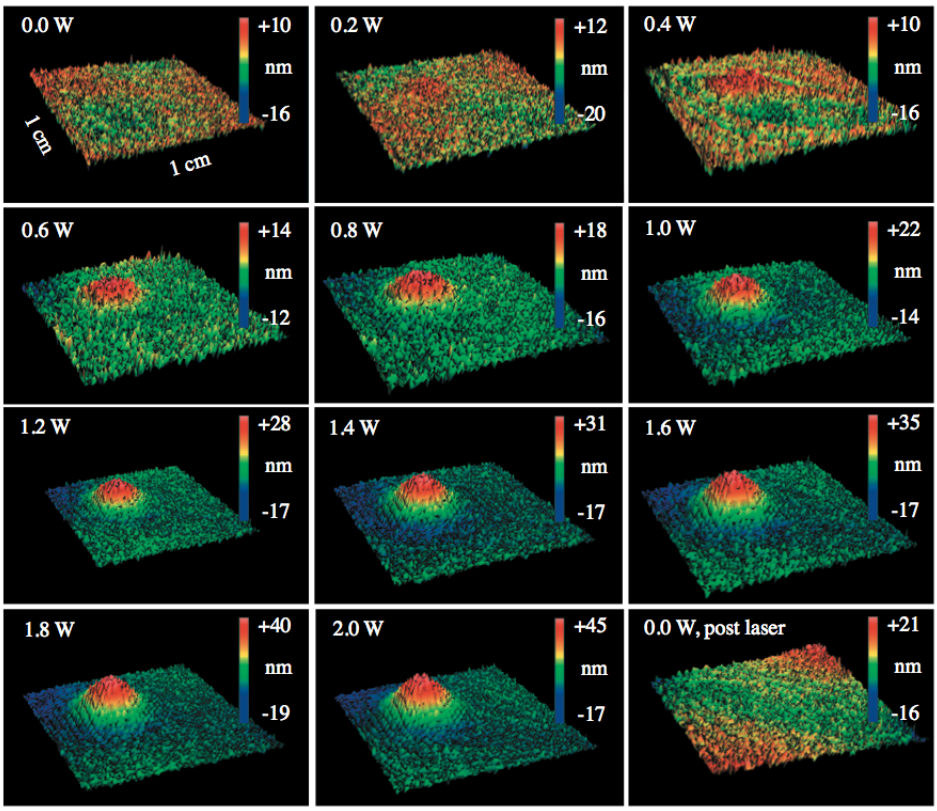

Figure 2.6: Zygo images capturing the surface response of the continuous-facheet, aluminum-coated BMC deformable mirror to increasing (left to right, top to bottom) incident laser light. The laser spot covers roughly 100 actuators.

The first image in Figure 2.6 (top left) is the result of two consecutive measurements subtracted from each other to show the $\sim$ 1 nm rms noise floor of the Zygo instrument. Images left to right, top to bottom, show the surface response of the DM to increasing levels of laser power. At 200 mW there is a slightly detectable upward bow of the DM's surface. This bowing is most likely caused by thermal expansion of the surface due to spot heating. The bowing of the surface continues to increase as the laser power

increases, reaching a maximum of 53 nm Peak-to-Valley (PV) surface deflection at 2 Watts for this device. When the laser is shuttered (returns to zero Watts without ramping down in power) the DM surface returns to its initial shape faster than the 10 second sampling rate of the interferometer. The DM was then removed and inspected with the Olympus microscope. No permanent damage was detected for this device.

The response of the continuous-facesheet protected-silver BMC DM was tested next. For this test, the telescope pair was inserted along the path of the laser. This decreased the spot size on the DM to 1.75 mm, thus increasing the irradiance. Eighty five percent of the Gaussian beam power is contained within $\sim$ 1 mm of the beam‘s diameter. This corresponds to roughly 3 actuators across (pitch = 300 um). The same test procedure was followed, and the recorded Zygo image with the laser set at 2 Watts is shown in figure 2.7 on the left.

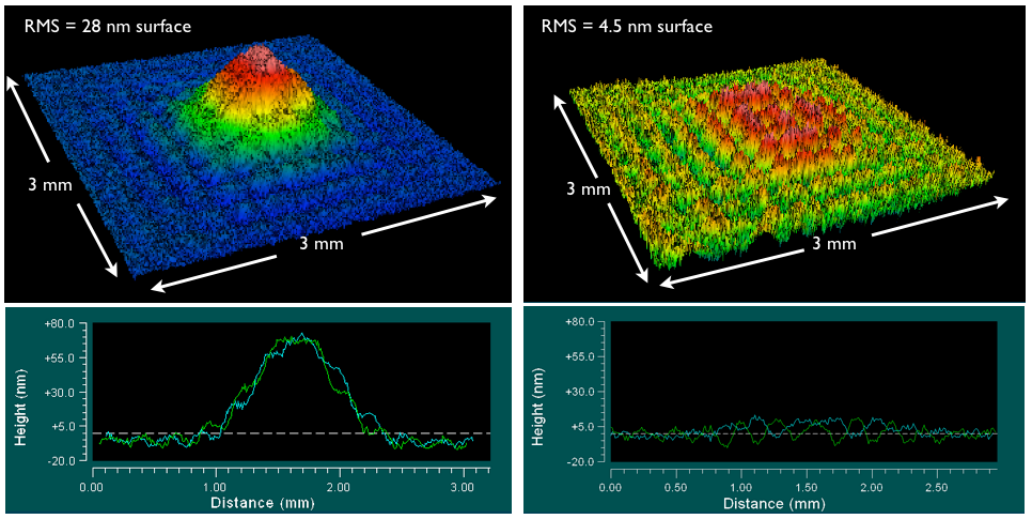

Figure 2.7: Left) Response of the continuous-facesheet protected silver-coated BMC DM to a 2 Watt, 1.75 mm laser beam. Right) Resulting DM profile with the laser still present at maximum power, but after closed-loop correction resulting in the majority of the deflection being compensated.

A PV surface deflection of 68 nm is measured for this device. Unlike the aluminum-coated DM, this device was able to be electrostatcially actuated. This allowed us to perform closed-loop control of the surface with the laser still incident on the DM. The result after closed-loop correction is shown on the right of Figure 2.7. This confirmed that the mirror was still functional and that the low-order, laser-induced surface deflection is able to be actively removed. However, spot heating is observed to affect the DM at spatial frequencies greater than the pitch of the actuators. This can be observed in the lineout of Figure 2.7 on the lower right.

All of the actuators were then set to zero volts and the laser was shuttered off. A Zygo image was captured 10 seconds late. The result is shown on the left of Figure 2.8. The surface of the deformable mirror is observed to deflect downwards on the order of 15 nm. A measurement of the same region recorded 50 minutes later is shown on the right of Figure 2.8, showing the mirror trending towards its original flat shape. The surface did eventually return to its initial state nearly 90 minutes later.

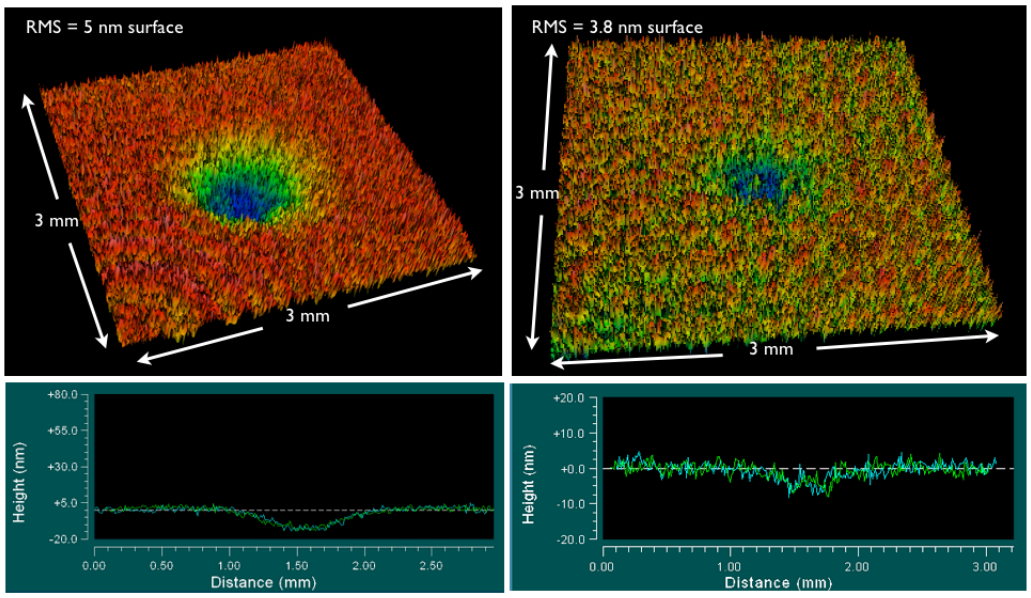

Figure 2.8: The response of the continuous-facesheet protected-silver deformable mirror after 10 seconds (left) and 50 minutes (right) post 2 Watt laser incidence. The mirror‘s surface did eventually return to its initial flat position.

This DM was then removed from the test bench and the Boston Micromachines‘ segmented DM was inserted in the test bench. The same test procedures were followed for this DM. The response of the SLM to the 1.75 mm beam at 2 Watts is shown in Figure

2.9.

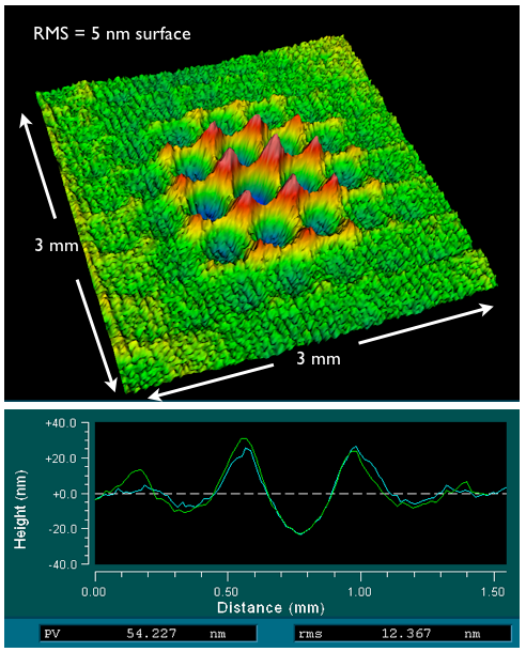

Figure 2.9: Response of the BMC segmented DM to 2 Watts incident laser power. Lineouts along the hypotenuse show that spot heating causes each actuator‘s bow to increase.

In contrast to the response of the continuous facesheet DMs where the surface is observed to bow outwards, the SLM segments deflect inwards under the presence of the optical power. As can be seen in the horizontal lineout, the center point of the the individual actuators deflects inward. A maximum PV deflection 54 nm surface is measured.

Next, an aluminum-coated DM from Iris AO was tested under the same conditions. This mirror was tested with the telescope pair of lenses inserted along the laser path so that the area of the laser would fall on an inner 7 segments of the device and allow for

reference measurements to be made relative to stable segments on the perimeter.

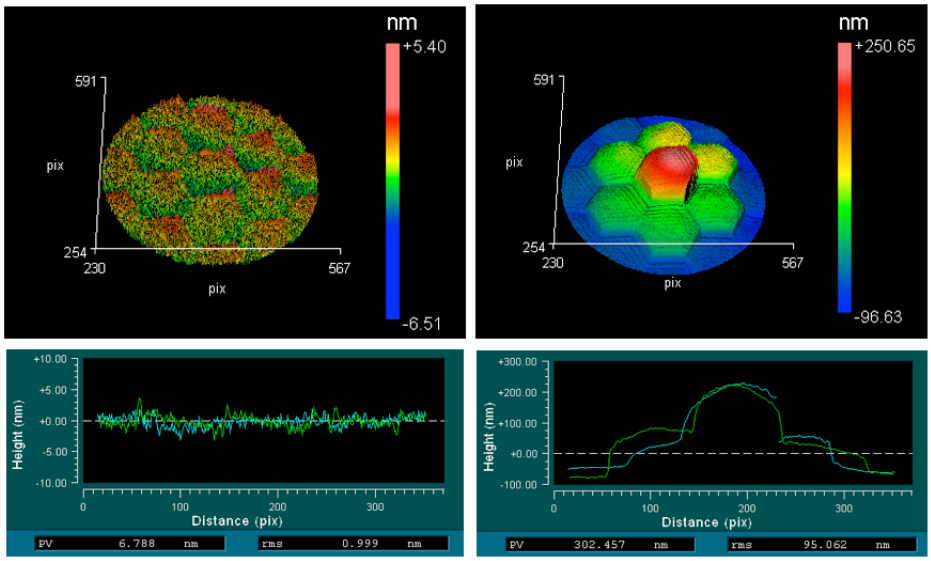

Figure 2.10: Difference image (left) of two images of the DM in its unpowered state showing the noise floor of the Zygo interferometer. Same region of the DM, showing the response of the segments to incident 2 Watt laser power.

The noise floor of a difference image between two Zygo measurements is shown on the left of Figure 2.10. With the laser at 2 Watts, the segments are measured to deflect upwards out of plane, which is consistent with the response of the continuous-facesheet DM from Boston Micromachines.

To summarize the above results, measurements of the DM's peak surface deflection as a function incident irradiance (W/cm^2) are plotted in Figure 2.11.

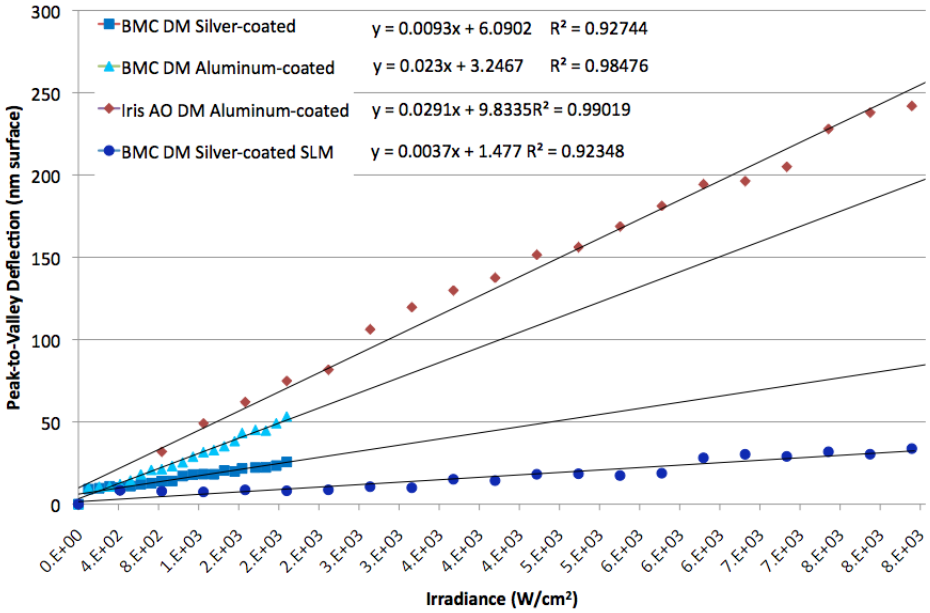

Figure 2.11: Measurements of the Peak-to-Valley surface displacement as a function of the incident laser irradiance for each of the metal-coated MEMS DMs.

The response of each device is observed to be highly linear. The surface response of the aluminum-coated DMs is greater than that of the protected-silver DMs. This behavior can be attributed to the lower reflectivity of aluminum (R=91% at the 532 nm laser wavelength) compared with that of silver (R=96.5%). However, microscope images revealed that the surface of the protected-silver continuous-facesheet BMC deformable mirror did experience permanent damage, in the form of annealing of the protective coating.

A linear least-squares fit to each DM allows us to project the expected response of each DM to the 10 Watt average optical power typical of the laser guidestar at Mt. Hamilton.

For example, the expected surface displacement for the aluminum-coated Iris AO DM at an irradiance of 1.04×10^4 Watts/cm^2 (10 Watts over the 3.5 mm working aperture) would induce 96 nm of displacement. As was shown in the laboratory, a deflection of this order could be corrected for and, in principal, incorporated into the closed-loop control algorithm.

Support from the National Science Foundation Grant No. IIP-1014435 allowed Iris AO to develop dielectric coatings for their DMs. Up until then, dielectric coatings had yet to be integrated on any MEMS deformable mirrors from either BMC or Iris AO. Iris AO was able to successfully implement these coatings for applications at several wavelengths [29]. Two of these wavelengths included the 532 and 589 nm wavelengths. Several of the 532 nm coatings were received and tested at the LAO. Figure 2.12 shows an image of one of the dielectric-coated Iris AO DMs.

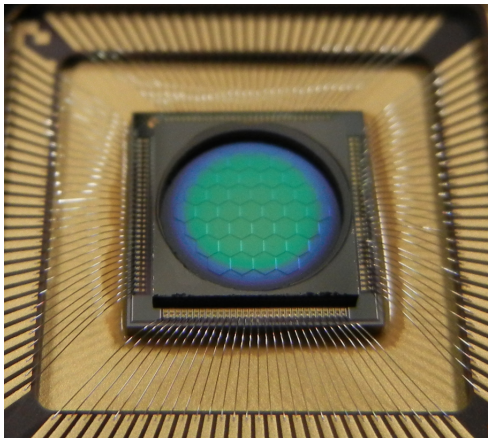

Figure 2.12: Iris AO PTT111 DM with a 532 nm, dielectric-coating deposited over the 3.5 mm working aperture.

The dielectric coating (green hue) fills the 3.5 mm working aperture of the device in the above image. The alternating layers of index of refraction that constitute the dielectric-coating total 2.58 μm in thickness. Lattice Electro Optics produced these coatings that give the DM a measured reflectivity of 99.75

The dielectric-coated mirror was initially tested in the same setup as the metal-coated DMs. Under this setup, no response of the deformable mirror‘s surface to the incident laser light was observed. Thus, the laser test setup was adapted to introduce a larger irradiance to the surface of the DM to test the damage threshold of this device.

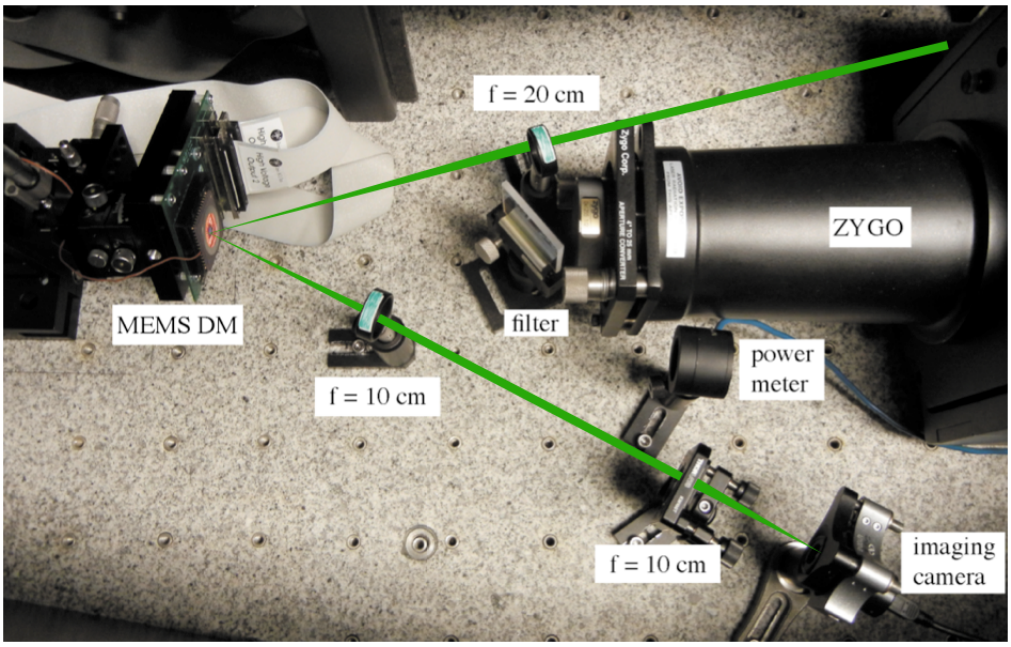

Figure 2.13: Same underlying testbed layout as before, but updated with a 200 mm focal length lens to focus the laser beam onto the dielectric-coated DM.

To increase the irradiance on the deformable mirror, a 20 cm focal length was then

inserted along the laser path. This created a 50 μm diameter spot, or equivalent maximum irradiance of 1.02×10^5 Watts/cm^2. A pair of 10 cm focal length lenses was used to enable the imaging camera to see the location of the LGS spot on the DM.

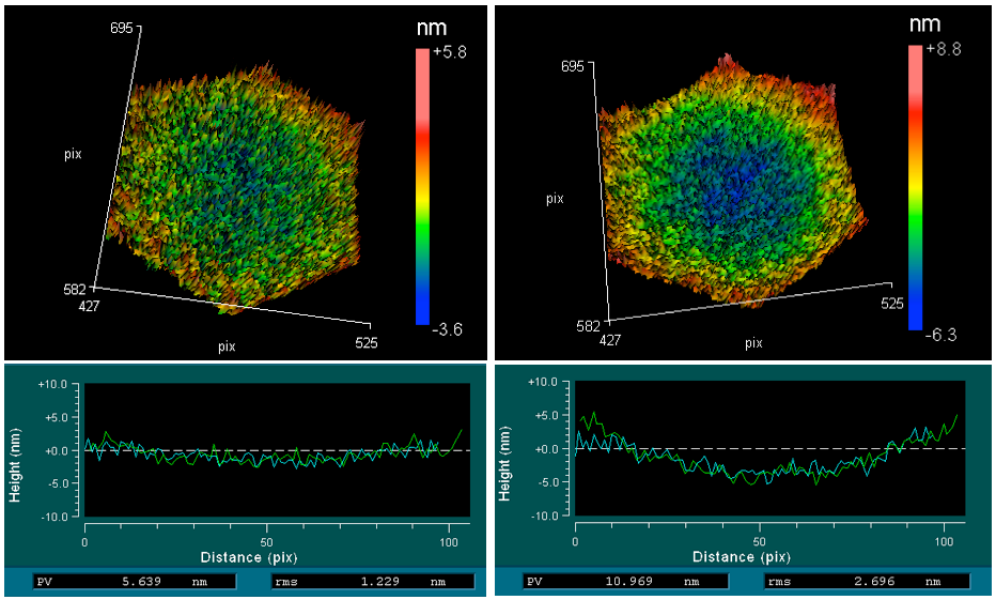

Figure 2.14: Left) response of segment 7 of the dielectric-coated Iris AO DM with the 2 Watt laser beam focused on it. Right) The same segment after an hour of continuous exposure to the 2 Watt laser.

Figure 2.14 shows the response of segment 7 on the dielectric-coated Iris AO DM. The left image is a difference image recorded when the laser first reached is maximum power of 2 Watts. The image on the right shows the same segment, after continuous exposure to the 2 Watt beam for one hour. A slight change of roughly 5 nm PV in the surface of the segment is observed, though this amount of deflection is acceptable for our application.

2.3.7 Discussion and Conclusion

The response of several MEMS deformable mirrors to incident, high-power visible wavelength laser light has been characterized. Spot heating induced by the laser causes the surface of each mirror to bow out of its original plane. The displacement of the DM‘s surface is observed to be highly linear and was shown to be controllable.

A dielectric-coated deformable mirror from Iris AO was able to withstand optical fluence levels typical of continuous-wave laser uplink-AO applications, with nearly no change in its surface figure profile. Independent tests by Iris AO showed that the dielectric-coatings at 355 nm could survive peak power densities of 130 MW/cm^2 [30]. Information from these experiments was used to drive the design of the uplink-AO system.

2.4 The Shane 3-meter Telescope‘s Laser Guidestar Facility

The Shane 3-meter telescope‘s sodium dye laser was developed at Lawrence Livermore National Laboratory (LNLL) and delivered to the observatory in 1995 [33]. The laser consists of four flash-lamp pumped frequency-doubled solid state (Nd:YAG) pump lasers which are located under the dome floor to avoid generating heat in the dome [34]. Energy from each pump laser is transmitted in 150 ns, 10 kHz pulses with 10 MW/cm^2 peak powers (10 Watts average power) via optic fiber cables to the dye cell located on the side

of the 3-meter telescope. Though typical average output laser powers ranged from 13 to 18 Watts [35] during the first few years of operation, the laser efficiency has steadily decreased, and only 3.5 Watts of average power was available during our uplink-AO experiments. This low amount of power has recently been attributed to a repairable problem with the dye master oscillator.

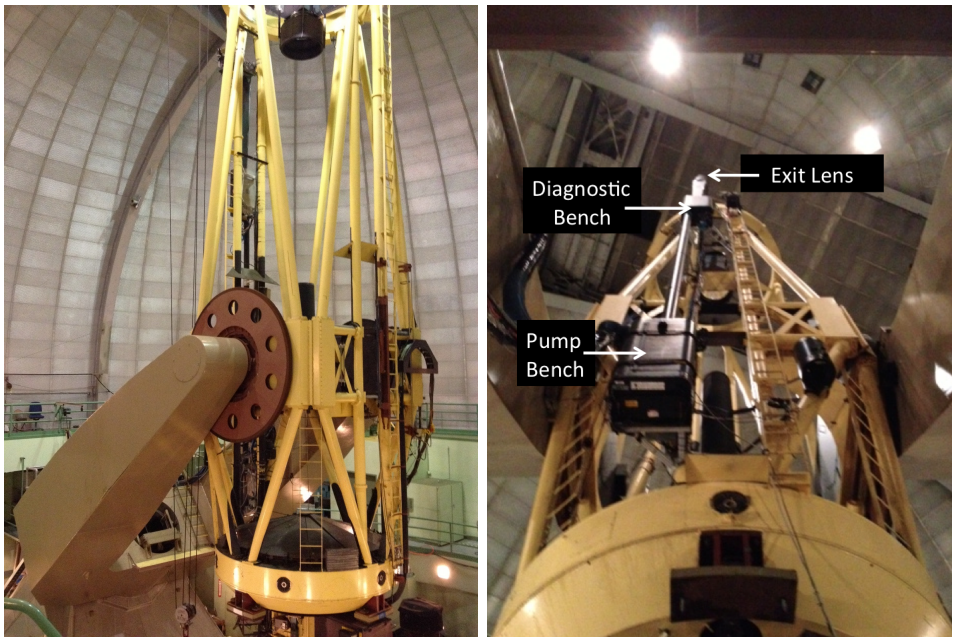

Figure 2.15: Left) The Shane 3-meter telescope at Mt. Hamilton. Right) Components of the 3-meter‘s laser launch telescope as seen looking up the side of the telescope

The beam transfer optics (BTO) system at Mt. Hamilton is mounted in a side-launch configuration on the Shane 3-meter telescope. The BTO consists of two main compartments; the pump bench, mounted near the primary mirror and the diagnostic bench, mounted near the secondary mirror. On the pump bench, the seed and pump lasers

are combined in the dye cell to generate the high power laser light tuned to the sodium D_2 line. The laser then free-space propagates to the diagnostic bench. Cameras in the diagnostic bench are used to monitor the pointing and centering of the outgoing laser beam. The tip/tilt mirror used to stabilize the LGS spot in the mesosphere is also located on the diagnostic bench.

Recently, phase aberrations in the LGS beam have affected the size and shape of the LGS spot profile. A typical image of the LGS spot as recorded by the guider camera on the Shane 3-meter telescope is shown on the left in Figure 2.16. This image is captured with the guider camera which is located after the primary of the telescope but before the AO system, so it measures the effects of the atmosphere on the LGS beam as it propagates to and from the sodium layer. Each pixel on the camera is 0.512 arcseconds in angular extent.

For comparison, a simulation of the expected spot profile for the launch geometry of the Shane AO launch system is shown image right of Figure 2.16. This simulation results from the convolution of the diffraction limited PSF with 100 random, statistically accurate, Kolmogorov phase screen realizations with $r_o = 12$ cm for both the upward and downward path of the laser light.

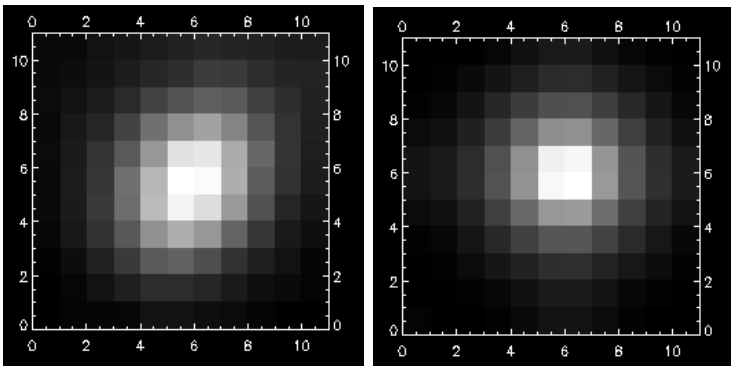

Figure 2.16: Left) Typical guider camera image of the LGS spot measured at Mt. Hamilton. Right) Simulated LGS spot seen with the guider camera with $r_o = 12$ cm Kolmogorov turbulence.

This persistent spot profile indicates that there is a quasi-static aberration along the round trip path from the laser launch telescope to the sodium layer and back through the primary of the Shane 3-meter telescope. This spot profile adversely affects the performance of the Shane 3-meter AO system in several ways. The Shack-Hartman WFS measurement error scales linearly with the angular size of the reference source, rising rapidly as the spot size increases. Furthermore, a factor of 2 decrease in spot size is equivalent to a factor of 4 in laser power [35] in the mesosphere. With the low laser power levels during our observing night, the flux was still above roughly 5 W/cm^2 [33] saturation level of the sodium atoms, and the simulated decrease in spot size should result in an increased photon flux returned from the sodium layer thus decreasing the closed loop bandwidth error of the AO system.

The goal of the uplink-AO system was to remove the slow time-varying phase aberra-

tions along the LGS beam producing a more compact and more uniform spot in the mesosphere, thus improving the performance of the Shane 3-meter AO system.

2.5 First on-sky demonstration of laser-uplink AO with a MEMS DM

Integrating an adaptive optics system into the laser launch path presented unique challenges. One of the main concerns was designing a system that could easily be introduced into the current LGS path and required a minimal number of modifications to the existing system.

The most immediate questions were 1) where will the AO system be located, and 2) how can the system be controlled?

Previous measurements revealed that the laser beam in the diagnostic bench was roughly 10 mm in diameter. This beam size is larger than the 3.5 mm working aperture of the Iris AO PTT111 MEMS DM. Measurements of the laser beam diameter in the pump bench confirmed that the diverging laser beam diameter ranged from 2 to 5 mm, depending on the position between the dye cell and the first collimating lens. Careful consideration of physical constraints and limitations resulted in the design of an uplink-AO system that could be placed on the pump bench.

2.5.1 Components of the uplink-AO system on the pump bench

A schematic of the uplink-AO system is shown in Figure 2.17. The uplink-AO system‘s optical bench is roughly 28 × 33 × 20 centimeters. The LGS light traverses vertically through the schematic at a height of 115 mm above the existing optical bench (not shown in the schematic). Existing optical equipment on the pump bench required that the uplink-AO bench be mounted roughly 100 mm above the pump bench‘s optical table. This constraint required that optical elements of the uplink-AO system be located 50 mm from the bench in order to intercept the outgoing LGS beam. Furthermore, the distance from the uplink-AO bench to the enclosing safety door required that no optical component of the uplink system could be higher than 80 mm above the height of the laser beam.

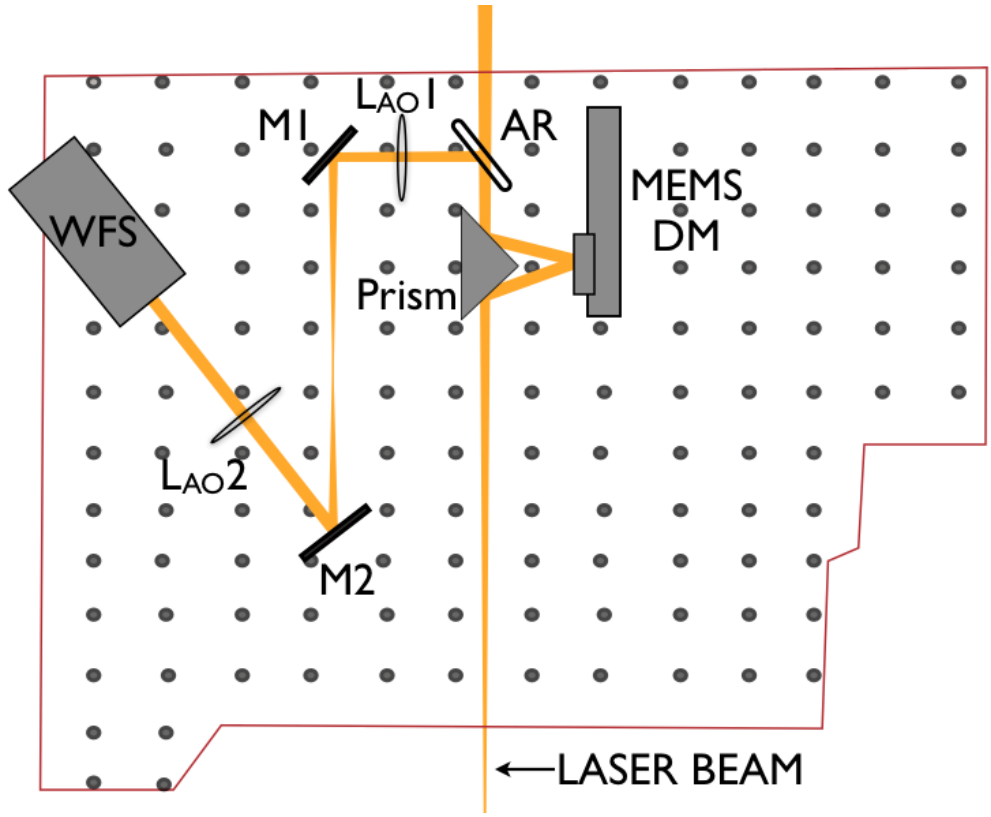

Figure 2.17: Schematic of the MEMS DM-based uplink AO system.

These physical constraints drove the cutout of the optical board and placement of the uplink-AO's components and mounting hardware. It also provided the information needed to build and test the uplink-AO system at the Laboratory for Adaptive Optics in conditions that simulated the beam diameter and divergence angle of the LGS beam. This allowed the uplink-AO system to be delivered with the components already aligned.

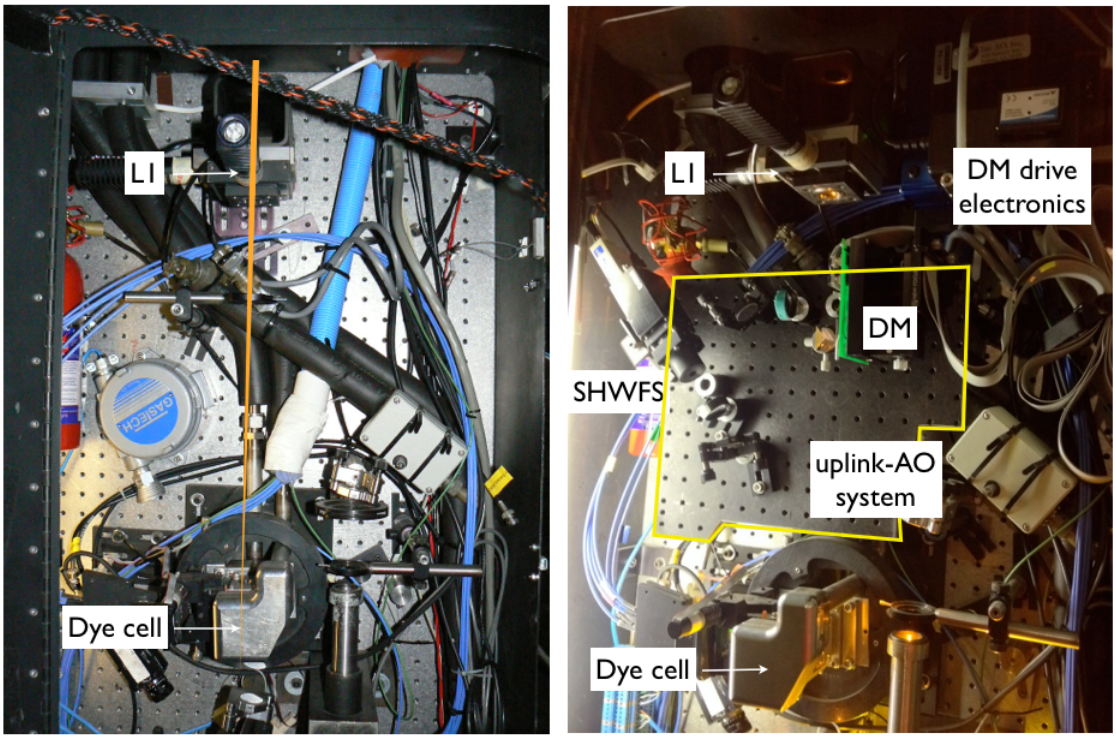

Figure 2.18: The pump bench pre- and post-integration of the uplink-AO system. The integrated optical board of the uplink system (outlined in yellow) sits above all of the existing components in the left image, at a position such that the diverging LGS beam was approximately 3.2 mm on the DM.

The exact path of the LGS beam through the pump bench (Figure 2.18) was unknown to within 2.5 cm, so three Newport BUP-2 freely rotating slotted bases were mounted to the optical table of the pump bench. This allowed us to correctly position the uplink-AO system relative to the path of the sodium laser beam, and then secure the system in place.

Power supplies and the deformable mirror drive electronics were also mounted on the pump bench and can be seen on the top right of Figure 2.18.

The uplink-AO optical components were designed with custom coatings to maximize the amount of light reaching the sodium layer. The first component the laser light encounters is the prism. The custom prism was manufactured by Precision Optical. The prism is made of corning 7980 grade 0 - A, with a quarter wave surface flatness, ± 2 arcminute angle tolerances, and a surface quality of 40-20 over the two 15 x 9 and 23.8 x 9 mm faces. Though the prism is typically used as a dispersive prism, a custom metal coating was deposited on the two 15 x 9 mm faces for the purpose of this experiment.

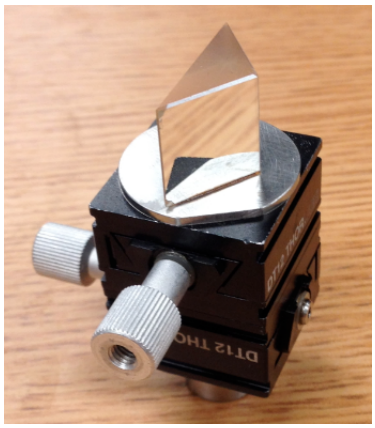

Figure 2.19: The custom prism showing one facet (15 x 9 mm) with the protective silver coating. The prism is used to direct the LGS beam to the DM and then back along the LGS beam‘s original path.

The prism‘s custom coating was performed by Andrew Phillips and the team at the

Lick Observatory's Optical coating shops located on the UCSC campus. A layer of silver deposited on titanium nitride, then coated with ytrium fluoride and titanium oxide, was deposited onto the two facets of the prism. The prism's theoretical reflection curves as specific for the 52.5 ° incidence angle are shown in Figure 2.20. For the P and S polarization planes the reflectance at the 589 nm wavelength is 99.7% and 98.7%, respectively. The average reflectance of these two planes, with an R = 99.2% is assumed as the actual reflectivity since the polarization plane of the laser is unknown.

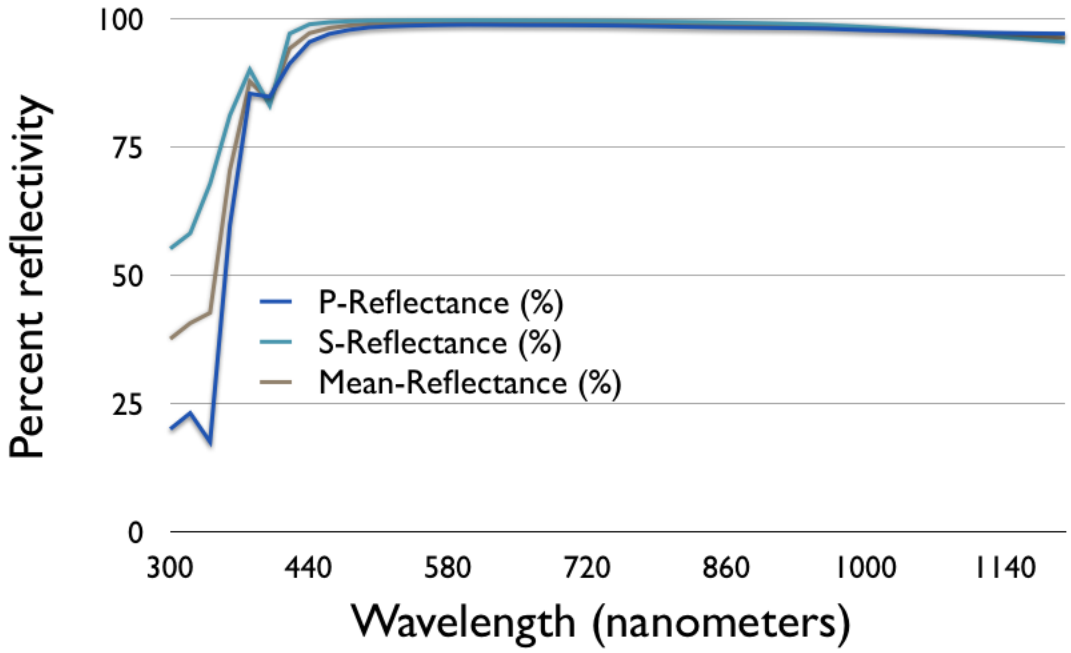

Figure 2.20: Theoretical reflectivity curve of the prism's coating as a function of wavelength. The coating is designed to give a reflectivity of 99.2% at 589 nm.

The prism was bonded to a piece of aluminum that was mounted onto a Thorlabs Inc. x-y stage. This allowed for fine alignment of the prism's apex with the center of the

deformable mirror. The prism‘s apex angle of 105° was specifically designed for two reasons: to minimize the distance the LGS light would travel to the deformable mirror and back to its initial path and secondly, to ensure the laser light was incident on the DM at 15° relative to normal since the custom DM‘s dielectric coating had been previously designed for this angle.

Laboratory acceptance tests with various MEMS DMs and coatings indicated that a dielectric-coated DM was ideal for this application [29] [30]. However, more recent tests performed by Iris AO concluded that an Iris AO DM with a protective silver coating was capable of meeting the LGS power requirements. Thus, it was decided to perform the experiment with a protected-silver MEMS deformable mirror.

The Iris AO DM used in the uplink-AO experiments is shown in Fig. 2.21. Each segment of this DM can be controlled in piston tip and tilt motion, allowing for 111 degrees-of-freedom. Each segment is capable of 5 microns of surface stroke and can repeatably return to an initial position within a nanometer [32]. The 8 μm gap between each segment and silver coating resulted in roughly 10% of the outgoing LGS light being lost to the DM.

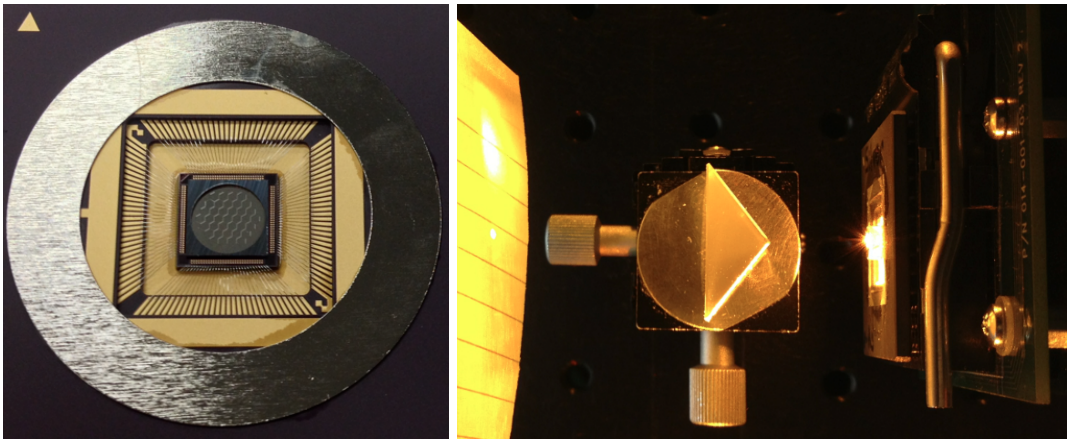

Figure 2.21: Left) The protected silver-coated IrisAO deformable mirror. The DM has 111 degrees of freedom and a 3.5 mm working aperture. Right) Close up image of the prism and DM. The DM is positioned to the right of the prism.

The uplink-DM was mounted to a goniometer providing fine-control of the outgoing LGS beam‘s angle. Light reflected from the deformable mirror encountered the second reflective facet of the prism. The thickness of the silver coating on this side of the prism was specifically tuned so that of the 1 percent of light not reflected by the prism‘s coating, 0.00001% of this light would transmit through the prism and be sent to the Shack-Hartmann Wavefront Sensor (SHWFS). This transmitted light can be seen hitting the index card in the upper left image of figure 2.21. However, this effort later proved too difficult to work with due to contamination by scattered light.

As an alternative method to get light to the SHWFS, an optical flat lens, 1 inch diameter and a quarter inch thick, was coated with a custom anti-reflective (AR) coating and placed after the prism. The AR-coated window is shown in Figure 2.22.

Figure 2.22: The 1 inch diameter, anti-reflective coated window. The AR window was placed just after the prism, to direct a small amount of the laser light to the SHWFS.

The AR coating is designed to send 0.2 percent of light reflected from each surface of the window is purposefully sent to the relay optics and the SHWFS. The AR window was placed at a 45 degree angle to the LGS beam after the second reflective side of the prism.

One of the reflected beams from the AR window was blocked, while the other beam passed through a telescope pair (LAO1 and LAO2) of 100 mm focal length lens, used to conjugate the DM surface to the SHWFS lenslet array. M1 and M2 are a pair of fold mirrors used to steer the beam into the WFS. Though the amount of light transmitted by the AR window was still above the saturation levels of the wavefront sensor, a neutral density (ND) filter and the ability to remotely control the frame rate of the camera allowed us to monitor the phase of the LGS beam at all of the various power level settings.

This setup worked in the laboratory and enabled closed-loop wavefront control at 30 Hz.

Unfortunately, however, the lateral shift in the LGS beam caused by passing through the AR window resulted in the LGS beam being clipped by a baffle located shortly after the existing collimating lens in the pump bench. Not being able to pass the LGS light to the diagnostic bench rendered the SHWFS path for controlling the uplink DM inoperable. Hence, an alternative wavefront sensing method was used, based on the point-spread-function (PSF) camera loop.

2.5.2 Components of the uplink-AO system on the diagnostic bench

Even if we could have used information from the SHWFS to direct control of the phase of the outgoing LGS beam, it might not have been the most ideal method for the following reason — the SHWFS has no knowledge of aberrations introduced to the beam during the approximately 12 meter path from the pump bench to the diagnostic bench, where the LGS beam encounters several more optical components before exiting. Furthermore, correction of any non-common path aberrations along the SHWFS would serve to corrupt the quality of the outgoing beam.

Aware of this concern going into the design of the uplink AO system, we decided to integrate a point spread function (PSF) camera in the diagnostic bench. An image sharpening control algorithm was then used to derive commands for the deformable mirror. This approach provided two main advantages over the SHWFS control loop: 1) simplicity in alignment, since the PSF camera arm required only a focusing lens, an ND filter and a steering mirror, and 2) it allowed us to monitor and control the laser‘s

wavefront along the majority of the beam transfer optics path.

The PSF camera and corresponding optics were integrated into the diagnostic bench where a SHWFS used to exist. At this location, the PSF camera is nearly 12 meters from the MEMS deformable mirror. In the same way that the LGS spot in the mesosphere is the Fourier transform of the exit pupil of the laser launch telescope, the PSF camera allows us to monitor the expected shape and size of the LGS beam in the sodium layer. Furthermore, a PSF Zernike-based control algorithm allows us to derive the phase commands for the deformable mirror that increases the flux in the sodium layer.

The components and LGS beam path through the diagnostic bench is shown in Figure 2.23. The diagnostic bench contains the tip-tilt mirror for stabilization of the LGS spot on the sky, a power meter for measuring the output laser power, a far-field and near-field camera for monitoring outgoing electric field, a pointing and centering camera for alignment of the fold mirrors, and safety shutters for emergency shutdown.

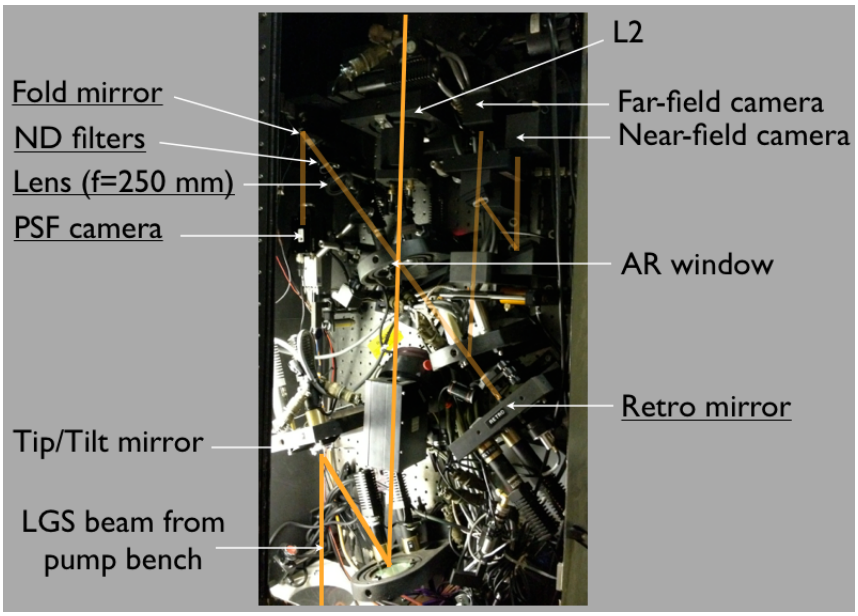

Figure 2.23: Image of the diagnostic bench and schematic of the LGS path through the optical components. The diagnostic bench was updated with the underlined elements, allowing us to perform closed loop control of the LGS beam.

To direct a small amount of the light to the PSF camera, the diagnostic bench was updated with two flat mirrors, a lens, and an ND filter (Figure 2.23). An optical flat mirror was inserted as the retro mirror which was used to pass the light back through the existing AR window and towards the PSF camera. A 1 inch lens with a 250 mm focal length focused the light to the PSF camera‘s detector. An ND4 and ND2 were combined to ensure the CCD did not saturate. This, along with being able to remotely control camera‘s shutter speed, allowed us to monitor the outgoing phase of the LGS beam over the range of optical powers. A fold mirror mounted on a tip tilt stage allowed for fine positioning of the spot on the detector. The PSF camera was mounted on a

micrometer stage for fine tuning of the CCD with the focal plane.

While it could have been possible to use the far-field camera that existed in the diagnostic bench we decided to introduce a Uniq Vision, Inc. camera model UP-600-12B as our PSF camera for the following reasons:

1. 12-Bit depth provided high dynamic range
2. A method of connecting the this camera to the control computer had already been established
3. The relatively large 7.58 x 6.15 mm chip size relaxed alignment tolerances of the laser light onto the camera
4. The 9 x 9 micron pixel size provided Nyquist sampling of the LGS far-field spot
5. The 16-level, variable electronic shutter speed would allow us to monitor the PSF quality at any LGS power level.

The digital signals were passed through 125-meter fiber optic cables via RCX C-link camera extenders from Engineering Design Team (EDT). Three fiber optic cables were routed along the side of the telescope structure linking the PSF camera, WFS camera, and the deformable mirror drive electronics to the computer in the control room.

The first laser uplink-AO experiment took place during the night of September 26, 2013. The second uplink-AO experiment took place during the night of November 26, 2013.

2.6 Laser uplink-AO experiment, September 26, 2013

The night of September 26 provided less than favorable seeing conditions. The atmospheric seeing parameter ranged from 7 to 11 cm (at $\lambda = 500$ nm) and wind speeds averaged 28 mph. Temperatures in the dome were approximately 53° Fahrenheit and humidity levels were stable at 30 percent.

2.6.1 Results from internal closed loop LGS correction

With the uplink-system integrated into the beam transfer optics, the telescope was slewed to a position 5 degrees from Zenith and the uplink-AO closed loop correction was performed.

Correction of the internal, quasi-static phase aberrations is achieved by stepping the DM through the first 12 Zernike modes (excluding piston/tip/tilt) and optimizing the integrated intensity squared recorded by the PSF camera. Each mode sweeps from negative to positive 0.25 μm rms surface figure error with a higher sampling density occurring near the DMs flat position. At each step, the peak intensity was calculated and stored for comparison with subsequent measurements. The algorithm takes roughly 90 seconds to complete.

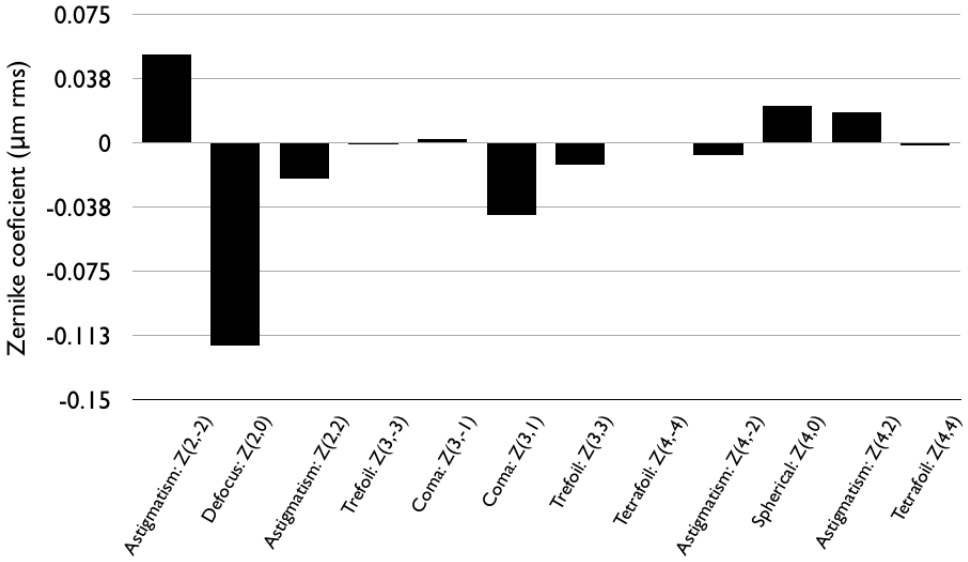

Figure 2.24: Deformable mirror Zernike coefficients (μm rms surface) resulting from the PSF closed loop optimization algorithm. The DM corrected 0.02 μm rms surface figure error.

The deformable mirror corrected 0.02 μm rms surface figure error. The Zernike coefficient for each of the 12 modes corrected is shown in Figure 2.24. One reason a small amount of wavefront correction was required could be the relatively low laser power generated this night. Of the correction provided by the uplink deformable mirror, defocus is observed to be the majority of the wavefront error. This could be a result of the PSF camera being slightly out of focus. Monitoring the return flux from the LGS spot and dynamically tuning the focus term on the DM allowed us to optimize the LGS spot on sky.

2.6.2 Test procedures and data analysis

Two metrics were available for measuring the effect of the uplink-AO system: 1) images of the LGS spot recorded with the guider camera; and 2) the performance of the ShaneAO System.

The guider camera is typically used to calibrate the position of the LGS spot. It is located behind the primary mirror of the telescope but before the ShaneAO system, so does not benefit from AO correction. The guider camera‘s CCD is a 400 × 400 pixel array with a platescale of 0.512 arcseconds per pixel. Capturing images once every second allowed us to assess the performance of the uplink-AO system by monitoring the size and shape of the LGS spot.

Effects of uplink-AO correction could also be assessed based of the performance of the Shane 3-meter AO system. The Shane AO system has an infrared science camera (IRCAL) which is a 256×256 Rockwell PICNIC array. IRCAL is sensitive to light between 0.9 and 2.5 microns and has a 0.076 arcsecond platescale, making it Nyquist sampled at 2.2 microns. This camera benefits from wavefront correction provided by the AO system. The AO system has a 61-element deformable mirror, a Shack-Hartman wavefront sensor, and is capable of 2 kHz closed loop bandwidth correction.

Creating a more uniform, more compact LGS spot should result in more photons returned from the sodium layer and thus better performance of the Shane AO system in terms of higher bandwidth correction and improved science images.

2.6.3 Guider camera images of the LGS spot

After performing the internal closed-loop correction, the uplink-DM was set to its flat position and the laser was propagated to the mesosphere. Following standard procedures, we tuned the focus of the LGS beam into the sodium layer using the existing biconcave lens (element L2 in Figure 2.23) located after the AR window in the diagnostic bench. We then switched the uplink DM it to its optimized position, and tuned the focus term on the DM to achieve the maximum flux count on the guider camera, setting this as our optimized position for the uplink-DM.

A series of 200 guider camera images was then recorded. The LGS spot FWHM values with the uplink-AO optimized are shown in dark blue in Figure. 2.25. The mean and standard deviation FWHM over the 200 seconds is measured at 3.20 $\pm$0.024" arcseconds. Note that these measurements contain the round-trip effects of atmospheric turbulence and so the size of the LGS spot in the mesosphere is taken as half of the reported value.

Near the end of the observing run, a second set of 200 Guider camera images was captured with the prism removed, i.e. with no light passing off the uplink deformable mirror. This series of 200 images is shown as the light blue plot in Figure 2.25. The measured LGS spots FWHM and standard deviation are 3.28 $\pm$0.023" arcseconds.

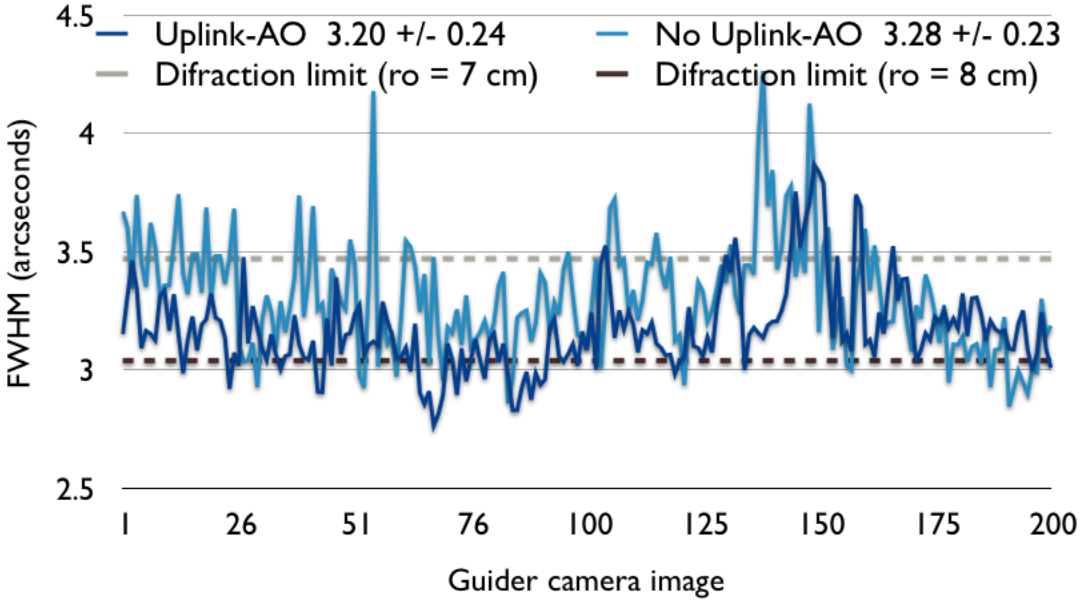

Figure 2.25: LGS spot FWHM (arcseconds) values from the round trip path as seen with the guider camera. A small improvement is detected with the guider camera when uplink-AO correction is on. Theoretical round-trip LGS spot sizes for r_0 values of 7 and 8 cm are shown as horizontal dashed line for reference.

For comparison, an LGS spot size for Kolmogorov turbulence with r_o values for 7 and 8 cm are shown for reference. A marginal improvement of 0.08 arcseconds in the mean of the spot size is observed for the case of the uplink DM in its optimized position compared with the beam transfer optics in their nominal operating state. On average, the LGS spot is smaller over the 200 seconds when the uplink-AO DM is in its optimized state as compared without the use of the uplink DM.

2.6.4 IRCAL images of star HIP 9507

The guider camera was then removed and light was directed to the ShaneAO system and into the IRCAL infrared camera. Images of star HIP 9507 were recorded in Ks-band (2.2 μm $\pm$0.21 μm . The ShaneAO system operated at 50 Hz closed-loop bandwidth.

A series of 50 IRCAL images were recorded with the uplink-AO system in its optimized state. Each image is a 1.5 second exposure. The average image of this data set is shown on the left of Figure 2.26. A 0.62" $\pm$ 0.05" FWHM is measured over the average of these 50 IRCAL measurements. The peak intensity is 246,615 counts.

The uplink deformable mirror was then aberrated with a wave of focus and astigmatism, and another set of 50 IRCAL images was recorded. The average image from this data set is shown on the right in Figure 2.26. The measured FWHM and standard deviation increased to 0.85" $\pm$ 0.16" respectively. Furthermore, the peak intensity is observed to decrease by 49% to 126704 counts.

While it was possible to show that the uplink-AO system could favorably impact the ShaneAO performance, it is important to note that the performance of the ShaneAO system with uplink-DM in its flat position was very similar (FWHM 0.66 $\pm$ 0.08") to the case when the phase correction of the uplink-DM was optimized. One explanation for this is that the internal wavefront error corrected by the uplink-DM was relatively small. Furthermore, focus was the dominant Zernike mode after closed loop correction, most likely owing to the PSF camera being slightly out of focus.

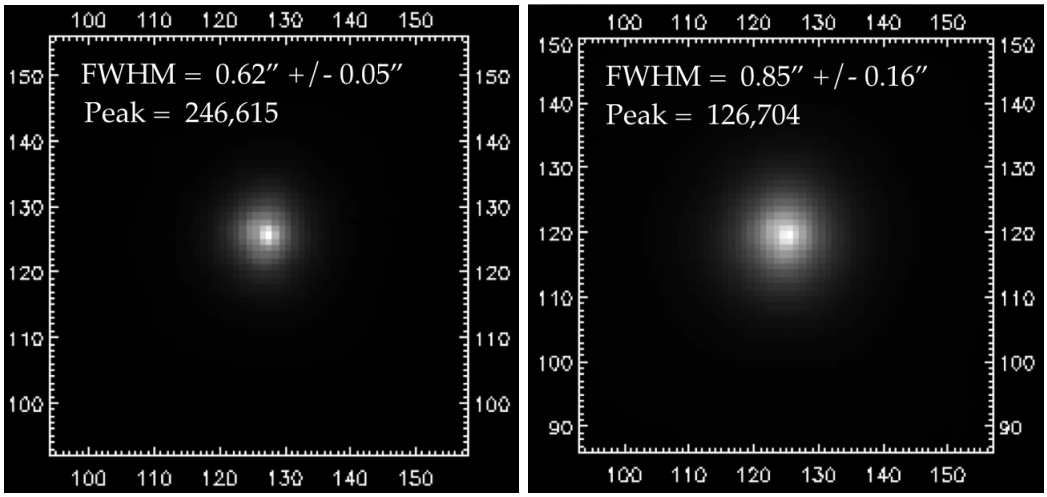

Figure 2.26: Left) Average of 50 IRCAL images of star HIP 9507 with the uplink-AO system in its optimized state. The FWHM is 0.62" ± 0.05" and the peak value is 246,615.00 counts. Right) Average of 50 IRCAL images when a wave of astigmatism and focus is applied to the uplink DM. The FWHM is increased to 0.85" ± 0.16" and the peak intensity decreased to 126,704.00 counts.

With the above IRCAL images recorded, the laser was shuttered off and we accessed the pump bench to remove the prism from the uplink-AO system (one removes the prism by loosening a screw and lifting the post from the post holder on the uplink optical board). This immediately returns the beam transfer optics setup to its initial state. The laser power was then brought back to its maximum and was propagated to the sodium layer. Standard procedures for focusing the laser into the mesosphere were performed before switching again to the ShaneAO system.

Another set of 50 IRCAL images of the same star was recorded and the resulting average

image from this data set is shown on the left in Figure 2.27. The measured FWHM and standard deviation of 0.82" ± 0.24", respectively, for the case with the prism removed are similar in performance when the LGS beam was deliberately aberrated with a wave of astigmatism and focus by the uplink DM. The peak intensity values for these data sets are also close in value.

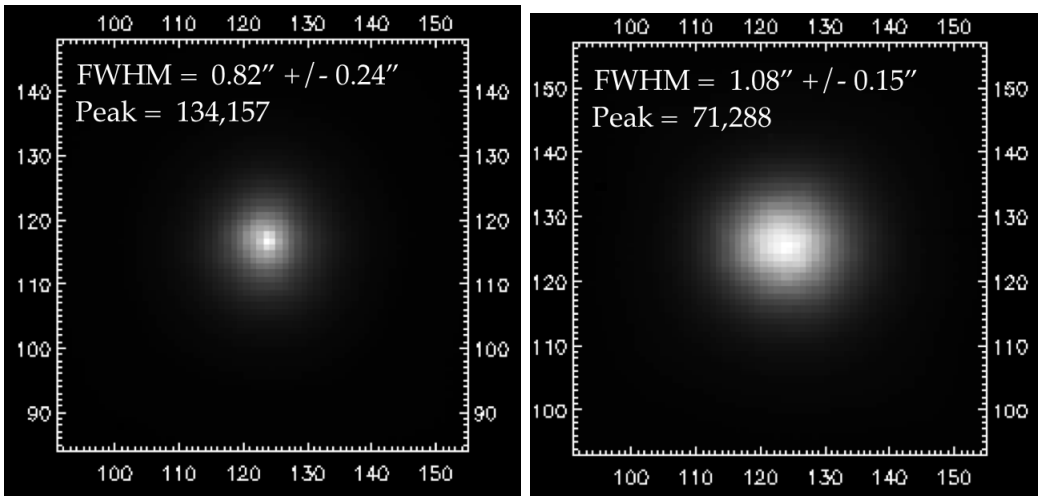

Figure 2.27: Left) Average of 50 Ircal images of star HIP 9507 with the prism removed, rendering the uplink-DM inoperable. The FWHM is 0.82" ± 0.24". Right) Resulting open loop IRCAL images. The FWHM is increased to 1.08" ± 0.15".

For comparison, an average of 50 IRCAL images with the AO system operating in open loop are shown on the right of Figure 2.27. The measured FWHM is 1.08 ± 0.15".

The performance of the Shane 3—meter AO system with the uplink-AO system in various states is summarized in Table 2.1.

IRCAL data set	FWHM (arcseconds)	Standard deviation (arcseconds)
Uplink DM optimized	0.62	0.05
Uplink DM aberrated	0.85	0.16
Uplink DM flat	0.66	0.08
Prism removed	0.82	0.24
Open Loop	1.08	0.15

Table 2.1: Results of the uplink-AO experiment for various states of the uplink and ShaneAO systems. Each IRCAL data set is an average of 50 measurements. The exposure time per image is 1.5 seconds.

The performance of the ShaneAO system is dependent on the LGS spot size in the mesosphere, an effect that could be observed by deliberately aberrating the phase of the LGS beam with the uplink-DM. However, because we did not bracket the measurements recorded with the prism removed, we do not conclude that the use of the uplink-AO system has improved the performance of the Shane-AO system when compared to the system operating in its nominal state.

2.6.5 Deformable mirror inspection pre- and post-uplink-AO

The 150 nanosecond, 10 kHz laser pulses with peak powers of 10 MWatts (3.5 Watts average during this night) were incident on the silver-coated, Iris AO MEMS deformable mirror for several continuous hours. Pre- and post-microscope images of the deformable mirror‘s surface with an Olympus STM6 microscope indicated no sign of permanent damage or degradation.

2.7 Laser uplink-AO experiment, November 25 and 26, 2013

Tuesday, November 26 2013 provided relatively good atmospheric coherence lengths (r_o = 12-15 cm at λ = 500 nm) but cirrus clouds dominated the night sky. The maximum output of the LGS laser was 3.2 Watts.

2.7.1 Results from internal closed loop LGS correction

Technical issues with the PSF camera required us to rely on the existing far-field camera in the diagnostic bench for controlling the phase of the outgoing LGS beam. Zernike modes were individually applied to the uplink deformable mirror to optimize the far-field LGS profile. The Zernike coefficients resulting from this correction are shown in Figure 2.28.

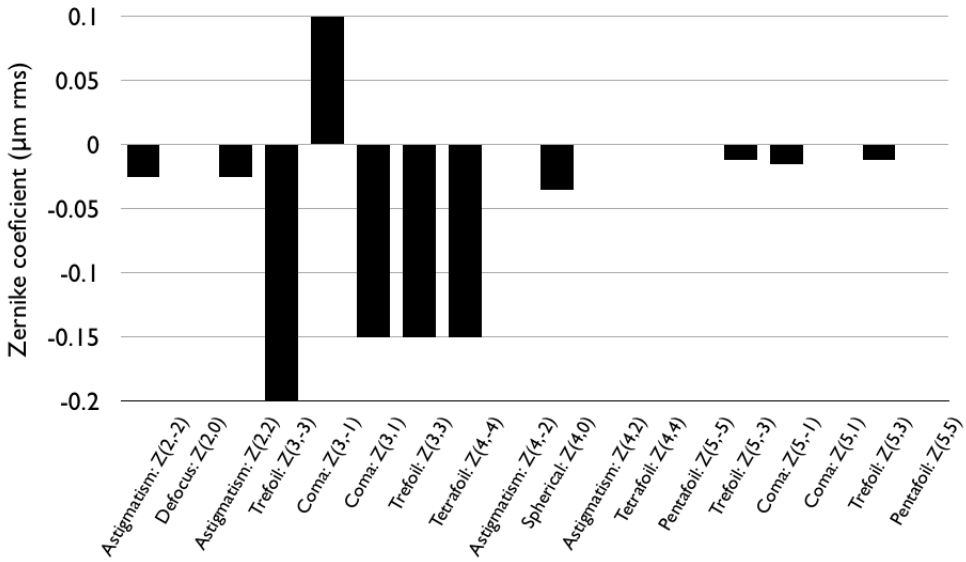

Figure 2.28: Deformable mirror Zernike coefficients (μm rms surface) resulting from the PSF closed loop optimization algorithm. The DM corrected 0.125 μm rms surface figure error.

Eleven Zernike modes were used in total. A surface figure value of 0.125 μm rms correction resulted from the optimization process.

Figure 2.29 shows the far-field spot profile recorded before (left) and after (right) optimization with the uplink DM.

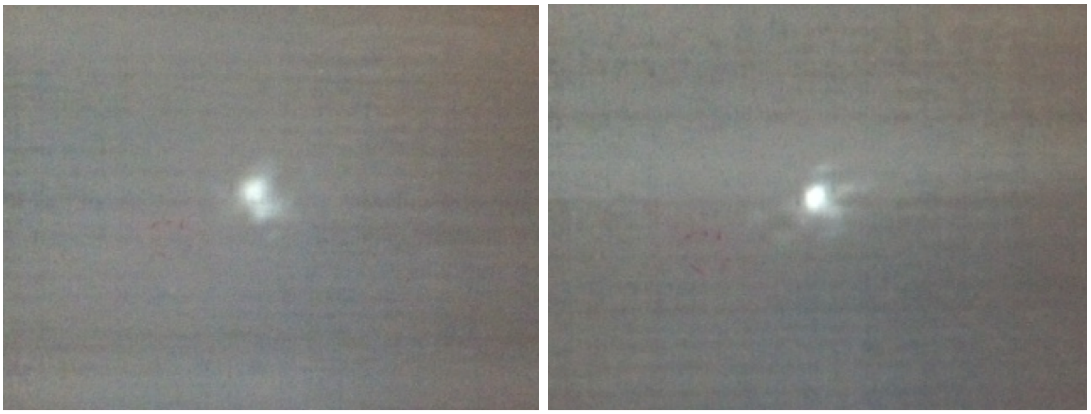

Figure 2.29: Left) Far-field profile of the sodium laser before optimization with the uplink DM. Right) Resulting far-field after optimization of 11 Zernike modes

As is evident in the images, correction with the uplink deformable mirror resulted in more energy being concentrated into a smaller area and improvements in the uniformity of the spot profile.

Over the 8 hour long observing night we had one opportunity to send the laser beam to the mesosphere.

2.7.2 On-sky Laser uplink-AO Performance

During our one opportunity to propagate the LGS beam, we were able to capture images of the LGS spot in the mesosphere with the Guider camera. These results are plotted in Figure 2.30. Images were recorded as the uplink-DM toggled between its optimized and flat positions. At each DM position, 16 guider camera images were captured. Each column in Figure 2.30 represents the average of these 16 measurements. FWHM values

are calculated by fitting a Gaussian to the average LGS spot. The values reported in Figure 2.30 are a result of a double pass of the LGS light through the atmosphere. The actual spot size in the mesosphere is half of this value.

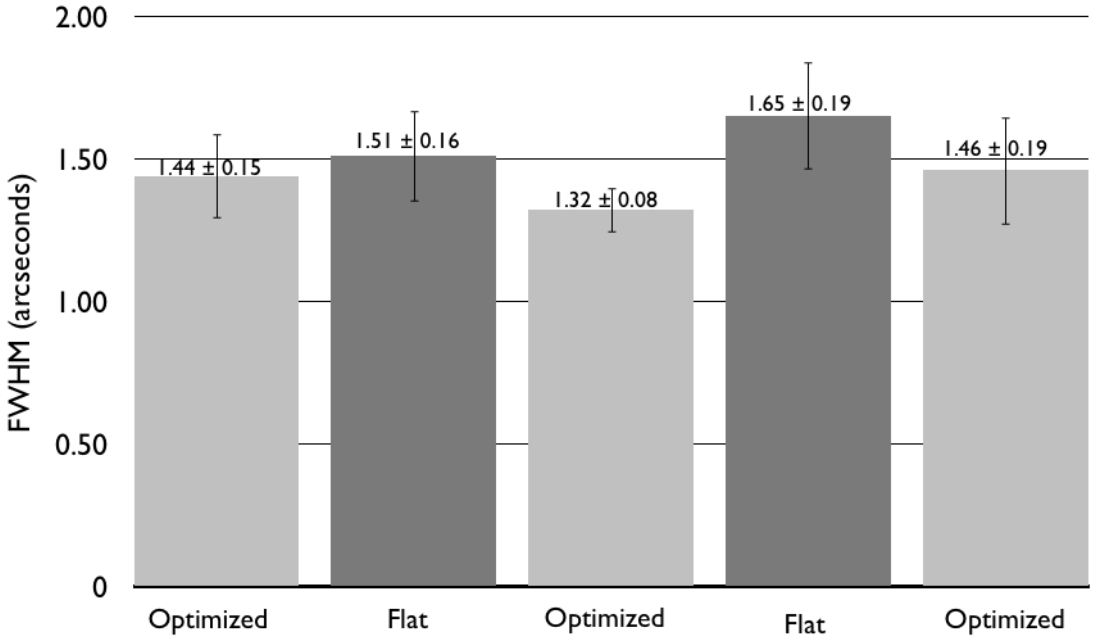

Figure 2.30: Measurements of the LGS‘ FWHM (arcseconds) spot size. Each data set represents an average of 16 guider camera images (1 second per image).

A diffraction-limited spot for our laser system‘s launch geometry would subtend 1.2 arcseconds after a round trip. Figure 2.30 indicates that uplink correction consistently provided a smaller LGS spot in the mesosphere. The average spot size with the DM at its optimized (48 measurements) and flat position (32 measurements) are 1.44 ± 0.12 and 1.62 ± 0.12, respectively.

Measurements of the guider cameras peak intensity as the DM toggled on and off are

shown in Figure 2.30. As is seen in the figure, there does not appear to be dependence on the number of backscattered photons from the sodium layer as a function of the LGS spot size.

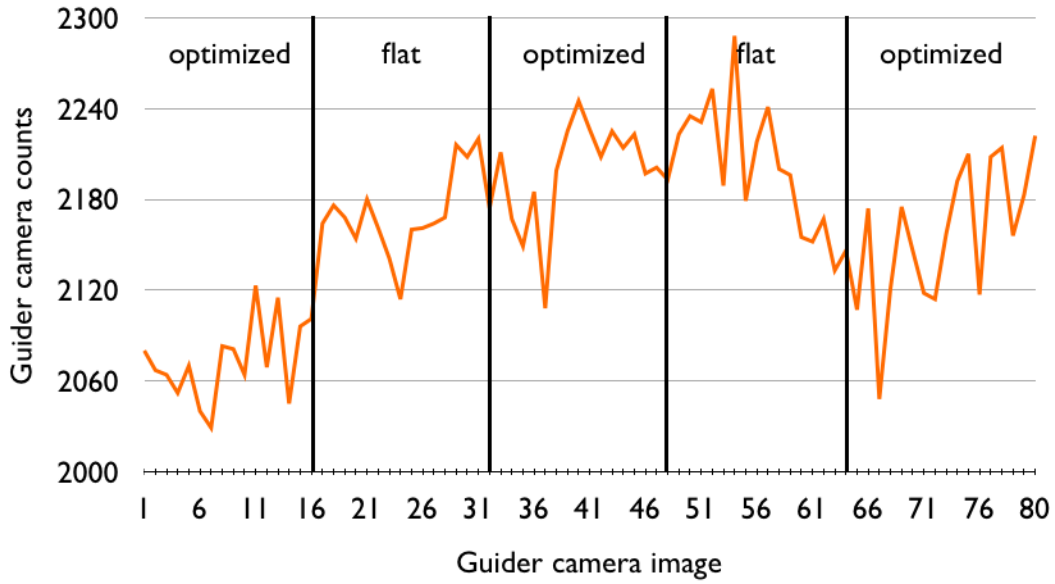

Figure 2.31: Peak flux values in the guider camera as the uplink DM is toggled between its optimized and flat position.

The measurement error of our quadcell Shack-Hartmann Sensor can be stated as

$$\sigma_{meas}(nm) = \frac{x\frac{\lambda}{r_o}d}{\sqrt{(N)}} \tag{2.1}$$

for λ 589 nm, a number of photons N of 100, r_o of 10 cm, and a subapture d of size 20 cm, the reducing the LGS spot size from 2 arcseconds to 1.5 arcseconds would decrease the measurement error by 50 nm. For the uplink experiment, the decrease in average

spot size from 1.62 to 1.44 arcseconds would decrease the measurement error by 18 nm.

A decrease in measurement error is one of the improvements we were hoping to detect. Unfortunately, cirrus clouds moved in before we could switch to the Shane 3-meter's AO system and assess the performance of this systems with the improved LGS spot.

2.7.3 Discussion and conclusion

The MEMS-based uplink-AO system enabled correction of internal, quasi-static aberrations. The system relaxed alignment tolerances, provided dynamic refocusing of the LGS spot in the mesosphere, and could provide control of flexure-induced phase distortions.

The performance of the ShaneAO system is dependent on the LGS spot size in the mesosphere, an effect that could be observed by purposefully deliberately the phase of the LGS beam with the uplink-DM.

Because we did not bracket the measurements recorded with the prism removed, we are not able to conclude that the use of the uplink-AO system has improved the performance of the Shane-AO system when compared to the system operating in its nominal state.

During our second observing night on November 26, 2013, we showed the uplink-DM consistently provided a more compact spot in the mesosphere. Two representative

images of this are shown in Figure 2.31. At its best, uplink correction decreased the area of the spot size by 36%.

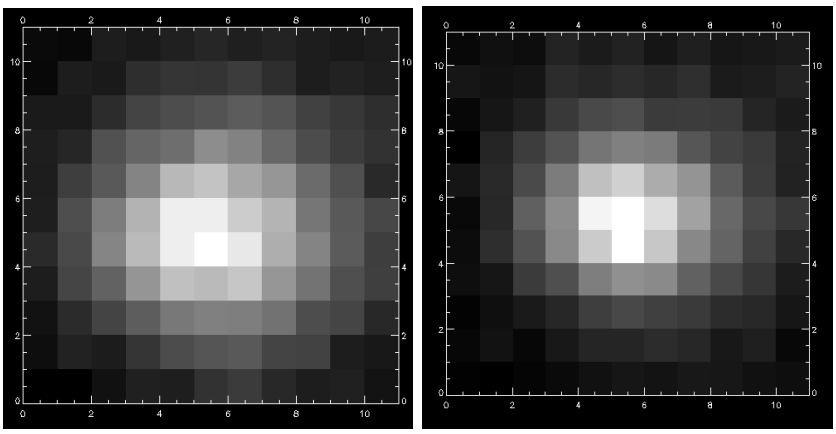

Figure 2.32: Left) Image of the LGS spot captured with the guider camera when the uplink DM was at its flat position. The FWHM is 0.00" ± 0.00". Right) Gudier camera image with the uplink-DM in its optimized state showing a smaller spot in the mesosphere. The FWHM is increased to 0.00" ± 0.00" and the peak intensity decreased to counts.

The Iris AO MEMS deformable mirror experienced several hours of exposure to average laser powers 3.5 Watts. No signs of damage to the surface or a reduction in performance have been observed.

2.8 Future directions

The ability to detect the effects of the uplink-DM on the guider camera and the ShaneAO system‘s SHWFS suggests that in the future these instruments could be used to derive the commands for the uplink-DM. This would preclude the need for the uplink-AOs SHWFS and PSF camera but still allow for optimization of the focus and LGS spot size at different pointing directions of the telescope. One future goal is to close the round trip loop by implementing the Gerchberg-Saxton algorithm to derive commands for the uplink DM from the guider camera images.

Lastly, in the same way that the uplink deformable mirror is used to conjugate the phase of the outgoing LGS beam to produce a diffraction-limited spot in the mesosphere, it is possible to use the uplink-DM to pattern the phase to generate custom LGS patterns. In principle, this technique would allow for asterisms to be generated from the single outgoing beam, create asterisms of any desired orientation, and allow the configuration to be dynamically rotated on sky.

The next section of the this thesis describes the ideas and a method for determining the phase of the electric field that will generate multiple LGS spots in the mesosphere from a single LGS beam. Simulation and preliminary laboratory results with an IrisAO MEMS deformable mirror and a spatial light modulator are presented.

Chapter 3

Using an uplink-DM as a means for producing custom LGS asterisms

Adaptive Optics (AO) correction is typically limited to a relatively narrow field of view angle along the line-of-sight of the laser guidestar. Several techniques to overcome this challenge have been proposed and even recently been employed on-sky.

Common to all of these concepts is the use of multiple reference sources (natural or artificial) arranged in an asterism within the desired science field. An AO system can then measure the turbulence along the slightly different paths to the reference sources. By shifting and averaging the wavefront sensor measurements [41], this allows for wavefront measurements of the different turbulence paths to be stitched together both radially and vertically, resulting in a 3D map of the column of turbulence above the telescope. Having this information reveals the distance to the discrete layers of turbulence above the

telescope as well as phase information over the entire window encircled by the reference sources. This enables AO correction over a field-of-view on the order of a hundred arcseconds [42] as opposed to only about 10 arcseconds when a single laser guidestar beam is used.

However, the probability of a natural asterism being located near the science target and in a desired pattern is very low. Instead, observing sites produce asterisms generated by multiple laser guidestars.

3.0.1 The need for multiple guidestar Adaptive Optics

There currently exist two methods for producing laser guidestar asterisms on-sky. The first method is to split the outgoing LGS beam into the required number of LGS beams and then launch each beam separately. This is the method used by the Gemini South GeMS adaptive optics team, which splits one 50 Watt laser into 5 different 10 Watt beams [21].

The second technique for producing LGS asterisms was developed by the team at the University of Arizona. They used a computer-generated hologram plate inserted along the beam path to control the phase of their outgoing single Rayleigh laser beam to produce the desired 5 guidester asterism [43].

Other techniques for producing multiple guidestars have been applied in biological applications, such as passing the light through a lenslet array [44] or using a DM as a

holographic phase generator [45]. In principal, these techniques could be applied to LGS asterisms for astronomy applications.

This chapter describes a technique for generating an LGS asterism by using the uplink-AO deformable mirror, inserted in the beam transfer optics of the laser launch path, to pattern the phase of the outgoing single LGS beam so as to produce a desired LGS asterism. This approach has the following advantages over the aforementioned techniques:

1. The uplink DM can be used to ensure good beam quality of the outgoing laser beam. This has already been demonstrated on-sky as described in the previous chapter.

2. In theory, the uplink-DM can be used to produce an asterism of any geometry.

3. The uplink-DM provides dynamic, real-time rotation of the LGS asterism for arbitrary beacon placement, thus negating the need for a de-rotator before each wavefront sensor

3.0.2 Producing a custom LGS asterism in the sodium layer from a single launch beam

The electromagnetic field propagating through space and time can be mathematically described as a complex field given in its simplest form as:

$$E(t,r) = Ae^{\imath(\phi(t,r))} \tag{3.1}$$

where A is the amplitude of the electric field with units of volt/meter, and $\phi(t,r)$ is the relative phase value at that instant in space and time. If at any location along the path of the traveling light field, the light is partitioned by passing it through an aperture, the complex electric field across the pupil function can be expressed mathematically as

$$Q(u) = |P(u)|Ae^{\imath(\phi(t,r=u))} \tag{3.2}$$

where $|P(u)|$ is the pupil function of the optical system and $\phi(t, r = u)$ is the phase value of the electric field at a point in the pupil plane. The resulting intensity pattern in the far-field is then given as

$$I(x) = |\mathcal{F}(Q(u))|^2 \tag{3.3}$$

where $\mathcal{F}$ is the Fourier transform of the pupil plane function and the detector measures the absolute value of the square of the electric field. When each point of the electric field across the pupil has the same phase value, or isophase, the resulting far-field intensity pattern is the familiar point spread function.

If a sine wave of a definite frequency exists in the phase values across the pupil, a frac-

tion of the far-field intensity will be distributed to the corresponding inverse frequency location of this sine wave in the far-field image [47].

If we could purposefully pattern the phase of the electric field by using a deformable mirror to deliberately impart the necessary phase value $\varphi(t, r)$ to the existing isophase values at each $\phi(t, r)$, then we should be able to produce a far-field intensity pattern of any desired pattern.

How would we know what phase pattern in the electric field would produce a desired far-field pattern? And to what fidelity could a deformable mirror accurately reproduce this desired pattern in the far-field? These questions are explored in detail in the subsequent sections.

3.0.3 Finding the phase in the pupil plane that will produce a desired LGS asterism

The Gerchberg-Saxton (GS) algorithm [37] can be used to find the phase pattern in the pupil plane that will result in the desired distribution of energy in the far-field. The Gerchberg-Saxton algorithm was developed in the early 1970s and has been used in several applications from electron microscopy [38] to space-based telescope designed for extra-solar planet detection [39]. In these applications the algorithm is used to find the phase in the pupil plane, which is then nulled by the deformable mirror to optimize the resulting point-spread-function.

The GS algorithm then works in the following way:

1. We first define the amplitude and phase of the complex electric field of the pupil plane. The phase of this is what we want to find, but because it is of course unknown at the beginning, we can first start with a best-guess phase or use any phase value.

2. We then propagate this pupil function to the far-field or detector plane by use of the Fourier transform.

3. Keeping the complex phase of the transformed result, we replace the amplitude values with those of our target or measured amplitude values.

4. We then inverse Fourier transform this new far-field intensity pattern to move back to the pupil plane and an estimate of the complex electric field. The amplitude can be ignored as only the phase component of this pupil function is desired. The original phase-estimate in step 1 is then updated with this new phase from step 4, and several more iterations are performed.

Mathematically, this process for the has the following form:

$$E_1 = A_1 e^{\imath(\phi_1)} \tag{3.4}$$

$$E_2 = \mathcal{F}(E_1) = A_2 e^{\imath(\phi_2)} \tag{3.5}$$

$$E_3 = A_2 e^{\imath(\phi_2)} \tag{3.6}$$

$$E_4 = \mathcal{F}^{-1}(E_3) = A_4 e^{\imath(\phi_4)} \tag{3.7}$$

The error can only decrease (or remain the same) at each iteration due to Parseval's theorem [40].

By supplying the desired far-field LGS asterism pattern to the GS algorithm, the phase, and hence commands to the uplink-DM, can be computed that produce the target LGS distribution.

In a simulation, say one seeks to split the single outgoing LGS beam into two spots separated by 5 arcseconds as shown on the left in Figure 3.1. This simulation assumes an outgoing sodium laser beam (λ = 589 nm) with a 20 cm launch aperture. For this case, we ignore the presence of atmospheric turbulence and assume a uniform amplitude of the outgoing electric field (Gaussian profile beams will be considered later in the paper). Under these assumptions each LGS spot is limited in angular extent by diffraction, resulting in a FWHM spot of 0.6 arcseconds for this launch geometry. Furthermore, it is assumed that the intensity of the outgoing beam is split equally in half, such that the peak intensity in each spot has a normalized value of 0.5 as seen on the scale bar of left image in Figure 3.1.

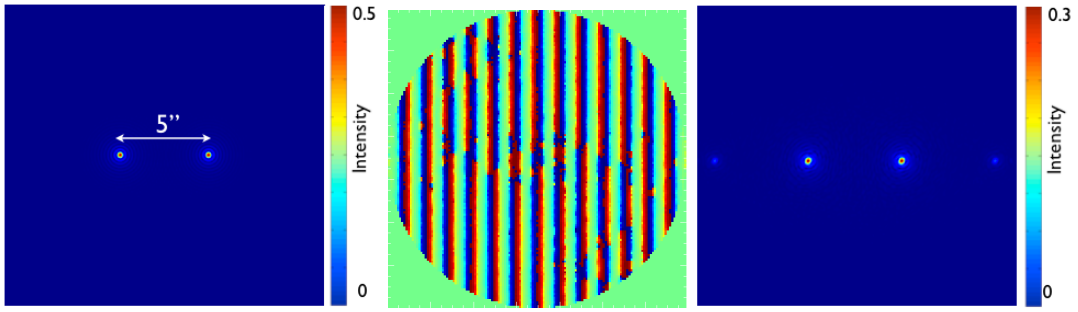

Figure 3.1: Left) Target far-field pattern consisting of 2 diffraction-limited LGS spots separated by 5 arcseconds and having equal intensity. Center) The required phase in the outgoing LGS beam that will split a single beam into the desired LGS far-field pattern. Each point in the electric-field exist within 2π radians since the outgoing laser beam is monochromatic. Right) The far-field intensity pattern resulting from propagation of the phase values. A uniform amplitude is assumed. Zero energy of the outgoing single LGS beam is directed to the center of the far-field plane. Each of the two LGS spots is λ/D in angular extent. Some energy is observed to fall outside of these locations, resulting in the peak intensity decreasing by 37%.

Passing this desired far-field pattern into the GS algorithm allows us to recover the phase values at each point in the electric field that would be responsible for the asterism. After 400 iterations of the GS algorithm, the retrieved phase values across the pupil plane are shown in the center image of Figure 3.1. As expected, the phase function has an underlying periodic signal similar to that of a grating. However, the phase map is more involved than a simple periodic function, owing to the need to direct energy away from the center of the far-field location and into the desired two LGS spot locations. Further-

more, each phase value in the electric field is within 2π radians. For monochromatic light, which is the case of sodium and Rayleigh lasers used in astronomical adaptive optics, the required deformable mirror stroke would be no greater than half of the laser wavelength.

Propagation of this derived phase up to the mesosphere results in the far-field intensity pattern shown on the right in Figure 3.1. The figure shows that each of the two LGS spots is present at the desired location. Zero intensity exists at the center of the far-field image. Furthermore, each spot is diffraction-limited with a FWHM of 0.6 arcseconds even though the beam was launched through the same, single circular pupil function. That is to say, each spot is not simply the result of half of the pupil function but is a result of the contributions of phase values across the entire aperture. Also observable is that fact that not all of the light is radiated into each of the desired two locations, as some of the energy falls to the side of each spot. This results in the corresponding peak intensity of each of the two spots measuring 0.3, a reduction of 37%.

The source of this discrepancy is still being investigated, and it is assumed to be a consequence only of the imperfect computer modeling or numerical error, and that one should be able to find a phase function that will exactly produce the target asterism.

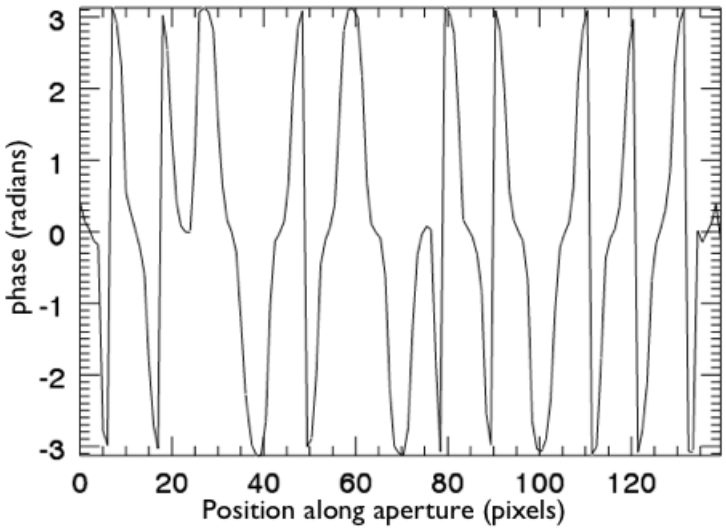

Figure 3.2: Horizontal lineout through the phase values of the center image of Figure 3.1. These phase values represent the relative oscillation of each point in the pupil plane's electric field, as recovered from 400 iterations of the Gerchberg-Saxton algorithm. Note that each point in the lineout exists within 2π radians, or one wavelength for monochromatic light. Each pixel on the horizontal axis is 0.003 meters in extent.

A horizontal lineout through the phase values of the aperture function are shown in Figure 3.2. These phase values represent the relative position of oscillation of each point in the electric field. Each pixel corresponds to 0.003 meters across the 0.2 m launch aperture. Each unique asterism pattern will, of course, result in a different phase profile.

3.0.4 Experimental Demonstration

Many candidate deformable mirrors for this application are commercially available [48]. However, an Iris AO PTT111 MEMS deformable mirror has already been shown to meet laser power handling requirements typical of astronomical facilities [46], and their nanometer go-to position repeatability [32] makes them a viable candidate for generating LGS asterisms. Thus, the first part of this section investigates the ability of MEMS DM from Iris AO to accurately produce a desired LGS asterism. A spatial light modulator from Xinetics is later used for comparison.

3.0.5 Ability of an Iris AO MEMS deformable mirror to generate Laser Guidestar Asterisms

A target far-field pattern consisting of two spots vertically separated by 0.5 arcseconds (Figure 3.3 (d)) was generated and sent through the GS algorithm. The recovered phase values are shown in Figure 3.3 (a). These phase values are then mapped to the actuators of the Iris AO PTT111 MEMS deformable mirror (Figure 3.3 (b)) and the resulting fitting error of 21.9 nm rms is shown in Figure 3.3 (c). Propagating the phase fit with DM results in the simulated far-field intensity pattern in Figure 3.3 (e). As can be seen in the image, the majority of the energy of the outgoing single beam is radiated to the two desired locations, and each spot is still approximately λ/D in angular extent. Some of the energy is observed at the center of the intensity plane, which is attributed to the inability of the DM to precisely fit the required wavefront.

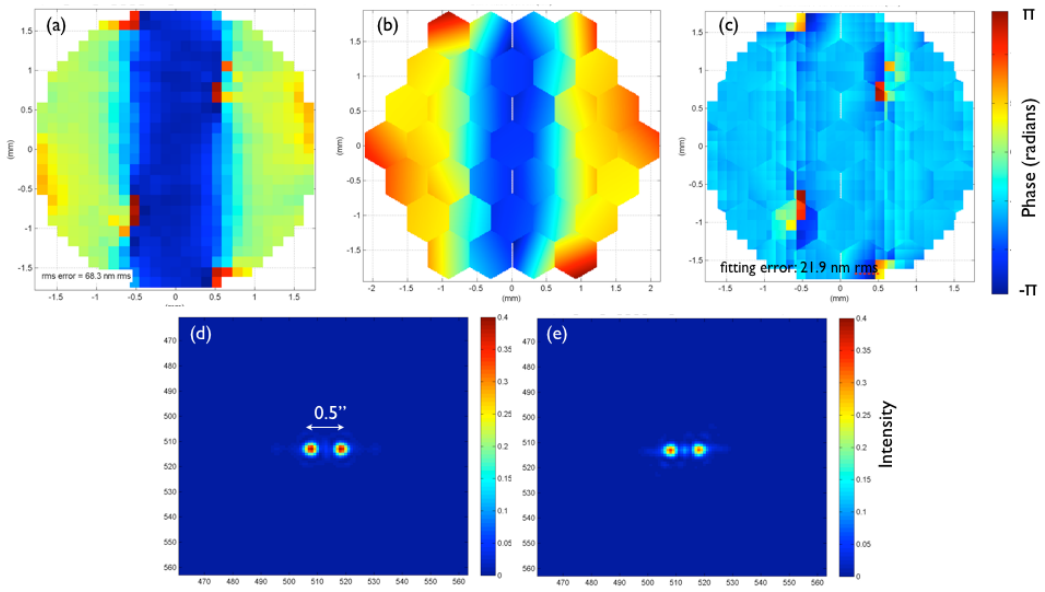

Figure 3.3: (a) Recovered phase from 400 iterations of the Gerchberg-Saxton algorithm required to split a single beam into to two spots separated by 0.5 arcseconds. (b) A fit to the phase using an Iris AO PTT111 DM. (c) Difference image resulting from the fit subtracted from the target phase, showing 21.9 nm rms residual wavefront error. (d) Simulated expected far-field intensity distribution using the phase values in image (a). (e) Resulting far-field intensity from image (b) in which the phase was fit with the Iris AOs 37 segment deformable mirror.

An IrisAO PTT111 MEMS-based AO system was used to test the efficacy with which we could accurately produce a desired far-field pattern descried in Figure 3.3 (d). A picture of the AO system is shown in Figure 3.4. Laser light ($\lambda = 632.8$ nm) is input to the system from a fiber at the upper right of the image. The light travels through the system as shown by the white line. A fold mirror passes the light towards the deformable

mirror. A telescope pair of lenses is used to match the diameter of the beam to the 3.5 mm working aperture of the deformable mirror. A splitter then sends the light to another set of fold mirrors and directs the light to the PSF camera used to measure the distribution of the far-field intensity. For the purpose of these tests, the path to the Shack-Hartmann Wavefront sensor (SHWFS) is ignored.

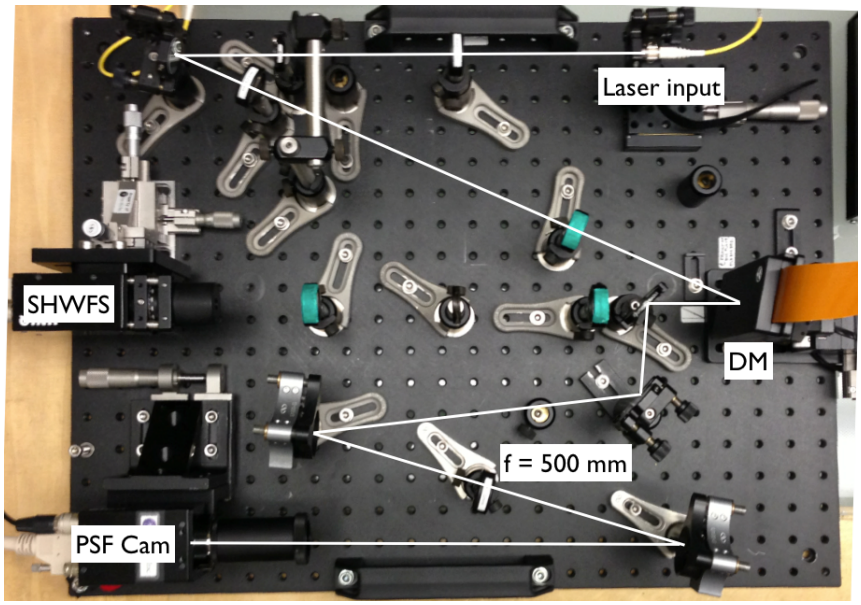

Figure 3.4: Image of the adaptive optics system (courtesy of Iris AO) used to test the ability of a Iris AO PTT111 MEMS deformable mirror to generate two LGS spots separated by 0.5 arcseconds. Laser light ($\lambda = 632.8$ nm) is input to the system from a fiber at the upper right of the image. The light travels through the system as shown by the white line. Derived phase commands for the GS algorithm are applied to the DM and measured by the PSF camera to assess the distribution of the far-field intensity.

Commands for the deformable mirror were derived from the fit of the DM to the phase

values in Figure 3.3 (b) and applied to the IrisAO PTT111 DM in the test bench in Figure 3.4. The resulting far-field intensity pattern captured by the PSF camera is shown on the right in Figure 3.5. A horizontal lineout shows that the single beam is indeed split into two distinct peaks. The energy is not equally divided between these two peaks, and some of the energy still resides at the center of the far field plane, closely resembling that of the prediction in Figure 3.3 (e).

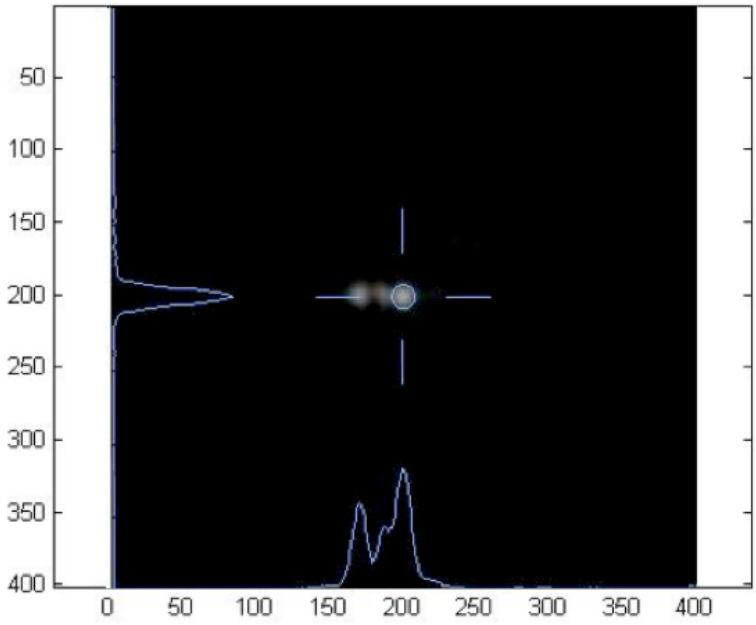

Figure 3.5: Measured far-field intensity distribution resulting from fitting an Iris AO PTT111 deformable mirror to the phase function described in Figure 3.3 (b). A horizontal lineout shows that the single beam is split into two distinct LGS spots separated by 0.5 arcseconds, in a pattern that closely resembles Figure 3.3 (e).

It was found that if the DM cannot accurately fit the required phase map needed to

produce a desired asterism, then the majority of the light is radiated to the center location of the far-field. This indicates there exist LGS asterism geometries that certain asterisms that are better suited to a DM architectures.

For instance, to split the single sodium LGS beam into 3 LGS spots oriented in a triangle with a separation of 1.5 arcsecond (Figure 3.6 (d)). As retrieved from the Gerchberg-Saxton algorithm, the required phase values of the outgoing LGS beam is shown in the top image of Figure 3.6 (a). A simulated fit of this phase with the 489 segments of the IrisAO deformable mirror is shown in Figure 3.6 (b). The ability to control each segment in piston/tip/tilt motion results in the mirror being able to accurately produce these required phase values. A difference image between the required and DM fit reveals the relatively small phase error shown in the Figure 3.6 (c).

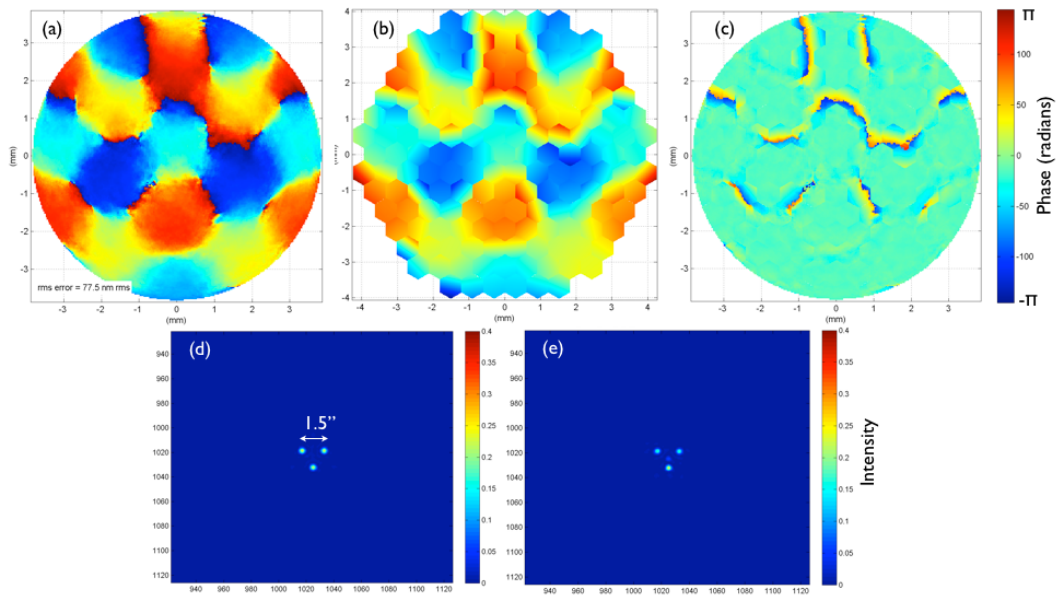

Figure 3.6: (a) Recovered phase from 400 iterations of the Gerchberg-Saxton algorithm required to split a single beam into to two spots separated by 0.5 arcseconds. (b) A fit to the phase using an Iris AO PTT111 DM. (c) Difference image resulting from the fit subtracted from the target phase. (d) Simulated expected far-field intensity distribution using the phase values in image (a). (e) Resulting far-field intensity from image (b) in which the phase was fit with the Iris AOs 37 segment deformable mirror.

The resulting simulated far-field intensity distribution, using the simulated PTT489 DM to pattern the outgoing phase, results in the image shown in Figure 3.6 (e). In comparison with the target simulated asterism in Figure 3.6 (d), the DM produces the 3 distinct LGS stars, each with an angular size of λ/D. However, again, not all of the light is removed from the center of the far-field, and we attribute this to the imperfect fit of the DM to the desired phase pattern. Lastly, there is some reduction in intensity in

each of the new spots from the target intensity, though this could be compensated in the system by turning up the laser power, though this would be unrealistic for astronomy applications, where laser light is expensive.

To compare the simulated performance of the IrisAO PTT489 device, we used the Laboratory for Adaptive Optics‘ test bench which has a Hamamatsu X8267 [50] spatial light modulator14 as a DM.

3.0.6 Ability of a Hamamatsu X8267 spatial light modulator to generate Laser Guidestar Asterisms

A schematic of the Multi-Conjugate/Multi-Object Adaptive Optics (MCAO/MOAO) test bench at Laboratory for Adaptive Optics is shown in Figure 3.8. This test bench is configured to assess the expected performance of next-generation adaptive optics applications for the Keck and Thirty Meter Telescope [51]. Our main purpose for this demonstration is to use the higher order spatial light modulator on the test bench, so we need only be concerned with the optical path highlighted with the dashed line in the test bench schematic below.

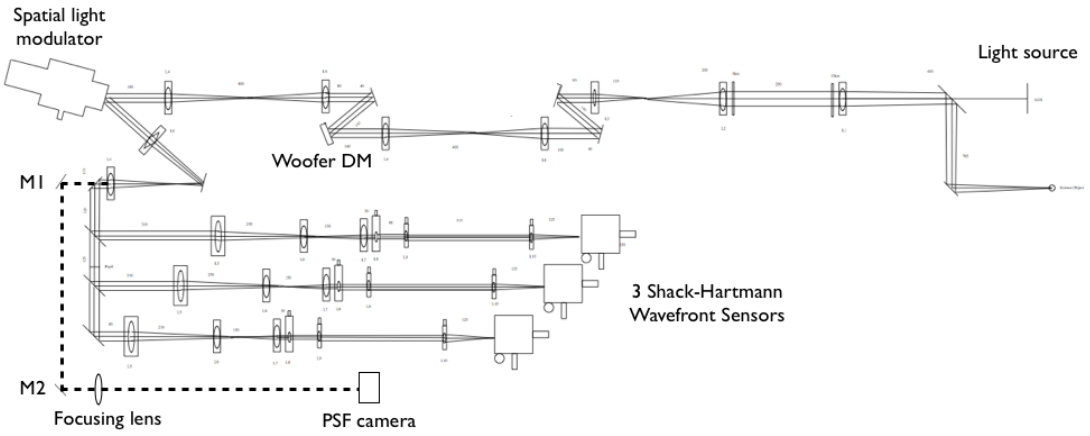

Figure 3.7: Schematic of the optical layout of the Multi-conjugate/Multi-object Adaptive Optics test bench at the Laboratory for Adaptive Optics at UCSC. It is used during these tests to measure the fidelity with which the Hamamatsu X8627 spatial light modulator (SLM) can accurately produce a desired asterism. Laser light is introduced to the system at the upper right of the image. Schematic courtesy of Renate Kupke.

Laser light is input to the system via a super-luminescent diode [SLD] shown at the top right of the schematic. An ALPAO deformable mirror acts as a woofer mirror for MCAO/MOAO tests and in these experiments the woofer is used to remove any low-order, large-stroke aberrations along the beam path. Light reflecting from the spatial light modulator is split and sent to the Shack-Hartman wavefront sensors and the PSF camera. We use only one of 3 SHWFS for this experiment, and it is used to provide closed loop control of the woofer DM only. The SLM is controlled with phase information derived from the Gerchberg-Saxton algorithm and the corresponding image of this pattern is recorded with the PSF camera.

As a direct comparison with the IrisAO PTT489 deformable mirror, the phase values (Figure 3.6 a) corresponding to the 3 LGS stars separated by 1.5 arcseconds was applied to the Hamamatsu X8627. The resulting far-field pattern seen by the PSF camera is shown in Figure 3.8. The reproduction of the target asterism is far from accurate. The intensity profile does show an expected triangular pattern, though the majority of the energy remains at the center of the field.

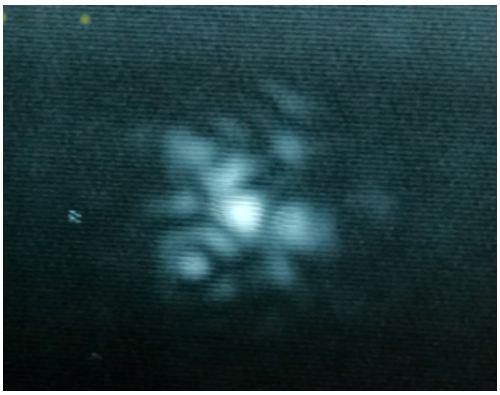

Figure 3.8: Resulting intensity measured by the PSF camera on the MCAO/MOAO bench with the SLM patterned to generate 3 LGS beacons separated by 1.5 arcseconds.

The inability of the SLM to accurately reproduce the desired pattern could be attributed to few factors; 1) the material properties of the SLM may be responsible for a large fraction of the light being scattered, and 2) residual, low-order wavefront error resulting from a poor fit of the woofer deformable mirror to the slow time-varying aberrations. This points to the importance of having good beam quality to start out with. Both of these possible sources of error are still under investigation, and further analysis on the dependence of low order phase errors across the aperture should be assessed.

3.0.7 Applications and limitations in Astronomy

The previous section demonstrates the principal that one could could use a deformable mirror to separate a single beam into a desired asterism constellation. Though the considered asterisms may be limited in angular separation for astronomy applications, in this section we focus on the requirements of an uplink AO system that would generate the asterism for the Keck Next Generation AO (NGAO) system.

The Keck Next Generation AO (NGAO) system desires 4 LGS spots arranged in a '3+1' asterism [52] [53] with one LGS spot at the center and 3 in a triangle with a 10 arcsecond radius as shown on the left of Figure 3.9. A uniform amplitude is assumed of the outgoing LGS beam. The required phase in the outgoing LGS beam at the 40 cm launch telescope that will split the single beam into the desired LGS far-field pattern is shown in the middle image of Figure 3.9.

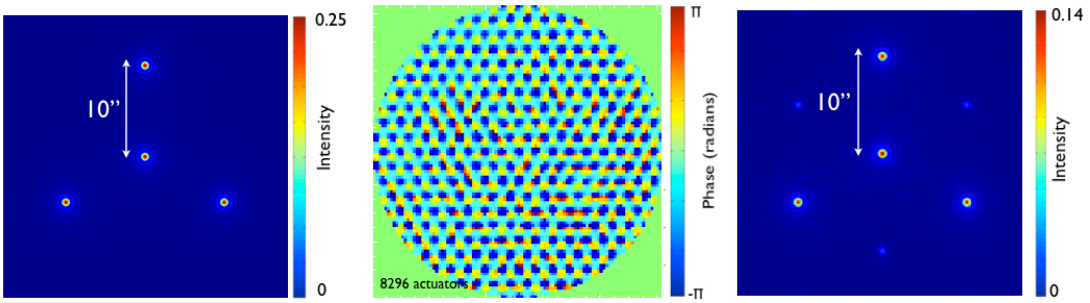

Figure 3.9: Left) The LGS asterism for the Keck Next Generation AO System. Right) The phase values in the 40 cm launch aperture required to split a single outgoing beam into the 4 equal intensity LGS spots. There are 8296 square pixels the pupil. Center) The resulting intensity pattern in the mesosphere after propagating the phase values to the mesosphere.

Each point in the electric field is within $2pi$ radians of each other. The far-field intensity pattern resulting from propagation of these phase values is shown as the bottom image. Each of the 4 recreated LGS spots is λ/D in angular extent, though some energy is observed to fall outside of these locations, resulting in the peak intensity decreasing by 56

When a Gaussian profile amplitude is assumed for the outgoing LGS beam, a more complicated phase map is retrieved from the Gerchberg-Saxton algorithm. An example of this is shown on the left of figure 3.10. This is the recovered phase from Keck's target '3+1' asterism when a Gaussian amplitude with a beam diameter of 0.3 meters at the $1/e^2$ value is assumed.

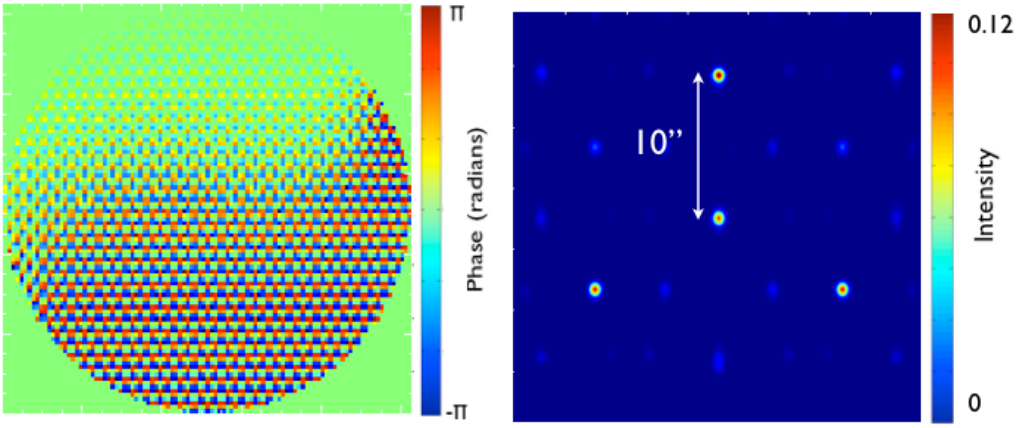

Figure 3.10: Left) Phase values at each point in the 40 cm launch telescope aperture required to split a single outgoing, 30 cm diameter Gaussian beam profile, into the perfect '3+1' LGS asterism. Right) Intensity pattern, resulting from propagation of the Gaussian beam to the sodium layer.

Propagation of this phase and amplitude distribution to the far-field give the result shown on the right in Figure 3.10. Each spot is correctly placed at the desired location, though the intensity is decreased from the target 0.25. A slight elongation of each spot is also present. The source of these artifacts is still under investigation.

A closer look at the phase values on the left of Figure 3.10 reveals that what appears as tilt in one direction is actually tilt in both the negative and positive phase space of the aperture. This is displayed in the 3D image in Figure 3.11. These rapidly changing phase variations suggest the use of a segmented DM over a continuous facesheet DM.

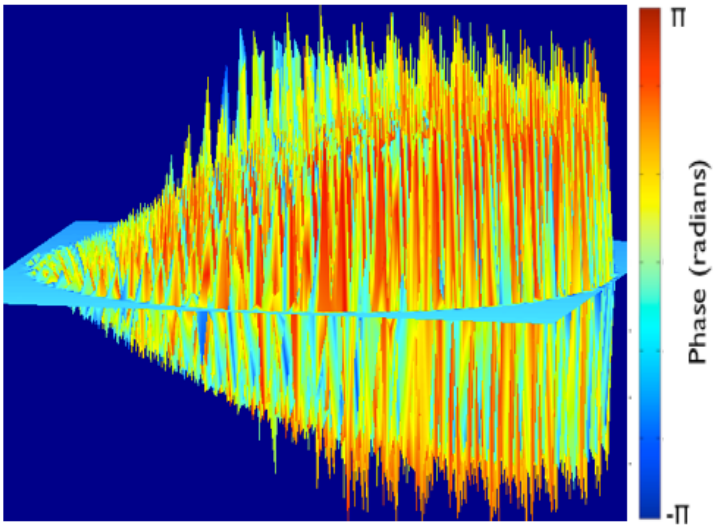

Figure 3.11: Rotated 3D view of the phase values on the left in Figure 3.10. What appears as one dimensional tilt is in that image is actually deviations in both the positive and negative phase space along the same direction. These rapidly varying phase values indicate a segmented DM would be preferred over a continuous-facesheet DM.

3.0.8 Rotation and arbitrary beacon placement

As might be expected, it is possible to rotate the phase values about the center of the beam by controlling the commands to the uplink deformable mirror. This would allow the asterism to rotate on sky at virtually any desired angular velocity. This would then preclude the need for the derotator used to correct for the field rotation and alignment of the fixed LGS spots on the wavefront sensors.

Furthermore, arbitrary patrolling beacon placement, which is a key requirement for

NGAO [54] could be achieved with the technique presented in this paper. Commands to the uplink-DM could be precompiled and stored for go-to programmability.

3.0.9 Conclusions

It is possible to create custom laser guidestar asterisms by using a deformable mirror to pattern the phase of the outgoing laser guidestar beam. This avoids the need for multiple laser launch assemblies, and in principle would allow one to position the multiple LGS spots in any desired arrangement around the science target, as well as dynamically rotate the LGS pattern on sky.

Simulations and laboratory experiments have been conducted to assess the fidelity with which a PTT111 and PTT489 Iris AO MEMS deformable mirror and a Hamamatsu X8267 spatial light modulator can accurately produce a desired laser guidestar asterism.

In closing, we note a relatively large number of actuators, 8296, is required to faithfully produce the asterism desired of Keck NGAO according to simulations presented in this paper. Further investigation is required to assess the use of other deformable mirrors for this application. Many reflective spatial light modulators, such as those from Holoeye, or a digital mirror device from Texas instruments, could potentially meet these requirements, though further analysis is required to understand their response to the relevant laser power fluences. A 3D printer maybe an alternative means for

generating the phase masks.

Chapter 4

Woofer-Tweeter Controller for the new ShaneAO System

4.1 Introduction

Most currently astronomical operating adaptive optics systems employ a single deformable mirror (DM) driven in a closed-loop feedback control system to correct for the deleterious effects of turbulent atmospheres. This DM is often conjugate to the entrance pupil, and the AO systems work well in the near-IR wavelengths over a narrow field of view. However, AO correction for increasingly demanding science goals and larger diameter telescopes introduce spatial and temporal requirements that often cannot be achieved by any single, currently-available DM. This constraint has driven the design of many AO system architectures to incorporate the use of two deformable mirrors that

complementary correct for turbulence. Such designs include that of Keck NGAO [55] the Advanced Technology Solar Telescope[56], as well as those of the thirty-meter class [57] telescopes for Single- and multiple MCAO applications. This dual deformable mirror architecture, also known as a woofer-tweeter architecture, consists of a large-stroke, low actuator density DM (woofer) in series with a low-stroke high actuator count DM (tweeter).

4.1.1 Background

In current woofer-tweeter AO systems, both deformable mirrors share the same wavefront sensor (WFS). Therefore, consideration must be given to a controller that will ensure the commands to each DM will not produce similar shapes, thus mitigating the others correction while unnecessarily using actuator stroke. Furthermore, each DMs temporal characteristics must be accounted for when the DMs bandwidth is less than that of the closed-loop AO systems.

In ophthalmology, a two-step sequential controller has been implemented in a scanning laser ophthalmoscope [58]. In this architecture the correction is first performed by the woofer DM. After the woofers correction, the tweeter DM then performs its correction while the woofer continues to hold its shape. This architecture works well when the aberrations change slowly in time, and may have applications in space-telescopes in which the surface of a controllable primary mirror and a backend deformable mirror work in series to correct for imperfections or any slow, time-varying disturbances [59].

More advanced systems exist in ground based astronomy applications such as the current woofer-tweeter architecture of the Palm-3000 AO system [60] at Palomar Observatory that offloads the tweeter DM shapes from those that the woofer DM will correct in the following time step.

When conditions require that the deformable mirrors both be updated in the same timestep, the controller must ensure that each DM has knowledge about the other DM‘s shape. One approach is to use a modal basis set and send all modes up to a certain cutoff to one DM and the rest of the modes to the remaining DM. Among these architectures are the Zernike polynomial basis set [61], the Fourier basis set [62] [63], and a modal basis set derived from the influence functions of the DMs [64]. Other proposed methods for woofer-tweeter controllers have been investigated in simulation [65] [66] that use the Lagrange multiplier and a damped least-square method to suppress the correlation between the DMs for simultaneous control of both DMs without offloading or modal splitting. This has been validated in simulation and more recently tested in vision science applications [67] and may have applications in astronomy-based AO systems. In this chapter, I report on a hybrid controller designed specifically for the ShaneAO 3-meter telescope system upgrade that uses the modal basis set of the woofer DM and zonal control of the tweeter DM.

4.1.2 Selected Woofer-Tweeter Deformable Mirror

A new adaptive optics system will replace the AO system currently in operation at the 3-meter Shane telescope at Mt. Hamilton, California. The new AO system will have two deformable mirrors (Figure 4.1) that share the same wavefront sensor. The tweeter DM is a 1024 actuator Micro-Electrical Mechanical (MEMS) DM from Boston Micromachines (BMC). An ALPAO low-speed-DM52-25 deformable mirror has been selected as the woofer. Unlike most AO systems that have a dedicated separate mirror for tip-tilt correction, the woofer DM will also act as tip-tilt corrector in this system. The ALPAO DM controls the surface of its mirror via magnetic attraction and repulsion while the MEMS DM achieves surface deflection through electrostatic attraction. Both DMs have a continuous reflective facesheet. More characteristics of each DM are listed in Table 4.1.

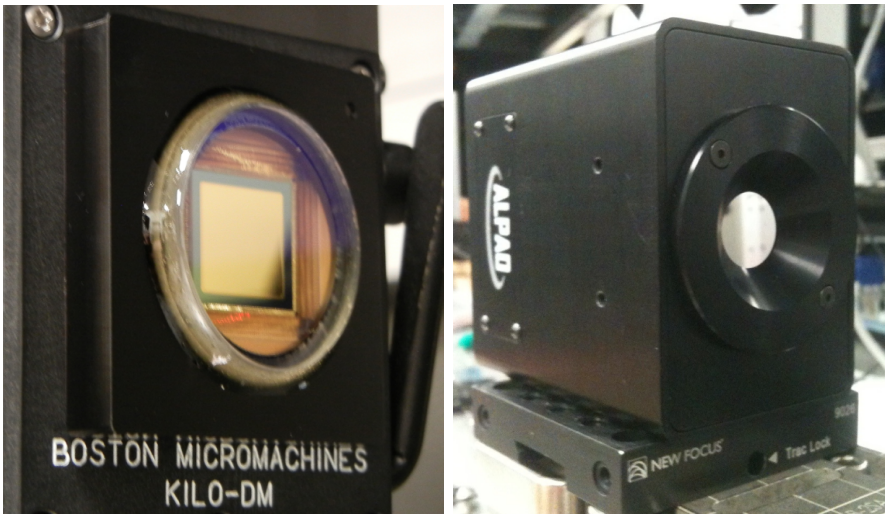

Figure 4.1: Left) Image of the Tweeter DM. The 1024 actuator device from Boston Micromachines Corporation has a reflective gold coating and a working aperture of 9.8 mm. Right)) Image of the Woofer DM, the Alpao low-speed DM52-25. This DM will also function as the tip-tilt corrector. The device has a working aperture 15 mm and is coated with protected silver.

DM Characteristic	Tweeter	Woofer
Number of actuators	1020	52
Working aperture (mm)	9.8	15
Pitch (mm)	0.340	2.5
Flat shape surface figure error (nm rms)	10	7
Wavefront tip/tilt stroke (PV microns	NA	± 50
Hysteresis (nm)	< 1	1%
Bandwidth (Hz)	60,000	250

Table 4.1: Deformable mirror characteristics of the woofer and tweeter DMs for the ShaneAO system upgrade.

4.1.3 Measured Spatial and Temporal characteristics of the ShaneAO‘s Woofer-Tweeter Deformable Mirror

The spatial and temporal behavior of each deformable mirror were characterized and used to drive the design of the controller.

4.1.4 Deflection of a single actuator

Surface measurements were recorded using a Zygo Verifire At+ interferometer when a single actuator was activated. Individual actuators were stepped from the minimum allowable input value to the maximum. During this process the remaining actuators were held at a fixed input command corresponding to the midway point of equal positive and negative displacement. This value is expected to occur near 140.0 Volts and 0.0 Amperes for the tweeter and woofer DM respectively. Measurements of the actuator‘s peak deflection relative to a reference are shown in Figure 4.2 for the tweeter and Figure 4.3 for the woofer DM.

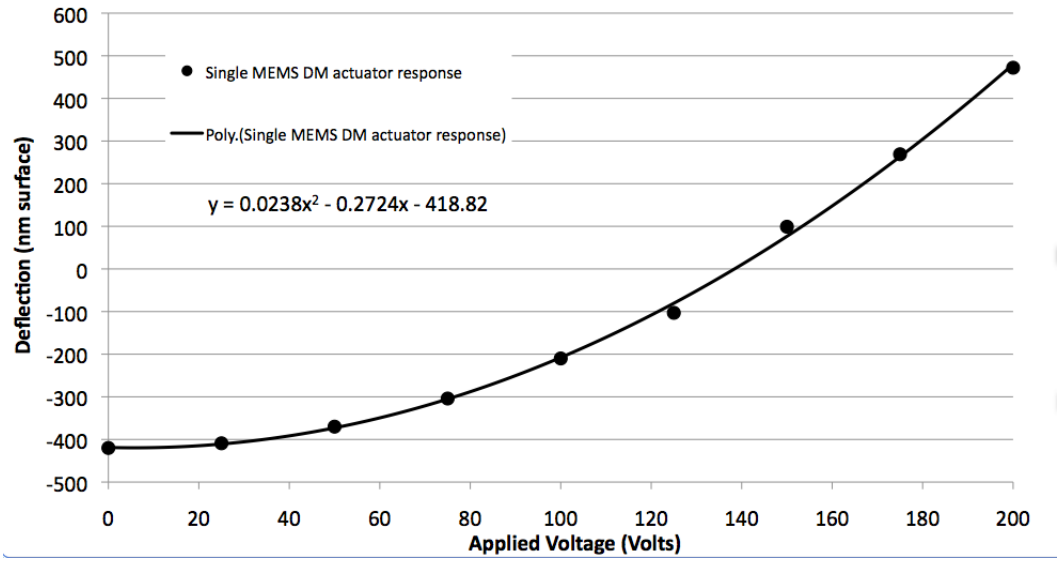

Figure 4.2: Surface deflection of a single MEMS DM actuator as the applied voltage increases. Measurements were made relative to a region of actuators held at a bias voltage of 140.0 volts giving roughly equal positive and negative surface displacement totaling 892 nm Peak-to-Valley.

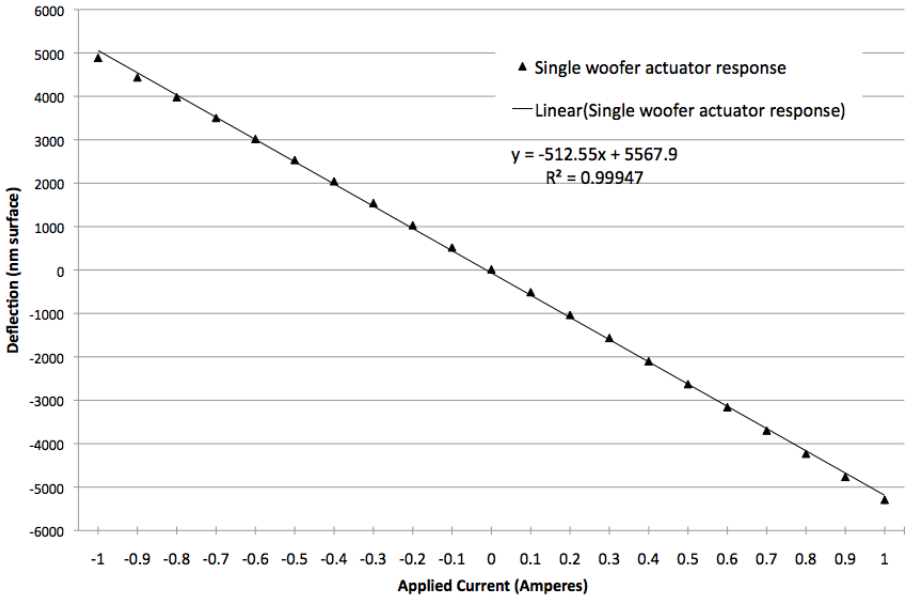

Figure 4.3: Surface deflection measurements of a single ALPAO actuator. This DM operates from a bias current of 0 Amperes. Nearly 10,000 nm of surface displacement is observed in total for this actuator. The response of the device is linear with an R^2 of 0.99947.

The response of a woofer actuator is observed to be linear as a function of the input command, with a linear least squares fit value of 0.99947. A peak-to-valley (PV) deviation of nearly 10 μm from the 0.0 Ampere bias was observed for this actuator. A PV surface deflection of roughly 6 μm was recorded for actuators at the perimeter of the device. This is most likely due to the added restoring force of the mirror‘s surface close to the attachment location.

4.1.5 Deformable Mirror Influence Function

The influence on the DMs surface when a single actuator is poked was also measured for each actuator of both mirrors using the Zygo Verifire At+ interferometer. For the case of the Woofer DM, influence functions were recorded at 20% of their maximum allowable applied current. Influence functions for the MEMS device were recorded with a single actuator poked at 165 Volts while the rest of the actuators were held at 140 Volts. The corresponding influence function for a single actuator from the MEMS DM are shown left in Figure 4.4 and that of the ALPAO DM are on the right.

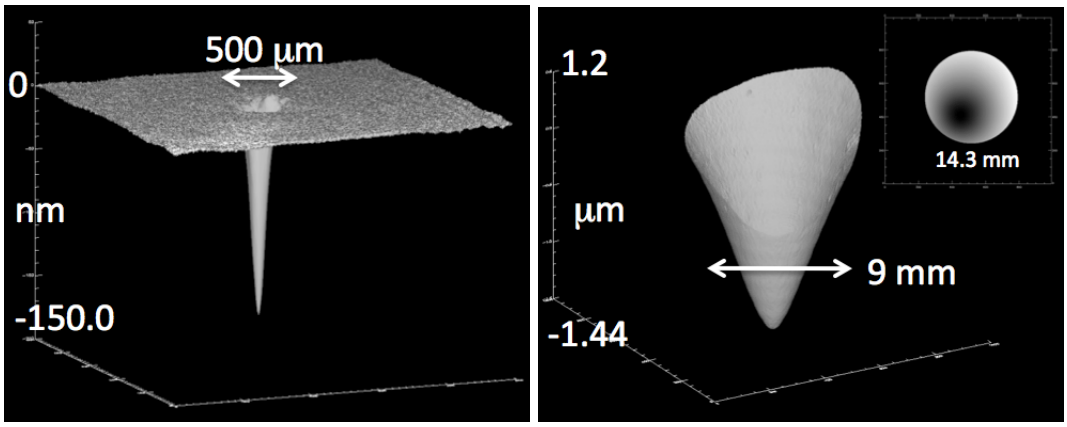

Figure 4.4: Left) A single tweeter actuator poked at 165 Volts deflects roughly 150 nm when the remaining DM actuators are at 140 Volts. The influence of the poked actuator spans roughly 500 μm in each direction. 700 of the total 1020 actuators will be used when the primary and secondary mirrors are considered over the surface of the tweeter DM. Right) Deflection of a single woofer actuator at 0.2 Amperes from the remaining actuators with 0.0 Amperes applied. The drum-head-like suspension of the reflective DM surface results in a poke of the actuator having a relatively broad influence across the selected 13.4 mm aperture diameter for the ShaneAO upgrade system.

It can be seen that the actuators on the ALPAO mirror have a very broad influence function spanning almost the entire working aperture of the device. Of the DMs 15 mm working aperture the ShaneAO upgrade system will be using a 13.4 mm aperture. In contrast to the broad influence response of a woofer actuator, the underlying posts of the MEMS DM that support the reflective top coating have a relatively narrow influence function. The influence of one actuator is 28% at its nearest neighboring actuator and

decays quickly thereafter to only a few percent two actuators away. For both DMs, we measured the influence functions of each actuator and used them to construct cross-coupling matrices for each DM.

4.1.6 Actuator Cross-coupling Matrix

The cross-coupling matrix is constructed from the DM influence functions and can allow one to build a control matrix for the device. Letting r_i(x,y) be the influence function of a single actuator recorded over the entire DM surface and r_j(x,y) be each individual neighboring actuator, the cross-coupling matrix is

$$M_{ij} = \int r_i(x,y) \cdot r_j(x,y) \mathrm{d}x \mathrm{d}y \tag{4.1}$$

In the case of woofer-tweeter mirrors, M is an N $\times$ N matrix, with units of nm^2 / dmu^2 (where dmu stands for deformable mirror unit of actuation), and N is the number of actuators (52 for the woofer, 1020 for the MEMS DM). The resulting cross-coupling matrix for each DM is shown Figure 4.5.

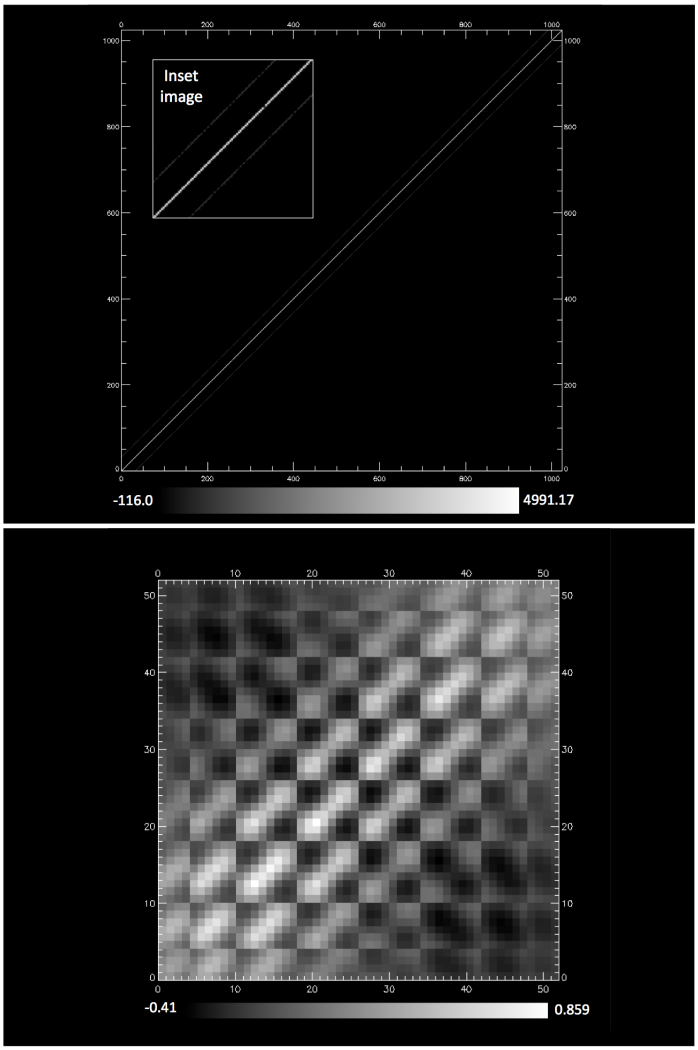

Figure 4.5: Top) Cross-coupling matrix for the 1020 actuators of the MEMS DM. The relatively narrow response of each actuator when deflected results in little influence on neighboring actuators (highlighted in the zoomed-in inset image) as observed in the narrow banded matrix. The units are (m^2/Volts^2) $\times$ pixels^2. Bottom) Cross-coupling matrix for the 52 actuators of the Alpao DM. The large influence function response of single actuator results in a matrix that has a relatively broad banded structure. The units are (m^2/Amperes^2) $\times$ pixels^2.

4.1.7 Mirror Modes

Performing a singular value decomposition [68],Landesman1992 on the mirror‘s cross-coupling matrix gives access to the DMs orthonormal modal basis set [70]. This modal set has been projected to the aperture of each DM as imaged by the Zygo interferometer. The first 20 normalized modes for each device are shown in Figure 4.6. The first mode of each DM is the lowest order mode and can be seen in the upper left of Figure 4.6. The structure of each mode increases with increasing mode number thereafter.

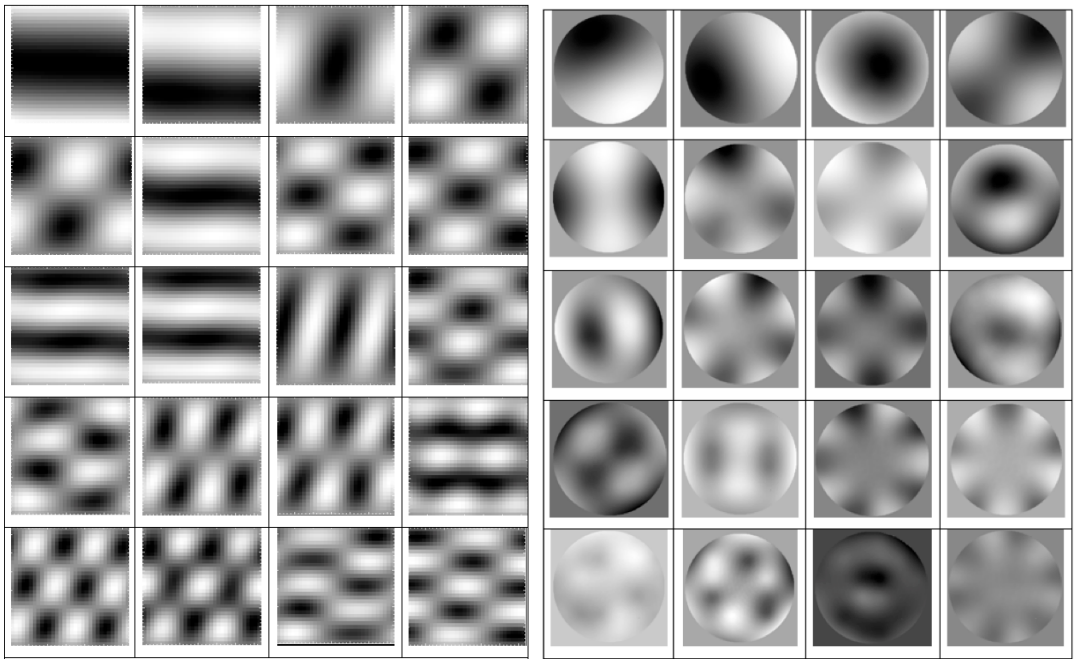

Figure 4.6: Left) First 20 orthonormal tweeter modes as viewed over the 9.8 mm working aperture of the MEMS 1K DM. Mode 1 is shown in the upper left, and the mode structure continues left to right, top to bottom. Right) First 20 orthonormal woofer modes of the woofer DM. Mode 1 is shown in the upper left. The nodes of each mode trend to the perimeter as the mode number increases leaving less correction over the full pupil.

The woofer modes appear similar in form to the Zernike polynomials [71]. Furthermore, as the mode number increases, the nodes trend around the perimeter of the device resulting in less correction across the full aperture of the telescope diameter. A possible explanation for mode 3 of the woofer not being centered may be due to differences in tension at the attached surface boundaries. The tweeter modes are more closely

representative of the Fourier modes, and are complimentary to the woofer mode space by the fact that nature of the deformation does not trend towards the perimeter of the device for increasing mode numbers.

4.1.8 Temporal characteristics of the ShaneAO‘s Woofer-Tweeter Deformable Mirror

Each mirror‘s closed-loop bandwidth is a function of the material, driving forces, and boundary conditions by which the surface is supported. Ideally, the resonant response of each mirror would be well beyond the closed-loop bandwidth of the AO system, so that any resonant frequencies or phase lag issues could be avoided. For correction of turbulence on the Shane 3 meter system, this is the case for the MEMS DM, where the underdamped resonant frequency of typical BMC devices has been observed to occur around 60 kHz [26]. In contrast, ALPAO reports that their DM has a resonance frequency at 250 Hz [72]. This feature will need to be accounted for in the controller, since driving this DM at frequencies close to this may introduce undesired phase responses of the DM and hence poor wavefront correction.

These observations have led us to design a woofer-tweeter controller that uses a hybrid modal and zonal architecture based on the normal modes of the woofer and the zonal arrangement of the tweeter actuators. Each DMs different temporal responses are also folded into the controller to ensure good wavefront correction.

4.2 Woofer-Tweeter Control architecture

The block diagram of the candidate controller is shown in Figure 4.7. The input atmospheric phase disturbance is shown entering the system from the left. The Shack-Hartman Wavefront Sensor (SHWFS) samples the gradient of the atmospheric phase over the entrance pupil. The output n×n vectors of slopes are then passed to the reconstructor.

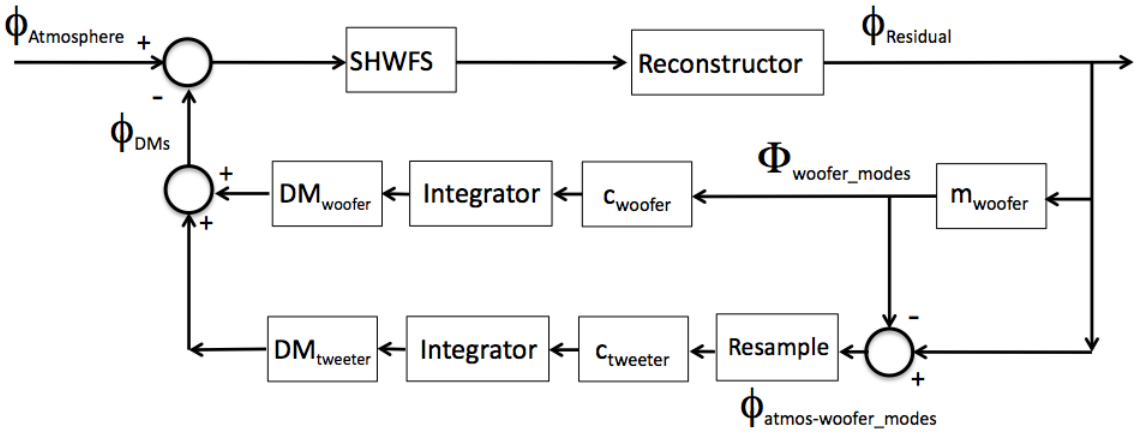

Figure 4.7: Block diagram showing the information flow for the woofer-tweeter controller. The n×n vectors of slope gradients measured by the SHWFS are reconstructed to produce the phase over the aperture. This reconstructed phase is sent first to the tweeter DM because of the relatively slow response of the woofer DM. We expect the tweeter will saturate unless the woofer modes are removed from the phase being sent to the tweeter every 0.005 seconds in delay.

Since the SHWFS is expected to be running between 500 Hz and 1.5 kHz, the recon-

structed phase will first be sent to the tweeter DM (shown in the outer loop in Figure 4.7 to avoid the resonant frequency of the woofer DM previously mentioned. We assume the response of the DM actuators obeys linear super-position and that the system is linear shift-invariant. For the case of the 8×8 or 16×16 sampling, the phase output from the reconstructor will be resampled to 32×32 space of the tweeter actuators. We expect the tweeter DM will saturate due to its limited stroke until removal of the low-order woofer modes. We convert the input phase to tweeter actuator voltage commands by using the polynomial coefficients from the least squares fit to the deflection curve of each actuator measured previously in the laboratory. The integrator tracks these command values before being sent to the DM.

Meanwhile, the same phase output from the reconstructor is being passed through the woofer loop. However, the commands for the woofer DM are only read out from the integrator every 5 milliseconds so as to avoid driving the DM past its response bandwidth. The first block encountered is m_{woofer}. By taking the inner product of the woofer modes with input phase we can know to what degree each woofer mode is present in the measured turbulence. The output phase $\phi_{woofer_{modes}}$ is the linear combination of each of these modes. This phase is then subtracted from the phase in the tweeter path, relieving the tweeter from any low-order, large stroke correction. The sum of the woofer modes is converted to commands for the woofer actuators before passing to the integrator and DM.

4.3 Results from simulation

How many woofer modes should be used? To answer this question we measured the residual wavefront error that would theoretically be passed to the tweeter DM as a function of the number of DM modes corrected. The average results, for 10 randomly realized iterations of Kolmogorov turbulence with varying r_o parameters are shown in Figure 4.8.

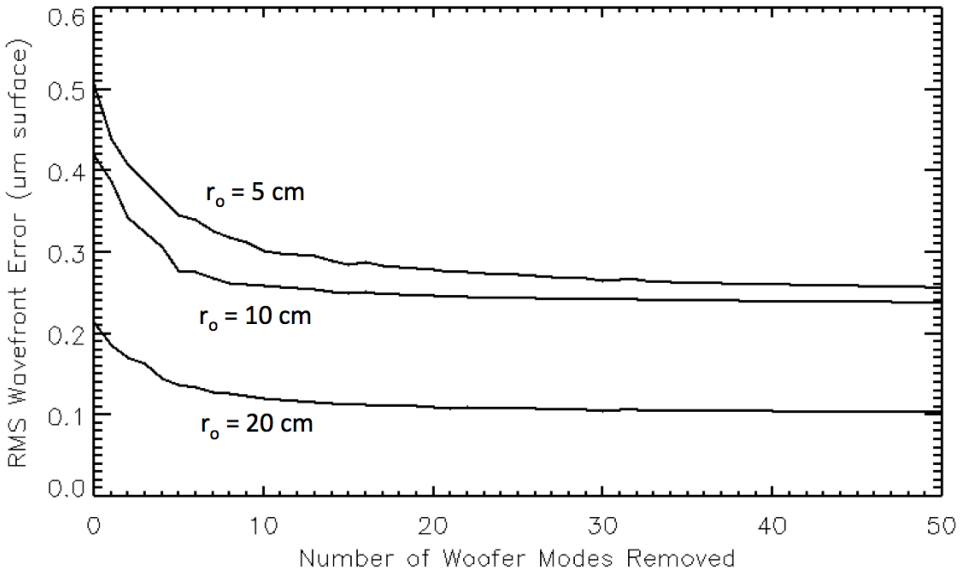

Figure 4.8: Average residual wavefront error (μm surface) from 10 randomly realized Kolmogorov turbulence screens of varying ro, as the number of woofer modes removed is increased.

As is expected, better correction is achieved at larger atmospheric coherence lengths since the wavefront error is proportional to ratio of the telescope diameter to r_o following

the 5/6 power law of Kolmogorov turbulence. The majority of the phase correction is observed to be achieved within the first 15 modes for each case, and slowly improves thereafter with the removal of more modes.

How many tweeter actuators will saturate as a function of the number of woofer modes used? To investigate this question we again used 10 computer generated phase screens with Kolmogorov statistical properties as well as closed loop telemetry data (Courtesy of Elinor Gates) from the current operating AO system on the Shane 3 meter telescope. After the removal of each subsequent woofer mode, the resulting phase was converted to tweeter commands using the quadratic coefficients discussed in Section 4.1.4. The number of tweeter actuators within the re-imaged pupil of the telescope that received a voltage command greater than 200 Volts or less than 0 Volts was tracked. This total number of actuators that saturate as a function of the number of woofer modes removed is plotted in Figure 4.9.

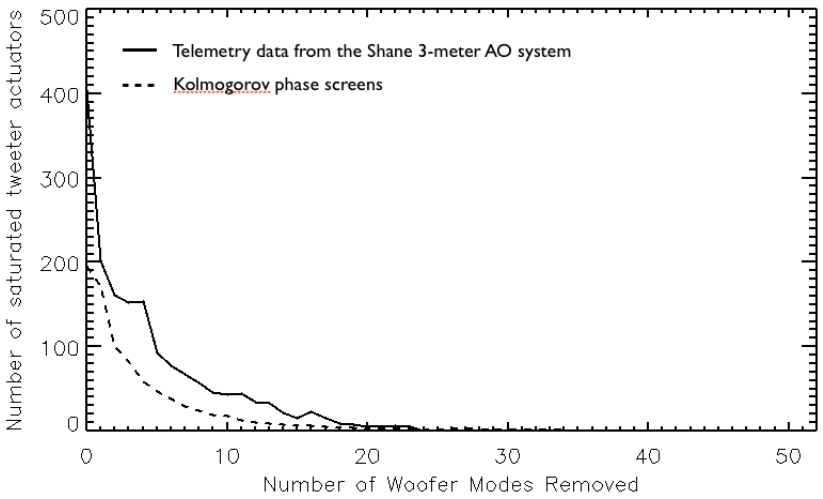

Figure 4.9: Number of tweeter actuators outside their allowable voltage range as a function of the number of modes removed from the telemetry data off the current AO system (solid line) and Kolmogorov phase screen (dashed lines). The atmospheric coherence length for both cases was 10 cm.

The first thing to notice is that without the removal of any woofer modes the tweeter actuators do indeed saturate. For the case of 10 reconstructed phase maps of the pupil from the on-sky telemetry data, with an r_o of 10 cm, an average of 403 of the 700 actuators within the pupil are either above or below their allowable input voltage range. An average of 195 actuators are observed to saturate when 10 randomly generated Kolmogorov phase screen with an r_o of 10 cm are introduced. The number of saturated tweeter actuators decreases quickly thereafter, reaching zero actuator saturation after the correction of 34 woofer modes. It is a curious observation that for the case of the telemetry data the number of saturated tweeter actuators does not continuously decrease

as more woofer modes are removed. Regardless, acceptable amplitude reduction of the input phase is achieved and more than 34 woofer modes may end up being used as a preventative measure.

Sample input phase generated numerically and measured on-site at Mt. Hamilton are shown in Figure 4.10 at top and bottom of the left column, respectively. The units of the input phase screens are in μm surface and are in agreement with the roughly 3 μm surface displacement expected of a 3-meter diameter telescope.

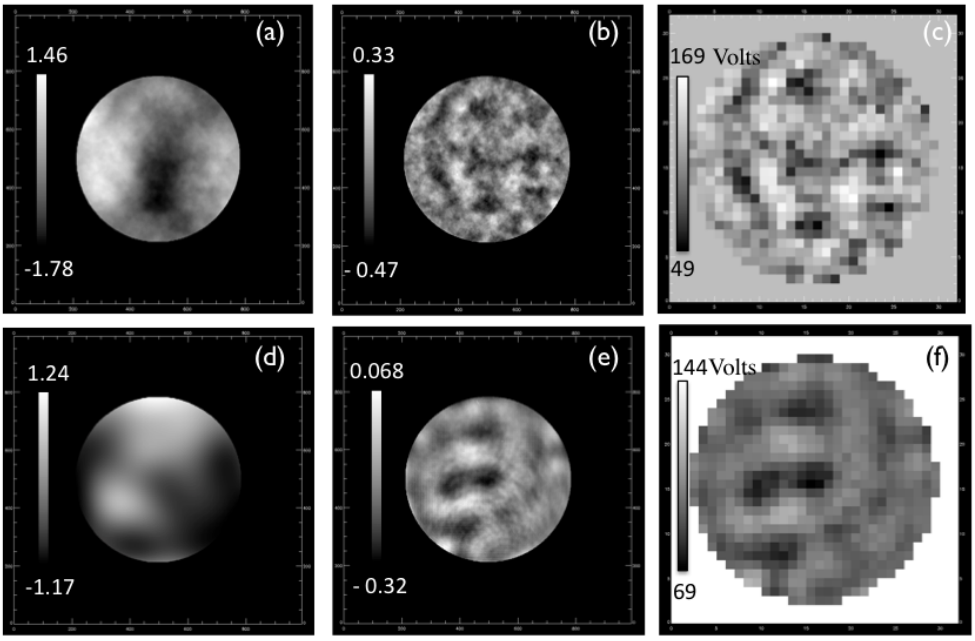

Figure 4.10: a) Input Kolmogorov phase screen with an ro of 10 cm. Units are in microns surface. The input aberration has a PV of 3.24 μm surface. b) High-spatial frequency aberrations are observed after correction of 52 woofer modes, with a PV displacement of 0.8 μm surface. c) The residual phase reimaged to the 32×32 tweeter DM plane and converted to actuator voltage commands. d) Reconstructed input phase as measured by the current 3-meter Shane AO system. The input aberration has a PV of 2.41 μm surface. e) Residual WFE after the removal of all 52 woofer modes resulting in a PV displacement of 0.38 μm surface. f) Derived voltage commands for tweeter DM after correction with the woofer, ranging from 144 Volts to 69 Volts.

High and low-spatial frequencies can be seen in the statistically accurate, Kolmogorov phase. Filtering effects of the telemetry data caused by the SHWFS can be seen in the

smoothed phase representation in the bottom left image of Figure 4.10. In both cases, correction with the woofer DM results in residual PV surface deviations on the order of 800 nm and 380 nm shown in the center column. For each case, this residual surface displacement is within the stroke requirements as seen by the generated tweeter voltage commands shown in the right two images.

4.4 Discussion and conclusion

The woofer-tweeter controller for the new ShaneAO system takes into account the spatial and temporal characteristics of each deformable mirror. The limited bandwidth response of the woofer DM motivates us to first perform correction with the tweeter DM. The tweeter will thus initially be responsible for the low-order modes until the woofer DM is activated 5 milliseconds later and the projected woofer correction is subsequently removed from the tweeter path. Using this approach, our simulations show that the use of 34 woofer modes results in no tweeter actuators operating outside their reachable stroke limit of 892 nm surface Peak-to-Valley.

Chapter 5

Conclusion

"Many other people who have studied far enough, to begin to understand a little of how things work, are fascinated by it, and this fascination drives them on, to such an extent, that they've been able to convince Governments and so on to keep supporting them, in this investigation that THE RACE is making into its own environment." -R. P. Feynman

This thesis has investigated the response of several micro-electrical mechanical systems (MEMS) deformable mirror for their response to incident, high-power, visible-laser light. Results of these experiments were used in designing, constructing and testing on-sky the world's first MEMS-based adaptive optics system. Wavefront correction provided by the uplink system consistently produced a more compact laser spot in the mesosphere. A novel extension of this system as a tool for generating LGS asterisms from a single laser beam has also been developed and preliminary tests have been conducted in the

lab.

A closed-loop control system to drive two deformable mirrors of different spatial and temporal characteristics but that also share the same wavefront sensor has also been developed.

Bibliography

[1] H. W. Babcock – The Possibility of Compensating Astronomical Seeing – Astronomical Society of the Pacific, Vol. 56, NO. 386 (1953).

[2] Duffner, Robert W. – The Adaptive Optics Revolution, A History – University of New Mexico Press, 2009.

[3] D. L. Fried, – Adaptive Optics Development: A 30-Year Personal Perspective – Proc. SPIE 4376,(2001).

[4] David George Voelz - Computational Fourier Optics, a Matlab tutorial – SPIE , Tutorial Texts in Optical Engineering, Volume TT89, 2010.

[5] A. N. Kolmogorov, – Dissipation of energy in locally isotropic turbulence – Doklady Akad, Nauk SSSR 32, 16. (Translation in Turbulence, Classic Papers on Statistical Theory, eds. S. K. Friedlander and L. Topper, Interscience, New York, 1961.)

[6] V. I. Tatarski – Wave Propagation in a Turbulent Medium – McGraw-Hill, New York, 1961.

[7] D. L. Fried – Statistics of a geometric representation of wavefront distortion – J. Opt. Soc. Am. 55, 1427 - 1435.

[8] D. L. Fried – Optical resolution through a randomly inhomogenius medium for very long and very short exposures – J. Opt. Soc. Am. 65, 1372 - 1379.

[9] D. L. Fried – Optical heterodyne detection of an atmospherically distorted signal wavefront –Proc. IEEE 55, 57- 67.

[10] Taylor, G. I. 1921.– Diffusion by Continuous Movement –. Proc. London Math. Soc. 20:196.

[11] Claire Max – Propogation of light through atmospheric turbulence –Lecture 5, UCSC Astronomy course 289C. http://www.ucolick.org/ max/289/

[12] Rachel Rampy, Donald Gavel, Simon Rochester, Ronald Holzlhner, – Investigations of long pulse sodium laser guide stars, – Proc. SPIE 8447, (2012).

[13] Holzlohner, S. M. Rochester, D. Bonaccini Calia, D. Budker, J. M. Higbie, and W. Hackenberg, – Optimization of cw sodium laser guide star efficiency, – Astron. Astrophys. 510, A20 (2010).

[14] Luke C. Johnson, Donald T. Gavel, Donald M. Wiberg – Bulk wind estimation and prediction for adaptive optics control systems – J. Opt. Soc. Am. Vol. 28, No. 8 (2011).

[15] Lisa Poyneer, Marcos van Dam, and Jean-Pierre Veran – Experimental verification

of the frozen flow atmospheric turbulence assumption with the use of astronomical adaptive optics telemetry – J. Opt. Soc. Am. A Vol. 26, No. 4. 2009.

[16] J. W. Hardy – Adaptive Optics for Astronomical Telescopes – Oxford University Press, New York, 1998.

[17] Marcos van Dam, David Le Mignant, and Bruce Macintosh – Performance of the Keck Observatory adaptive-optics system – Applied Optics, Vol. 43, No. 29 (2004).

[18] Donald Gavel – Laser Technology for astronomical adaptive optics – Proc. SPIE 7015, 70150J (2008).

[19] Darryl P. Greenwood and Charles A. Primmerman – Adaptive Optics Research at Lincoln Laboratory – The Lincoln Laboratory Journal, Volume 5, Number 1, 1992.

[20] J. Drummond, J. Telle, C. Denman, P. Hillman, J. Spinhirne, J. Christou – Photometry of a Sodium Laser Guide Star from the Starfire Optical Range. II. Compensating the Pump Beam – Publications of the Astronomical Society of the Pacific, 119:952-964, 2004.

[21] Andres Guesalaga, Benoit Neichel, Maxime Boccas, Celine D'Orgeville, Francois Rigaut, Dani Guzman, Jaime Anguita – Improving stability, robustness, and performance of Laser systems – Proc. SPIE. 8447, Adaptive Optics Systems III 84474M, September 13, 2012.

[22] Richard Dekany, et. al – A Roadmap for the Development of United States Astro-

nomical Adaptive Optics – 2008.

[23] Donald Gavel, Mark Ammons, Daren Dillon, Elinor Gates, Bryant Grigsby, Jess Johnson, Chris Lockwood, Kathleen Morzinski, David Palmer, Marc Reinig and Scott Severson – Visible light laser guidestar experimental system (Villages): on-sky tests of new technologies for visible wavelength all-sky coverage adaptive optics systems, – Proc. SPIE 7015, Adaptive Optics Systems, 70150G (July 07, 2008).

[24] W. Happer, G. J. MacDonald, C. E. Max, F. J. Dyson – Atmospheric-turbulence compensation by resonant optical backscattering from the sodium layer in the upper atmosphere, – J. Opt. Soc. Am. Vol. 11, No. 1, 1994.

[25] Claudia Bruchmann, Michael Appelfelder, Erik Beckert, Sylvia Gebhardt – Multilayer deformable mirrors based on wafer-level manufacturing, – 2010. http://www.ikts.fraunhofer.de/en.html.

[26] Thomas Bifano, Paul Bierden, Julie Pereault – Micromachined deformable mirrors for dynamic wavefront control, – Proc. SPIE 5533 (2004).

[27] M. A. Helmbrecht, T. Juneau, M. Hart, N. Doble, Performance of a High-Stroke, Seg- mented MEMS Derfomable-Mirror Technol- ogy, Proc. SPIE Vol. 6113, 2006.

[28] M. A. Helmbrecht, M. He, C. J. Kempf, Scaling of the Iris AO segmented MEMS DM to larger arrays, Proc. SPIE Vol. 7209, pp. 12090L, 2009.

[29] M. A. Helmbrecht, and M. He Advanced optical coating of a segmented MEMS

DM, Proc. SPIE Vol. 7209, 2009.

[30] M. A. Helmbrecht, and M. He, Andrew P. Norton, Donald T. Gavel, Laser testing of an Iris AO dielectric-coated segmented MEMS DM, Proc. SPIE Vol. 8165, 2011.

[31] Andrew Norton, Donald Gavel, Daren Dillon, Steven Cornelissen, High-power visible-laser effect on a Boston Micromachines MEMS deformable mirror, Proc. SPIE Vol. 7736, 2010.

[32] Andrew Norton, Donald Gavel, Daren Dillon, High-power visible-laser effect on a 37-segment Iris AO deformable mirror, Proc. SPIE Vol. 7595, 2010.

[33] Herbert Friedman, Gaylen Erbert, Thomas Kuklo, Thaddeus Salmon, David Smauley, Gary Thompson, Jody Malik, Nan Wong, Keith Kanz, and Kurt Neeb, Sodium Beacon Laser System for the Lick Observatory, Proc. SPIE Vol. 2534, 1995.

[34] Scot. S. Olivier, Donald T. Gavel, Herbert W. Friedman, Claire E. Max, Jong R. An, Kenneth Avicola, Brian J. Bauman, James M. Brase, Eugene W. Campbell, Carmen Carrano, Jeffrey B. Cooke, Gary J. Freeze, Elinor L. Gates, Verno K. Kanz, Thomas C. Kuklo, Bruce A. Macintosh, Michael J. Newman, Edward L. Pierce, Kennth E. Waltjen, James A. Watson – Improved performance of the laser guide star adaptive optics system at Lick Observatory – Proc. SPIE Vol. 3762, 1999.

[35] Donald T. Gavel, Herb Friedman, Brian Bauman – Lick Sodium Laser Guide Star: Performance During the 1998 LGS Observing Campaign –https://e-reports-ext.llnl.gov/pdf/236276.pdf (1999).

[36] Brian J. Bauman, Donald T. Gavel, Kenneth E. Waltjen, Gary J. Freeze, Kristian A. Keahi, Thomas C. Kuklo, Shordon K. Lopes, Michael J. Newman, Scot S. Olivier – New Optical Design of Adaptive Optics System at Lick Observatory– Proc. SPIE Vol. 3762, 1999.

[37] R. W. Gerchberg and W. O. Saxton – A practical Algorithm for the Determination of Phase from Image and Diffraction Plane Pictures – Optik, Vol. 35 (No. 2) 237-246 (1972).

[38] D. L. Missel – A Method for the solution of the phase problem in electron microscopy – J. Phys., Vol. 6, 1973.

[39] Jason Kay, N. Jeremy Kasdin, Ruslin Belikov – Wavefront correction in a shaped-pupil coronograph using a Gerchberg-Saxton-based estimation scheme – Proc. SPIE 6691Astronomical Adaptive Optics Systems and Applications III, 66910D, September 18, 2007.

[40] J. R. Fienup, Phase retrieval algorithms: a comparison, Applied Optics, Vol. 21, No. 15 (1982).

[41] J.M. Bechers – Increasing the size of the isoplanatic path with multiconjugate adaptive opitcs – Proceedings ESO Conference on Very Large Telescopes and their Instrumentation, Ulrich, M-H, Ed, Garching/Munich European Southern Observatory Conference and Workshop Proceedings 30, 693-703.

[42] Christoph Baranec, Michael Hart, N. Mark Milton, Thomas Stalcup, Keith Powell,

Miguel Snyder, Vidhya Vaitheeswaran, Don McCarthy, and Craig Kulesa, – On-sky wide eld adaptive optics correction using multiple laser guidestars at the MMT – Astrophys, J. 693, pp. 18141820, 2008.

[43] Thomas Stalcup – Design and construction of a multiple beam laser projector and dynamically refocused wavefront sensor – 2006, Ph.D. thesis, University of Arizona

[44] M. Levoy, Z. Zhang, and I McDowall – Recording and controlling the 4D light field in a microscope using microlens arrays – Journal of Microscopy, Vol. 235, Pt 2 2009.

[45] Christopher Lutz, Thomas S Otis, Vincent DeSars, Serg Charpak, David A DiGregorio, and Valentina Emiliani, – Holographic photolysis of caged neurotransmitters – Nature Methods, Vol. 5 No 9. 2008

[46] Andrew Norton, Donald Gavel, Michael Helmbrecht, Carl Kempf, Ellinor Gates, Konstantinos Chloros, Donnie Reidel, and Daren Dillon, – Laser guidestar uplink correction using a MEMS deformable mirror: on-sky test results and implications for future AO systems, – Proc. SPIE Vol. 9148, 2014.

[47] K. L. Cahoy, A. D. Marinan, B. Novak, C. Kerr, T. Nguyen, M. Webber, G. Falkenburg, A. Barg, –Wavefront control in space with MEMS deformable mirrors for exoplanet direct imaging, – J. Micro/Nanolith. MEMS MOEMS 13, p. 11105, 2013.

[48] Nicholas Devaney, Derek Coburn, Chris Coleman, Christopher Dainty, Eugenie Dalimier, Thomas Farrell, David Lara, David Mackey, and Ruth Mackey, – Charac-

terization of MEMs mirrors for use in atmospheric and ocular wavefront correction, – Proc. SPIE 6888, 2008.

[49] D.L. Fried – Probability of getting a lucky short-exposure image through the atmosphere – J. Opt. Soc. Am. 68, 1651 - 1657.

[50] http://www.loreti.it/Download/PDF/SLM/X8267.pdf

[51] S. Mark Ammons, Renate Kupke, Edward A. Laag, Donald T. Gavel, Daren Dillon, Marco Reinig, Brian Bauman, Claire Max, and Jess Johnson, – First results from the UCSC Laboratory for Adaptive Optics multi-conjugate and multi-object adaptive optics testbed, – Proc. SPIE 6272, 2006.

[52] R. Dekany, C. Neyman, P. Wizinowich, E. McGrath, C. Max – Build-to-Cost Architecture Wavefront Error Performance– 2009

[53] Keck Adaptive Optics Note 768, Next Generation Adaptive Optics: Preliminary Design Manual, 2010

[54] Jim Bell, Jason Chin, Drew Medeiros, Thomas Stalcup, Ed Wetherell, NGAO Laser Launch Facility System Performance, KAON 686, 2009,

[55] P. Wizinowich, S. Adkins, R. Dekany, D. Gavel, C. Max, R. Bartos, J. Bell, A. Bouchez, J. Chin, A. Conrad, A. Delacroix, E. Johansson, R. Kupke, C. Lockwood, J. Lyke, F. Marchis, E. McGrath, D. Medeiros, M. Morris, D. Morrison, C. Neyman, S. Panteleev, M. Pollard, M. Reinig , T. Stalcup, S. Thomas, M. Troy, K. Tsubota,

V. Velur, K. Wallace and E. Wetherell, – W. M. Keck Observatory's next-generation adaptive optics facility – Proc. SPIE7736, Adaptive Optics Systems II, 77360K, 2010.

[56] Gil Moretto, Thomas Rimmele, and Maud Langlois, – Multi-conjugate Adaptive Optics Relay Optical designs for a 4-m off-axis solar telescope – Proc. of SPIE Vol. 5171, 2004.

[57] Donald Gavel, Brian Bauman, Richard Dekany, Mathew Britton, and David Anderson – Adaptive Optics Designs for an Infrared Multi-Object Spectrograph on TMT – Proc. of SPIE Vol. 6272, 62720R, 2006.

[58] Diana C. Chen, Steven M. Jones, Dennis A. Silva, and Scot S. Olivier, – High-resolution adaptive optics scanning laser ophthalmoscope with dual deformable mirrors, – J. Opt. Soc. Am. A 24, 1305-1312 (2007).

[59] Brij Agrawal and Joel Kubby, – Applications of MEMS in segmented mirror space telescopes, – Proc. SPIE 7931, 793102 (2011);

[60] Antonin H. Bouchez, et. al. – Status of the PALM-3000 high-order adaptive optics system, – Proc. SPIE, Vol. 7736, 2010.

[61] S. Hu, B. Xu, X. Zhang, J. Hou, J. Wu, and W. Jiang, – Double-deformable-mirror adaptive optics system for phase compensation, – Appl. Opt. 45(12), 26382642 (2006).

[62] Lisa Poyner and Jean-Pierre Veran, – Optimal modal Fourier-transform wavefront control, – Optics Society, Vol. 22, No. 8, 2005 et al.

[63] J. Lavigne, J. Vran, and L. A. Poyneer, – Woofer - Tweeter Control Algorithm for the Gemini Planet Imager, – in Adaptive Optics: Analysis and Methods/Computational Optical Sensing and Imaging/Information Photonics/Signal Recovery and Synthesis Topical Meetings on CD-ROM, OSA Technical Digest (CD) (Optical Society of America, 2007), paper AWB5.

[64] R. Conan et al., –Distributed modal command for a two-deformable-mirror adaptive optics system, – Applied Optics, Vol. 46, 2007.

[65] Peter Hampton, Radolphe Conan, Colin Bradley, Pan Agathoklis, – Control of a woofer tweeter system of deformable mirrors, – Proc. SPIE Vol. 6274, 2006.

[66] Weiyao Zou, et al. – Wavefront-aberration sorting and correction for a dual deformable-mirror adaptive-optics system, – Opt. Letters, 33(22), 2008.

[67] Weiyao Zou and Stephen A. Burns, – Testing of Lagrange multiplier damped least-squares control algorithm for woofer-tweeter adaptive optics, – Appl. Opt. 51, 1198-1208 (2012).

[68] David Watkins, –Fundamentals of Matrix Computations, – Third Edition, Wiley, 2012.

[69] Edward Landesman and Magnus Hestenes,– Linear Algebra for Mathematics, Science and Engineering, – Prentice-Hall, 1992.

[70] Thomas Farrels thesis on Woofer-Tweeter Adaptive Optics for Astronomy, 2010.

[71] Robert J. Noll, – Zernike polynomials and atmospheric turbulence,– J. Opt. Soc. Am. 66, 207-211 (1976).

[72] Alpao Low speed DM52 25 Test report, page 13.

[73] Lisa Poyneer, Don Gavel, James Brase, – Fast wave-front reconstruction in large adaptive optics systems with use of the Fourier transform, – JOSA-A, 19, 10, Oct 2002, pp 2100-2111.

Appendix A

Code

```
;PRO GS_LGS_asterism
;Author: Andy Norton
;5/20/2014

;---------------------------
; Physical Constants
;---------------------------
c = 3.0e8  ; speed of light
cm = 1.e-2
microns = 1.e-6
nm = 1.e-9
mm = 1.e-3
km = 1.e3
ms = 1.e-3
arcsec = !pi/(180.*3600.)
i = complex(0.,1.)
seed = 7

;---------------------------
; Problem Parameters
;---------------------------
lambda = 589.*nm
d_launch = 40*cm;
r0 = 10.*cm       ; seeing parameter
```

```
n = 1024            ;number of fine pixels in simulation
du = 1./float(n)  ; size of fine pixel
df = 1./(n*du)    ; size of frequency domain sample, in m^-1
zNA = 90.*km
astig = 3.        ; radians peak-to-valley
dtheta = (lambda/d_launch)/n ; size of fine pixel in far field
; (angle) in radians
sf = 10.*cm       ; spatial filter scale for sensing
dx = zNa*dtheta   ; size of fine pixel in far field (at the sodium
; layer) in meters
nf = (1./sf)/df   ; number of frequency bins low-pass filter
filter = zeropad(ones(nf,nf),n,n);low-pass filter in the spatial
;frequency domain
du = sqrt(zNa*lambda/float(n))
dx = du
D_pix = 2.0*(d_launch/2.)/du ;telescope diameter converted
;to pixel space
ratio = n/D_pix
print,ratio,'ratio of linear pixels to telescope size'
rad = round(D_pix/2.)

;aperture
ap = circle(n,n,n/2,n/2,(d_launch/2.)/du,1.)

;introduce beam profile -- amplitude only
;gbeam = gauss2(n,n/2.,n/2.,0.5*(d_launch/2.)/du)
;mag = ap*gbeam
mag=ap;*power

;-----------------------------------------------
; (SOURCE)
;-----------------------------------------------
phs = ap*0.0
wfs = mag*exp(i*phs);E field in the source pupil plane
isource = abs(wfs);source intensity at the pupil plane

;-----------------------------------------------
;    (TARGET)
;-----------------------------------------------
;   intensity with 'unkown' phase aberration
pht = ap*0.0
wft = mag*exp(i*pht);Efield in the target pupil plane --
;pretend the phase is unkown
```

```
ftft = ft(wft);source frequency domain
itarget = abs(ftft);^2 ; target intensity measurement
part = itarget[n/2.-100:n/2.+100,n/2.-100:n/2.+100]

;fit Gaussian to spot to find FWHM for later use
;; Record the !except value for later...
prevexcept = !except
message, /info, "Current exception value is " +
;strtrim(prevexcept,2)
!except=0 ;
; by gauss2dfit
  ;; Fit a 2D Gaussian
;!except=0
var = GAUSS2DFIT(part,A) ;
;!except=prevexcept ; restore to previous value

;print,'--------iteration',strtrim(i,1),'---------'
print,'A',a
;print,'center pixel x and y = ',A[4],A[5]
;print,'FWHM x pixels =',strtrim(A[2],1),'FWHM y pixels
; =', strtrim(A[3],1)
print,'FWHM x pixels =',strtrim(2.355/2.*A[2],1),'----
;-FWHM y pixels =',         strtrim(2.355/2.*A[3],1)
;print,'mean FWHM (pixels) = ',strtrim(((A[2]+A[3]))/2.0,1)
print,'geometric mean FWHM (pixels) =
strtrim(2.355/2.*(A[2]+A[3]),1);,strtrim(sqrt(A[2]*A[3]),1)

FWHM_pix = 2.355/2.*A[2];
spot_size = (lambda/d_launch)*206265.

arc_sep = 5  ;desired arcsecond seperation in mesosphere

pix_per_arcsec = fwhm_pix*(1./spot_size)
print,'pix per arcsec',pix_per_arcsec
sep_coef_pix = arc_sep*pix_per_arcsec ; separation
print,'desired separation between stars:',arc_sep,'arcseconds'
print,'desired separation in pixels',sep_coef_pix,'pixles''

;KECK NGAO 4 LGS asterism
n_targets = 4.
theta = !pi/2
theta1 = (7*!pi)/6
theta2 = (11*!pi)/6
```

```
gs1 = SHIFT(itarget, 0,sep_coef_pix);top star
gs2 = SHIFT(itarget, sep_coef_pix*cos(theta1),&
;sep_coef_pix*sin(theta1));left star
gs3 = SHIFT(itarget, sep_coef_pix*cos(theta2),&
;sep_coef_pix*sin(theta2));right star
gs4 = itarget
itarget3 = gs1+gs2+gs3+gs4
max_itarget = max(itarget3)
imax = max_itarget
itarget4 = itarget3/max_itarget/n_targets ;
disp,itarget4,'TARGET far-field intensity pattern'

;--------------- THE G-S LOOP ----------------------
A_phase = phs*0.0;initial phase for loop, can be a guess or all zero

stop
for j = 0,400 do begin ;
B = isource*exp(i*A_phase)
C = FT(B)
D = itarget4*exp(i*atan(imaginary(c),real_part(c)))
A = FT(D,/inverse)
A_phase = atan(imaginary(A),real_part(A))
endfor
disp,A_phase*ap,'recovered phase'

;Propogate calculated phase back to Na layer
foo = mag*exp(i*A_phase*ap)
foo2 = ft(foo)
bar = abs(foo2)
fmax = max(bar)

perc_change = (abs(fmax - imax)/imax)
from_orig = imax/imax/4.0*perc_change
perc_coef = imax/imax/4.0-from_orig

;normilze bar
bar_norm =bar/max(bar)
bar_final = bar_norm*perc_coef

itargetn = itarget4/imax/4.0
disp,itargetn,'itarget normilized'

disp,bar_final,'predicted target normilized'
```

```
END
```